2016

The Synthesis and Characterization of Multifunctional Nanoparticles of Elastin-Like Polypeptides for Theranostic Applications

James T. Cole
Cleveland State University

THE SYNTHESIS AND CHARACTERIZATION OF MULTIFUNCTIONAL NANOPARTICLES OF ELASTIN-LIKE POLYPEPTIDES FOR THERANOSTIC APPLICATIONS

JAMES T. COLE

Bachelor of Science in Biomedical Engineering

Case Western Reserve University

December 2005

Master of Science in Chemical Engineering

Cleveland State University

May 2009

Submitted in partial fulfillment of requirements for the degree of

DOCTOR OF ENGINEERING IN BIOMEDICAL ENGINEERING

at the

Cleveland State University

December 2014

We hereby approve this dissertation for

James T. Cole

Candidate for the Doctor of Engineering in Biomedical Engineering degree for the

Department of Chemical and Biomedical Engineering

and CLEVELAND STATE UNIVERSITY's College of Graduate Studies

Nolan B Holland, PhD., Dissertation Committee Chairperson, Department & Date

---

Chandra Kothapalli. PhD., Dissertation Committee Member, Department & Date

---

Xue-Long Sun, PhD., Dissertation Committee Member, Department & Date

---

Sandra Halliburton, PhD., Dissertation Committee Member, Department & Date

---

Vinod Labhaserwar, PhD., Dissertation Committee Member ጰ Department & Date

Student's Date of Defense: Decemeber 11, 2014

This student has fulfilled all requirements for the Doctor of Engineering degree.

Dan Simon, PhD., Doctoral Program Director

ACKNOWLEDGEMENTS

First I would like to thank Dr. Nolan B. Holland, for all of his guidance and support over the course of my many years of research and study. He has helped guide me through the challenges of determining the course of study I would like to take as well as providing never ending support for the paths I decided to undertake with this research. Without the support and guidance of my advisor, I would have never been able to accomplish any of the goals I have achieved thus far.

I would also like to thank Dr. Xue Long Sun for the use of the dynamic light scattering instrument as well as other instruments in his lab over the years and Dr. Chandra Kothappalli for the use of the fluorescent microscope that enabled my targeted nanoparticle research to be visualized. I would also like to thank Dr. Joanne Belovich for allowing me to use her laboratory for the purposes of my cancer cell research. Without the generosity of these 3 in allowing me to use their instruments many of my more challenging goals would not have been possible to achieve.

Dr. Ali Ghoorchian was my initial partner in this work and whose incredible drive and work ethic always inspired me to work harder on achieving these research goals. I wish him well in all his future endeavors and I learned a great deal about how to be a better researcher from him. Through the years I have had many students pass through the lab and each one of you was unique and my experiences in helping you achieve your goals have meant a great deal to me. This past year Eric Helm joined the lab, and he helped me in more ways than I can ever thank him in terms of understanding how to utilize analytical chemistry. Finally Mr. Kurt Farrell has been the most supportive

colleague I have worked with. He never refused to help in any way or put his needs above others and for that I will always be grateful.

Ms. Becky Laird and Darlene Montgomery in the Department of Chemical and Biomedical Engineering office have been tremendous sources of support to me for the last 7 years and I will always be thankful for their help in making life as easy as possible during my studies. Further Dr. D.B. Shah has always been a great ally and source of conversation about any number of topics, and whom I will always remember as a friend.

I would like to thank my father Thomas Walker for always making life as easy as possible for me during this journey, and supporting me in an innumerable number of ways since childhood. Finally I would like to thank Ms. Anjali Kottha for her love, support and understanding as I accomplished the goal of completing this dissertation.

THE SYNTHESIS AND CHARACTERIZATION OF MULTIFUCNTIONAL NANOPARTICLES OF ELASTIN-LIKE POLYPETIDES FOR THERANOSTIC APPLICATIONS

JAMES T. COLE

ABSTRACT

Theranostics is a promising field that aims to combine therapeutics and diagnostics into single multifunctional formulations. This field is driven by advancements in nanotechnology and specifically in the creation of multifunctional nanoparticles capable of providing the necessary functionalities. Elastin-like polypeptides (ELPs) are a class of environmentally responsive biopolymers that are known to undergo a transition in response to various stimuli. The organic nature of ELPs along with the ability to control their design at the gene level and the aforementioned responsive behavior make them a promising candidate for use in theranostic systems. The system presented here is one of the first examples of using ELPs as the base for multifunctional theranostic nanoparticles.

Presented in this study is a fully protein based self-assembling nanoparticle system based on micelles of ELPs for use in theranostic applications. Micelle forming ELP constructs have been modified through the fusion of the protein based MRI contrast agent CA1.CD2 to the C terminal of existing protein constructs. Micelles were then crosslinked into stable nanoparticles that relied only on changes in temperature to drive the transition. In addition to that, a targeting peptide has been added to the system as well to provide active targeting to cancer cells. As a contrast agent the system has been shown

to bind and retain gadolinium while effectively providing contrast in *T1* weighted imaging and having higher relaxivity values than clinical contrast agents. Modification of the architecture of the construct through changes of the tail length, and through creation of mixtures did not drastically affect the behavior of the system demonstrating its flexibility. Here I detail, the design, synthesis of the expression, purification and characterization of all the required properties of the constructs.

TABLE OF CONTENTS

LIST OF TABLES

LIST OF FIGURES

CHAPTER I

INTRODUCTION AND BACKGROUND

(Modified from publication with N.B. Holland, Drug Delivery and Translational Research, 5, 2015, 295-309)

1.1. Multifunctional nanoparticle theranostic systems

Cancer is the second leading cause of death in the United States with projections estimating 1,665,540 new cases occurring with 588,720 deaths or 1,600 deaths per day[1]. Despite advances in treatment, diagnosis and prevention options, cancer mortality rates however have only dropped 1.6%, which given the total number of cases, is not a significant improvement[2]. These statistics indicate that there is a pressing need to develop novel treatments and approaches that will enhance the survival rates.

Chemotherapeutics, although successful in reducing deaths directly related to cancer, suffer from very poor pharmacokinetic profiles as well as non-specific mechanisms of action, which in turn leads to a tremendous amount of systemic toxicity for the patient. These drugs also are known to target any highly proliferative cell, not just

cancer, and the non-specific mechanism of action exposes all of these cells to the drug and causes damage to these as well, such as hair follicles, stomach lining and bone marrow[3]. The non-specific mechanism of action also reduces the amount of drug that is actually delivered to the cells of interest, which results in the need for higher and continuous doses.

In recent years nanoscale materials have been developed for a wide range of purposes related to drug delivery, cancer treatment and diagnosis. These materials present numerous opportunities to improve the current state of cancer diagnosis and treatment available to patients. Currently there are numerous clinically approved formulations that are comprised of nanoparticle drug delivery systems which have been shown to reduce the toxic side effects associated with traditional chemotherapy regimens[4]. These therapeutic loaded nanoparticles have displayed limited long-term success clinically, which has led to the need to attempt to develop new strategies to improve the efficacy of nanoscale treatments through addition of numerous functional elements. Active targeting enhancements as well as imaging modalities have been imparted into the nanoparticles to create truly multifunctional formulations.

Theranostic nanoparticles represents the culmination of all the strategies that have been imparted onto multifunctional nanoparticles into one package. The traditional definition of theranostics is that they are a therapeutic (Thera-) and diagnostic (nostic) in the same formulation[5]. In order to achieve this multi-functionality typically 4 components are include in the formulation (Figure 1-1).

1) Nanoparticle base

2) Diagnostic imaging domain

3) Targeting ligand

4) Therapeutic

Once the interplay between all of the components has been optimized the field of theranostics holds the ability to potentially drive the field of nano-medicine into the area of "personalized medicine"[6]. The concept of personalized medicine is to attempt to tailor medicinal regiments and treatments to the specific characteristics of each individual patient[7] due to the idea that no single individual undergoes the same response to any therapeutic agent. This therapy may aid in reducing undesirable side effects of treatment and potentially produce better results.

The diagnostic imaging domain component can be utilized before starting treatments, which can potentially allow for the exact nature, phenotype and stage of the disease state to aid in guiding treatment. This capability allows theranostic compound to act as a guided biomarker to support the treatment regimen chosen, the efficacy of the dosage as it's delivered or predict the response to treatment[8]. In theory this powerful technique can help to maximize drug efficacy and reduce the guesswork associated with development of cancer treatments. In order to take advantage of these techniques however, it is necessary for a sufficient amount of contrast to accumulate in the region of interest. The usage of the nanoparticle platform becomes quite advantageous in this regard because of the ability to decorate or functionalize the surface of the particles with these domains. Commonly included imaging modalities include magnetic resonance imaging (MRI), computed tomography (CT), optical imaging (fluorescence and bioluminescence) and radionuclide imaging (PET and SPECT).

There are a large number of nanoparticle formulations that can be used as the base for a theranostic system, and these include both organic and inorganic nanoparticles. Common materials used to synthesize or form nanoparticle systems include proteins, polymers, lipids, gold and iron oxides. Each class of particles will have a size of less than 150 nm in diameter, with highly heterogeneous particle distributions and sufficient stability *in vivo*. Further these particles must be able to be functionalized with imaging, therapeutic cargo and targeting elements while retaining their nanoparticle nature upon the addition of components. The use of targeting ligands decorated on the surface of the theranostic nanoparticles, allows for direct binding of the system to receptors that are overexpressed on tumors. Finally therapeutics can be encapsulated within these particles and be designed to either have slow release properties, which is typical of most therapeutic drug combinations or designed to have triggered release capabilities, such that upon endocytosis of the nanoparticle release occurs due to change in the environment. What follows are examples of possibilities for the different components in a theranostic system as well as useful examples.

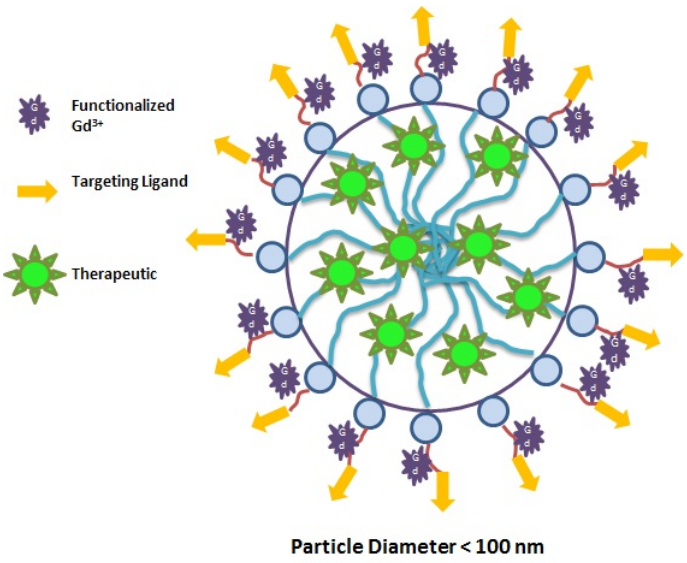

Figure 1.1. Schematic of theranostic nanoparticle. Included in a single system is a nanoparticle, an imaging component, a targeting moiety and a therapeutic component.

1.1.2. Components of multifunctional nanoparticle systems

Nanoparticle drug delivery vehicle

The nanoparticle forming material that is used for the base of the theranostic particle delivery vehicles can vary in composition, size, shape, charge and hydrophobicity. Using any composition of nanoparticles as the drug delivery vehicle can overcome the following series of limitations associated with traditional drug administration routes. The first is the problem of solubility of the therapeutic which occurs due to the fact that most chemotherapeutics are hydrophobic and subsequently require the use of solubilization agents such as Cremophor EL, which has been associated with hypersensitivity reactions[9]. The use of nanoparticles such as polymeric micelles, or liposomes can provide both a hydrophobic and hydrophilic environment which can enhance solubility[10]. The second is burst release upon administration, which can cause

significant damage to surrounding tissues or rapid degradation of the drug *in vivo*. To be considered a successful drug carrier nanoparticle drug delivery vehicles must stably encapsulate the therapeutic, which has the effect of delaying the release of in the body and protecting the payload from environmental effects *in vivo*[11]. The third limitation is traditional drug delivery routes have unfavorable pharmacokinetic profiles due to rapid clearance, which subsequently requires repeated high dosages. This is overcome using nanoparticles, which provide slower drug release, and a lower overall dosage to achieve a greater effect of the therapeutic[12]. Poor bio-distribution also occurs in these systems due to the non-specific nature of the formulation. Due to the ability to control the design of the particles either from the gene level, or through chemical reactions, targeting elements can be decorated on the surface on the nanoparticles, reducing systemic toxicity and enhancing the delivery of therapeutic at the site of interest[13]. It is clear that the use of nanoparticles as drug delivery systems offer an enormous amount of advantages as well as great potential for the future.

1.1.3. Compositions of nanoparticles

The physiochemical properties of the nanoparticles used for theranostic applications plays a very important role in determining the success of the uptake and interaction with cancer cells[14]. Factors that play a role in the ultimate success of the theranostic system include size, shape, charge, hydrophobic / hydrophilic character, and surface chemistry. The size of the nanoparticles is directly related to the cellular uptake rate of the nanoparticles[15] and is related to time the nanoparticle remains in circulation. The mechanism of uptake is known as pinocytosis[16] and can occur in two ways; the first is through passive targeting or adsorptive mechanisms and the second is through active

targeting and receptor-mediated endocytosis. In order for the particles to undergo cellular internalization it has been found that particles of the size 40 to 50 nm have maximum uptake in vitro[17], while a general range of 10 to 100 nm has been established for in vivo applications[18]. Smaller nanoparticles, such as those less than 10 nm in size, are cleared via glomerular filtration in the kidneys[19]. Larger particles are cleared through the Kupffer cells of the liver and through the spleen[20]. When targeting to solid tumors for the purpose of nanoparticle accumulation the size ranges are between 70 to 200 nm for passive targeting purposes[21], while anything larger than 400 nm is considered too large[14]. While these general size ranges have been established, there are also examples of contradictory reports and each class of nanoparticle and cell type interaction appears to needs to be investigated individually.

The shape of the nanoparticles also plays a critical role in the internalization interaction between the particles and cells. Due to the role of hydrodynamic forces in the transport of nanoparticles, the symmetry of the particles dictates the trajectory as they travel through the body[22]. Shapes that can accommodate cellular membrane wrapping are most effective at cellular uptake and between rods and spheres, spheres are more effectively taken up[23]. Spheres are symmetrical in shape and because of this the distribution of forces acting on it are constant, which will allow them to remain in the center of the blood vessel as they circulate[24]. Rods, which are asymmetrical in shape are susceptible to drag forces and torques as they circulate, which leads to alteration of the particle motion and a propensity to head towards and accumulate at the vessel walls[25]. Shape also plays a role in the circulation time and bio-distribution of the particles. It has been reported that spherical particles have shorter circulation times than non-spherical particles[26].

The charge on the surface of the nanoparticles plays a role in whether or not the particles bind to the target of interest or undergo non-specific binding elsewhere while in circulation. Cationic nanoparticles will interact with negatively charged proteins, glycans, and phospholipid head groups on the surface of cells[27], which will in turn enhance nanoparticle uptake due to increased cellular binding. Anionic particles have been shown to display enhanced uptake compared to neutral particles[28]. The charge further plays a role in the mechanism of uptake that takes place with negatively charged particles being internalized in a dynamin independent manner and positively charged particles being internalized using dynamin and F-actin[29]. Positively charged particles will be cleared via the mononuclear phagocyte system and suffer from short half-life due to interactions with blood proteins. When these interactions occur, it activates the complement pathway[30]. If the designed nanoparticles are more hydrophobic than the cell surface they are binding to, there is an enhancement of uptake[27], as well as experiencing an enhancement of protein adsorption on their surfaces[31]. Hydrophilic nanoparticles on the other hand, will attract fewer of these proteins. For this reason nanoparticles are often PEGylated, which is the process of coating the surface of the particles with polyethylene glycol (PEG)[32], a highly hydrophilic polymer coating that increases in vivo circulation and half-life times. The optimal level of PEGylation, such as the thickness of the coating, the coverage configuration and the chain length has yet to have been established and is an important factor to investigate in each nanoparticle cell pairing.

Clearly there are many factors that interplay in the design of the nanoparticles for use in theranostic systems. Despite the wealth of information available and reported, there is no way to predict the interactions that may take place in a given system.

Therefore, it is critical to determine each of these factors experimentally for a given system.

Polymers

Polymeric nanoparticles are comprised of a broad class of materials that are characterized by shapes that are either nanospeheres or nanocapsules and are composed of a backbone that is polymeric in nature with a biodegradable monomer[33]. The most common materials used to make polymeric nanoparticles are poly(lactic acid) / poly(lactic-co-glycolic acid) PLA/PGLA, block copolymers, and chitosan. Chitosan are semi-synthetic polysaccharides that have been used extensively as multi-functional nanoparticle systems, and especially in gene delivery applications[34] due to their strong polycationic properties. PLA / PLGA is an attractive polymer for encapsulating hydrophobic and hydrophilic drugs without degradation[35] and providing a mechanism for their release into the target of interest. The manner through which the drugs are loaded into the particles greatly affect the rate of release. PLGA nanoparticles undergo hydrolysis of ester linkages throughout its matrix and advantageously the resulting by products are easily cleared from the body. Tunability of these nanoparticles can be achieved via changing the ratios of lactic and glycolic acid in the synthesis[36]. Overall polymeric nanoparticles offer a great deal of advantages including biocompatibility, low clearance in the body and ease of customization.

Liposome

Liposomes are concentric closed bilayer membranes of water-insoluble polar lipids, which are an important structural component of the cell membrane. Liposomes are amphiphillic in nature, due to being composed of both hydrophobic and hydrophilic

components which leads to the self-assembly into the bi-layer structures[37]. These materials possess many advantages for use as drug delivery systems the first of which is that the surface properties can be easily modified to suit the needs of the system being developed through the addition of targeting functionalization[38] and their size can be precisely controlled[39]. They can also stably encapsulate and protect both water soluble or insoluble therapeutics in the core[40]. Finally due to their organic nature, liposomes are generally biocompatible. Despite these advantages there are drawbacks to using liposomes, including poor stability, low loading efficiency, and poor release profiles.

Dendrimers

Dendrimers[41] are spherical, synthetic structures that are typically composed of a core molecule that branches out into tree like extensions with terminal ends that are available for functionalization. In terms of diameter, dendrimers are the smallest nanoparticle system[42] with radius ranging from 2.5 to 8 nm. Due to the nature of their synthesis, dendrimers offer a high level of control of their branching, molecular weight, charge and functionalization. This allows for drugs to be attached to the branches via the functional groups, can fill in the void spaces between the branches or can be encapsulated in the core presuming it is hydrophobic. Targeting or imaging domains can be attached to the ends through the functionalized groups and because of the shape of the dendrimers these are highly available. These highly customizable features are the most desirable properties of using dendrimers as drug delivery vehicles.

Polymeric Micelle

Nanoparticle micelles are colloids consisting of amphiphillic macromolecules with both hydrophobic and hydrophilic segments[43]. The segments lead to a distinct segmentation of the particles into two regions, a hydrophobic core consisting of polymer tails and a hydrophilic headgroup. Typically the micelles are formed through a process of self-assembly that occurs in a concentration dependent manner known as a critical micelle concentration (CMC). Below this concentration micelles exist as monomers in solution. Micelle nanoparticles typically have a size that ranges from 5-100 nm in diameter. As drug delivery vehicles there are numerous advantages to using micelles as the base particle. Chemotherapeutics can be encapsulated in micelles in multiple ways, including during self-assembly for hydrophobic drugs in aqueous solution, or self-assembly of hydrophilic drugs in non-aqueous solutions. This core shell structure is highly advantageous for using micelles in drug delivery, due to the hydrophobic core which solubilizes drugs and the hydrophilic shell which protects the particles as they travel through the body. Addition of targeting fragments or imaging domains is achievable using micelles, and various studies have shown that micelles are endocytosed via EPR effect or through receptor mediated interactions. Micelles are generally composed of biocompatible materials, which aids in their presence and eventual clearance in the body.

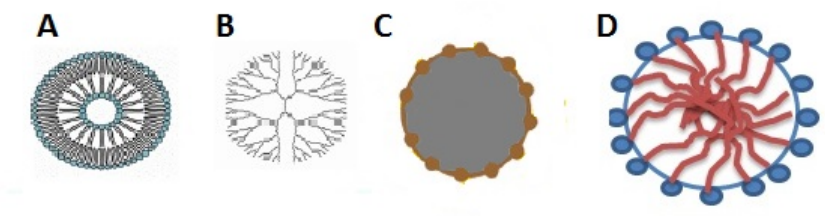

Figure 1.2. Multifunctional nanoparticles used in theranostic systems. A) liposome B) dendrimer C) functionalized polymer D) micelle

1.2. Nanoparticle Drug Delivery Systems

1.2.1. Chemotherapeutics

Choice of the therapeutic agent used plays a very large role in the development of multifunctional nanoparticle systems. A large amount of the design in encapsulating the compound depends on the solubility of the therapeutic, which can either need to be protected or need to have its solubility enhanced. Two of the most common therapeutics that have been encapsulated into micelles are doxorubicin and paclitaxel.

Doxorubicin which is commercially available in a PEGylated liposomal form[44] is a chemotherapeutic drug used in numerous forms of cancer chemotherapy. Due to its wide range of indications, it is one of the most widely used anti-cancer drugs on the market. However, even though it is approved for usage there are a number of adverse side effects associated with its administration. These include common symptoms such as hair loss and vomiting as well as hand- foot syndrome[45] and cardiomyopathy[46]. Doxorubicin's mechanism of action is through interaction with DNA via intercalation[47]. Once this process is initiated the progression of the enzyme topoisomerase, which is necessary to allow DNA to undergo transcription. Through further stabilizing interactions with

topoisomerase II complex, the DNA double helix can't be resealed and thus replication is halted[48].

Paclitaxel belongs to the taxane family of drugs, along with Docetaxel and is derived from the bark of the pacific yew tree[49]. A formulation of paclitaxel that is FDA approved and readily available is known as Abraxane, which is an albumin bound nanoparticle designed to overcome solubility issues with the free drug. Typically the drug is used to treat breast, lung, ovarian and head and neck cancers. Due to solubility concerns mentioned earlier, paclitaxel is an excellent choice for a therapeutic that would benefit from being encapsulated in nanoparticle drug delivery systems. Paclitaxel targets and stabilizes and protects cellular microtubules, which leads to prevention of the normal breakdown of these during the cell division process. Specifically this prevents the progression of mitosis and causes reversion back to the G-phase of the cell cycle[50]. Side effects of administration of paclitaxel directly are related to the use of solubilization agents and typically include nausea, vomiting, rashes and even female infertility[9].

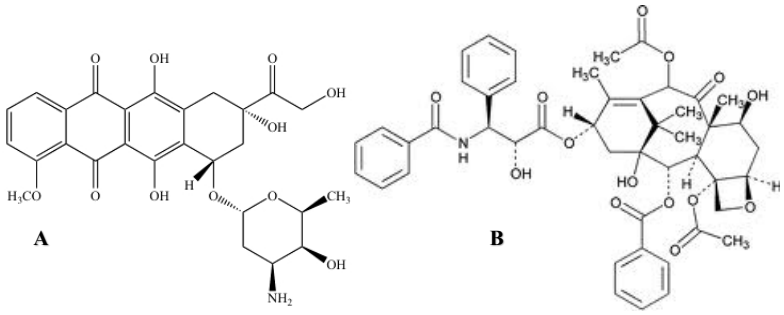

Figure 1.3. Chemical structures of doxorubicin **(a)** and paclitaxel **(b).**

Nucleic acid based therapies such as those utilizing small interfering RNA (siRNA) and mircroRNAs (miRNA) have gained traction in treatment of various forms of cancers. These are known as non-coding RNAs[51], and can be used in theranostic systems.

The miRNAs are conserved single stranded RNAs of 19-25 nucleotides that are transcribed by RNA polymerase II[52] and their abnormal expression is linked to various tumors such as leukemia[53] and lung cancer[54]. They can be used as therapeutic targets since they have been shown to play a role in increasing chemo-resistance of both breast cancer cells[55] and prostate cancer cells[56]. To utilize miRNA as a therapeutic agent two strategies have been employed the first is to block tumor suppressor miRNA and the other is to target the genes involved in their transcription. For utilization in theranostic systems the miRNA can be delivered to target cells by targeted nanoparticle systems, such as using targeted liposomes for delivery of miR-34a into metastatic melanoma[57] and using gold nanoparticles loaded with miR-29b for delivery into HeLa cells[58].

Small interfering RNA (siRNA) is a class of double stranded RNA that is also being utilized in the treatment of cancers. These RNA are typically 20-25 nucleotides in length and are known to interfere with the expression of a gene that shares a complementary sequence with the double stranded DNA[59]. Liposomes decorated with monoclonal antibodies were utilized to deliver siRNA specific to cyclin CD-1 in vivo and were shown to silence the target in leukocytes[60]. Polymer nanoparticles decorated with the integrin ligand RGD have been utilized to deliver siRNA to endothelial cells during angiogenesis[61].

1.2.2. FDA approved Nanoparticle drug carrier systems

One of the most common and important examples of a FDA approved and widely available nanoparticle drug formulation is Doxil, approved for clinical use in 1995 and made by Jansen biotech. This drug is a polyethylene glycosylated liposome drug carrier loaded with the chemotherapeutic doxorubicin used to treat ovarian cancer and

sarcoma[62]. Doxil, unlike the free drug, has been shown to be generally localized to the blood pool, except for at site of increased vascular permeability like the liver, spleen and within tumors. Due to these reasons Doxil has a circulation half-life that is reported to be 100 times longer than free doxorubicin while carrying a risk of cardio toxicity that is seven fold lower[63]. DaunoXome is a formulation of liposomal danorubicin to treat sarcoma that was approved in 1996[64]. Another example of a successful FDA approved formulations is Abraxane, which is albumin bound paclitaxel and used for the treatment of metastatic breast cancer, lung cancer and pancreatic cancer[65]. A list of nanoparticle based formulations that have been approved by the FDA are listed in Table 1.1.

Drug Name	Formulation	Usage	Year Approved
Abraxane	Albumin bound paclitaxel	Breast cancer	2005
Cimzia	PEGylated fragment of anti-TNF-α antibody	Chron's disease and arthritis	2008
Doxil	PEGylated liposomal doxorubicin	Ovarian cancer and sarcoma	1995
DaunoXome	Liposomal danorubicin	Sarcoma	1996
Eligard	PLGH-polymer and leuoprolide formulation	Late-stage prostate cancer	2002
Oncaspar	PEG-L-asparagine	Acute lymphoblastic leukemia	2006
Genexol-PM	PLA-PEG micelle with paclitaxel	Metastatic breast cancer	2007

Table 1.1. Nanoparticle formulations that are FDA approved for clinical use.

For micelle-based system, numerous candidates are currently in clinical trials, and these are listed in Table 1.2. Genexol-PM is a micelle based nanoparticle that was approved by the FDA in 2007 and is polyethylene glycol poly-lactic acid micelle which has indications for use in breast and lung cancer[66]. The micelles that compose the formulation are a range of 20-50 nm in size. Genexol was designed to overcome one of

the major limitations of using paclitaxel as a therapeutic, which is the need for Cremophor-EL, a surfactant solubilization agent used to dissolve the paclitaxel in Taxol[9]. This agent has been linked to hypersensitivity reactions and requires pre-medication for administration. In the case of Genexol-PM, the paclitaxel is encapsulated and protected within the hydrophobic core of the micelle and solubility is maintained through the hydrophilic shell of the micelle. In a phase I study involving this formulation it was found that hypersensitivity reactions were not observed and that the formulation had linear pharmacokinetics[66].

Name	Composition / diameter (nm)	Therapeutic	Usage	Stage
NK105	PEG-P(aspartate) 85	Paclitaxel	Stomach Cancer	III
NK012	PEG-PGlu(SN-38) ~20	SN-38	Breast Cancer	II
NC-6004	PEG-PGlu(cisplatin) 30	Cisplatin	Solid Tumors	II
SPIO49C	Pluronic L61 and F127 ~25	Doxorubicin	Adenocarcinoma	III
NK9111	PEG-pAsp ~40	Doxorubicin	Broad	I

Table 1.2. Micelles currently in clinical trials.

1.3. Targeting Strategies

1.3.1. Passive Targeting

As of now, all clinically administered and approved nanoparticle formulations are delivered to the site of interest in the body through passive targeting via the enhanced permeability and retention (EPR) effect[14]. This phenomenon was developed by Maeda et

al. after observing a higher concentration of colloidal particle drug conjugate in tumor tissue as compared to free drug[67] which was described as being due to irregularities in the tumor tissues themselves. These irregularities include a highly leaky vasculature which allows particles to enter into tumor from surrounding tissues[68] and the lymphatic drainage system is ineffective which leads to an entrapment of particles and prevents their clearance. Various classes of nanoparticles, most effective when the size is between 10-100 nm in diameter, have had their tumor interaction behavior described via the EPR effect including, micelles[21], liposomes[69] and polymer nanoparticles[70] and nanosized materials up to 400 nm in diameter. Various studies in animal models have shown that the EPR effect can lead to a 50 fold accumulation in tumors compared to healthy tissues[4] and further the greater the circulation time of the particles the greater the accumulation. However there are drawbacks to solely relying on the EPR effect for passive targeting, such as the fact that many large tumors are known to be heterogeneous in nature, which prevents the particles from accumulating throughout the tumor. Further the EPR effect is negated in the central regions of the tumors which further reduces the accumulation of the particles[71]. Also the negative pressure gradient that exists in the tumoral interstitial space has the potential to limit the movement from the intravascular to extravascular space, thus negating the advantages of the leaky tumor vasculature[72]. Another drawback is that not every type of tumor will allow for accumulation via the EPR effect, including gastric and pancreatic cancers[73].

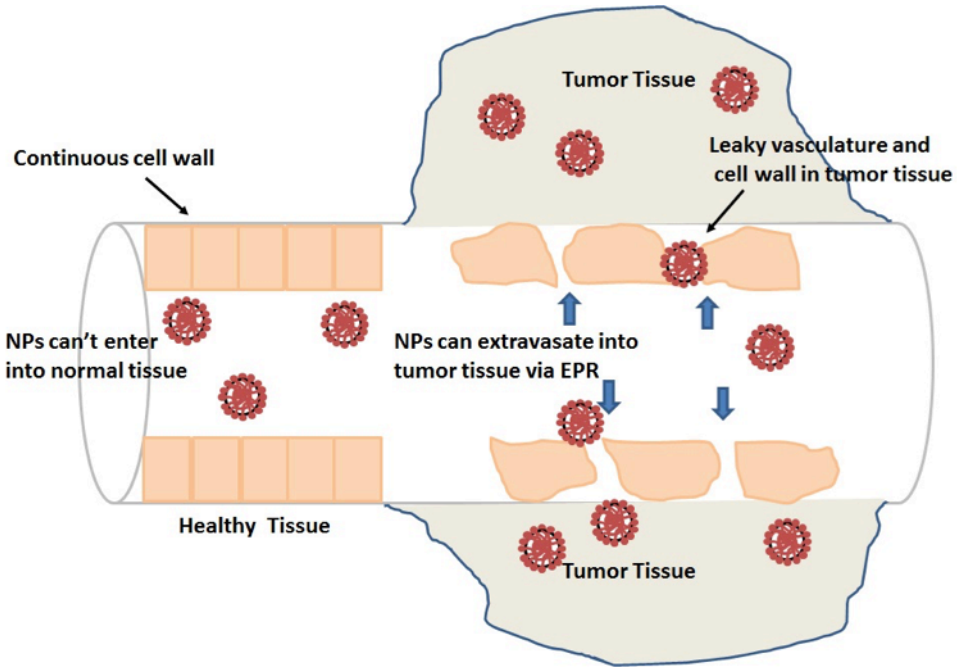

Figure 1.4. Passive targeting via the EPR effect.

1.3.2. Active Targeting

As an alternative strategy to relying solely on passive targeting through the EPR is to use active targeting strategies that rely on affinity ligands which will directly bind nanoparticles to the over-expressed receptors on tumor surfaces[74]. This is achieved by decorating the surface of the nanoparticles with these targeting elements. The origins of active targeting are derived from modification of the surfaces of liposomes with monoclonal antibodies that were designed to recognize antigens present on target cells[75] and there are over 30 of these compounds approved to date. The most recognizable of these is known as Herceptin (trastuzumab), which is used in the treatment of breast cancer through the biding of the HER2/neu antigen[76]. Many types of targeting ligands have been developed including antibodies, peptide fragments, nucleic acid ligands and biomarkers. Short peptide fragments possess advantages over larger antibody fragments

due to the fact they are inherently smaller, less immunogenic, possess more stability and are far less complicated to manufacture[77]. Although peptide targeting tends to have lower affinity for the target cells than antibodies, this issue is overcome by the fact that the nanoparticle surface is entirely decorated with the peptide targeting fragments, which leads to a situation where the peptides can achieve avidity. The development of a wide library of peptides has been facilitated through the use of phage display[78].

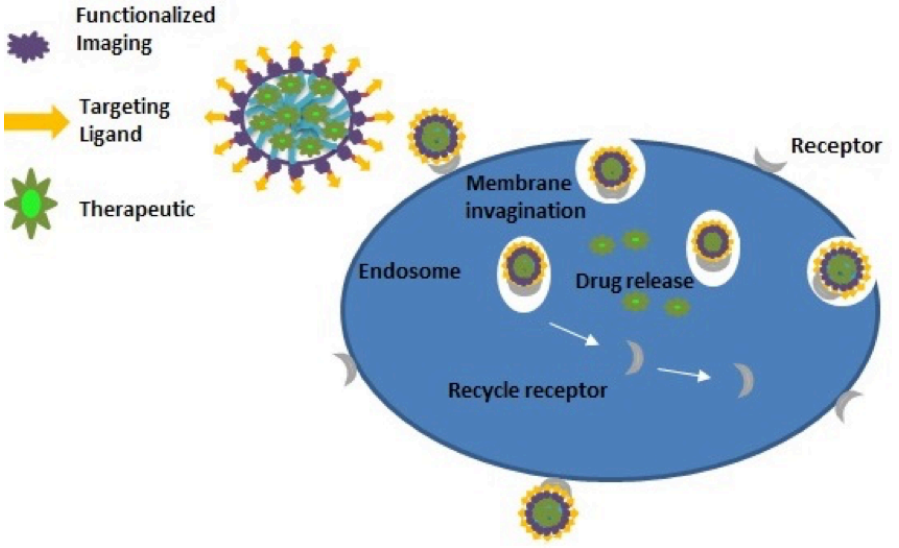

Figure 1.5. Internalization of nanoparticles via receptor-mediated endocytosis.

Despite the advantages of active targeting, there are only 6 known targeting nanoparticles that have advanced to the state of reaching clinical trials, three of which are polymers[79] and three are liposomes[80]. Each of these compositions has demonstrated thus far an enhancement in activity as compared to non-targeted versions. These are presented in Table 1.3.

Code	Targeting fragment	Particle Composition	Usage	Therapeutic	Phase
MBP-426	Transferrin	Liposome	Gastric, adenocarcinoma	Oxaliplatin	II
SGT-53	Antibody tumor antigen transferrin	Liposome	Tumors	P53	Ib
MCC-465	Antibody fragment	Liposome	Stomach cancer	Doxorubicin	I
SEL-068	Antigen	Polymeric	Nicotine antigen, TLR agonist		I
Bind-014	PSMA	Polymeric	Solid tumors	Docetaxel	I
CALAA-01	Transferrin	Polymeric	Solid tumors	siRNA	I

Table 1.3. Active targeted nanoparticles in clinical trials

1.3.3. Types of targeting ligands

Antibody

This class of targeting ligand is the only that is currently clinically available and has consistently demonstrated increased cellular uptake as compared to non-targeted particles. This is most like due to the fact that antibodies have two epitope binding sites on the same molecule, which offers high selectivity and affinity towards the target[81]. Clinically available AB targeted nanoparticles include, Rituximab for lymphoma[82], Trastuzumab for breast cancer treatment[76], Bevacizumab used to inhibit angiogenesis[83] and Cetuximab for the treatment of advanced colorectal cancer[84]. These large monoclonal antibodies however, have drawbacks that limit their desirable use in the laboratory. These include their large size which can affect particle diameter, instability in solution making self-assembly processes difficult, batch to batch variations and immunogenicity concerns. To overcome these limitations, small fragments of antibodies have been utilized, known

as affibodies that are used in combination with phage display to target specific cell markers[85].

Folate Receptor

The folic acid receptor (FR) is overexpressed in many kinds of cancer cells including breast, bone, lung, head neck and brain and is one of the most studied receptors in active targeting[86]. Folic acid is a vitamin that is necessary for cell function and provides required components for the synthesis of DNA. Although the FR is present on normal healthy cells, it presents low affinity for nanoparticles carrying folic acid conjugates[87]. An example of the efficacy of the targeting is demonstrated by Lacroix et al. who conjugated folate onto poly(L-lysine) polymers with encapsulated doxorubicin[88] and showed enhanced toxicity compared to non-targeted nanoparticles. Using folate as the targeting ligand has numerous advantages including the fact that it is easily conjugated to particles and has high binding affinity for the folate receptor. Further it is inexpensive, non-immunogenic, readily available and conjugation chemistry is simple.

Transferrin

Transferrin is an antibody that operates via transferrin receptor mediated endocytosis, through the binding of iron and transportation into cells. Cancer cells, being highly proliferative, have a need for tremendous amounts of iron during their growth periods which leads to an overexpression of the transferrin receptor[89]. These receptors are overexpressed on tumor and metastasizing cells by approximately 2 to 10 fold compared to healthy cells[90]. Labhasetwar et al. used the transferrin receptor to decorate particles with transferrin and loaded with paclitaxel to demonstrate an increase in an anti-proliferative activity[91]. The advantages of using transferrin are that it is completely

biocompatible due to non-immunogenicity, can be easily conjugated to many particles and drugs and the acquisition is easy.

Peptides

Peptide targeting fragments are molecules that range in size from 2 to 50 amino acids linked by peptide bonds[92]. There are numerous peptide receptors overexpressed in tumor cells, which gives a large variation in the targets that are available and these include luteinizing hormone-releasing hormone (LHRH), bombesin receptor, and somatostatin. Peptides are also used as ligands to target integrins, which are transmembrane receptors, whose role is vital in the adhesion between cells and surrounding tissues. These are commonly overexpressed in tumor neo-vasculature[93]. The most common of these integrin receptors that is targeted is $\alpha_v\beta_3$, which is overexpressed on endothelium of cancerous tissues and is selectively targeted by the peptide RGD[94]. Zhan et al. used PEG-PLA micelles conjugated with cyclic RGD and loaded with paclitaxel to show an enhanced anti-glioblastoma effect by 2.5 times compared to non-targeted micelles[95]. Peptides as targeting ligands possess many desirable features including the fact that they small in size, can be excreted through normal pathways, have high binding affinity and their small size enhances the avidity effect on surface on nanoparticles, they have high stability and are easy to reproduce.

1.3.4. Targeting ligands for Prostate Cancer

Prostate cancer is one of the most diagnosed cancers in males with an estimated 233000 new cases being estimated for 2014 or 27% of new cases with 29,480 deaths resulting from it (~ 8%)[1]. Prostate cancer incident rates however have been declining, and this is partly due to early detection improvement, but it is still the second leading cause of

cancer death among males behind lung cancer[1]. When detected early there are a number of treatment options which can include radiation therapy or removal of the tumor. However, once the cancer has begun to metastasize it becomes resistant to removal and becomes incurable[96]. Currently there is a need for treatment options that will enhance the efficacy of care for late-stage prostate cancer. Unfortunately prostate cancer is a difficult disease and no wide reaching strategies have proven successful, mostly due to the fact that the tumors themselves display a high level of heterogeneity[67]. This however, presents an opportunity for theranostic formulations to provide personalized treatment regimens to enhance the chances for success.

Active targeting strategies

Two clinical trials have been performed in the last few years on actively targeted nanoparticles for the treatment of prostate cancer, SGN-15 and ASG-5ME. SGN-15 is an antibody conjugated nanoparticle loaded with doxorubicin and Docetaxel which was completed in October 2011[97]. ASG-5ME targets a transmembrane antigen and delivers an anti-microtubulin drug known as MMAE. This study was completed in June 2013[98]. As of the publication of this thesis these are the only two targeted nanoparticle studies on record, indicating that there is a pressing need for new strategies. What follows is a list of possible targeting strategies to guide theranostic formulations in the future including a table listing all the options (Table 1.4).

Prostate Specific Membrane Antigen

The prostate specific membrane antigen (PSMA) is a glycoprotein type II integral membrane that is a common biomarker for prostate cancer multifunctional nanoparticle studies[99]. The common usage of this target is due to it possessing highly elevated

expression levels in a wide range of prostate cancer tumors as well as a high level of internalization when targeted to[100]. When a PSMA antibody complex is formed it has been shown that it will be internalized, eventually ending up in the lysosomes via the clathrin coated pits route[101]. Xu et al. used unimolecular micelles conjugated with aptamers targeting PSMA, composed of a PLA-PEG core and loaded with doxorubicin. These micelles demonstrated a higher level of cytotoxicity than non-targeted constructs[102].

Six-Transmembrane Epithelial Antigen

Six-transmembrane epithelial antigen (STEAP) is a transmembrane protein that is primarily expressed in the tissue of the prostate[103]. This antigen is also highly over-expressed in a variety of tissues including prostate cancer, lung, colon and bladder while there is restricted expression in healthy tissues. Further the overexpression has been shown to exist in metastases of prostate cancer in lymph nodes and in bone[104]. These reasons make it an attractive target for prostate cancer treatments in the future. Currently there is an ongoing clinical trial in phase I, using STEAP I as the targeting ligand to measure the treatments effectiveness in dealing with metastatic castration resistant prostate cancer[105].

Gastrin-release peptide receptor

The gastrin-release peptide receptor (GRPR) is a glycosylated, 7-transmembrane G-protein coupled receptor which belongs to the family of bombesin receptors[106]. It is targeted to by the gastrin-release peptide, a bombesin analogue. This receptor has a broad range of biological functions including exocrine secretion of gastro-intestinal organs and stimulation of smooth muscle contraction. Also, once activated, the receptor stimulates

cell growth and proliferation through activation of several protein and signaling pathways. GRPR is overexpressed in prostate cancer as well as in a variety of other tumors including breast and pancreas[107]. It has been shown that the rate of GRPR expression varies from 63% to 100% in prostate cancer tumors[106]. A recent study was conducted to determine the expression levels and profile of GRPR in the various stages of prostate cancer, including healthy tissue, primary cancer following excision, castration resistant prostate cancer (CRPC) and prostate cancer metastases[108]. This study was conducted from a group of 530 patients and the findings were rather enlightening. GRPR was strongly up-regulated in prostate cancers, especially of lower grade. Further progressed prostate cancer tumors had a tendency to be closer to GRPR negative, while metastases and CRPC displayed lower levels of GRPR expression. These findings are rather important in demonstrating the potential to use GRPR for use in theranostic applications, especially as an early detection and treatment method.

The gastrin release peptide (GRP) is the mammalian counterpart of bombesin and was named for its first known activity of inducing gastrin secretion from G cells in the gastrin antrum[122]. There is a strong similarity between the sequence of GRP and bombesin including an amidated methionine at the C terminal. The 27 amino acid sequence is represented as follows:

V-P-L-P-A-G-G-G-T-V-L-T-K-M-Y-P-R-G-N-H-W-A-V-G-H-L-M-NH2

The 10 amino acid C terminal fragment is identified as the most similar to bombesin and is used as the targeting fragment for active targeted prostate cancer applications

G-N-H-W-A-V-G-H-L-M-NH2 (GRP)

Glu-Gln-Arg-Leu-G-N-Q-W-A-V-G-H-L-M-NH2 (Bombesin)

Two examples of using the gastrin release peptide targeting fragment are presented. Steinmetz et al. demonstrated active targeting utilizing the GRP peptide fragment with viral nanoparticles of tobacco mosaic virus[109]. This system demonstrated enhanced binding to GRPR positive pC3 cells compared to non-targeted nanoparticles. Hosta-Rigau et al. used gold nanoparticles functionalized with GRP to demonstrate enhanced binding and uptake in GRPR positive HeLa cells as compared to the non-targeted version[110]. These results lay the groundwork for the active targeting strategies used in this work.

Type	Ligand	Receptor	Indications
Peptides	Gastrin release peptide	Gastrin release peptide receptor	Prostate
	NGR	APN / CD13	Angiogenic endothelial cells
	RGD	$\alpha_v\beta_3$ integrin	Melanoma, breast, prostate, ovarian, glioblastoma
	VEGF	VEGF receptor	Endothelial cells
Antibodies	Mab A7	Antigen A7	Colorectal
	Anti-HER2 scFv	ErbB2	Breast, ovarian, stomach, uterine
Small Molecule	Folate	Folate receptor	Ovarian, renal, lung, breast, brain, pancreatic
	Galactose	Asialoglycoprotein receptor (ASGP-R)	liver
Protein	Transferrin	Transferrin receptor	Colon, breast, kidney, lung, stomach ovary
	PSMA	Solid	Prostate
	EGF	EGFR	Lung, anal, glioblastoma, NSCLC

Table 1.4. Active targeting strategies for multifunctional nanoparticles.

1.4. Imaging Techniques

In order to effectively utilize the theranostic nanoparticles for diagnostic purposes molecular imaging is required to characterize biological processes at the cellular and subcellular levels. Utilizing disease state specific targeting these modalities aided by contrast agents or molecular probes can help to detect different disease states at various stages of progression or be utilized to evaluate the efficacy of treatments. In order for the imaging modalities to be utilized in theranostic systems they must not interfere with nanoparticle self-assembly or alter the nanoparticle scale of existing particle systems upon their inclusion. The successful utilization of these modalities requires there to be a sufficient accumulation of the contrast agents, which is aided by both the nanoparticle size and the disease state specific targeting.

1.4.1. Optical Imaging

Optical imaging utilizes photons emitted from bioluminescent or fluorescent probes to detect disease states. It is considered to be an attractive option for imaging due to its high sensitivity, lack of nonionizing radiation, ability to image the spectrum from visible to near-infrared, ability to image in real time and it is inexpensive to detect the photons[111]. Disadvantages of using optical imaging techniques are poor tissue penetration, susceptibility to noise due to scattering, and potential auto-fluorescence[112]. Probes used for this imaging include synthetic fluorophores, semiconductor fluorescent crystals, and lanthanide based probes. Choi et al. utilized PEGylated hyaluronic acid nanoparticles with a near-infrared fluorescent dye (Cy 5.5) loaded with irinotecan as a theranostic agent[113]. This system was able to selectively target, treat, and image colon cancer tumors *in vivo*.

A common probe used in optical imaging is quantum dots which have the advantage of being able to have their fluorescent properties tuned in any number of ways[114]. Tan et al. used quantum dots as a contrast agent encapsulated in chitosan nanoparticles that utilized HER2/neu siRNA for targeted delivery to HER2 overexpressing SKBR3 cancer cell lines and demonstrated the ability to specifically target these cells as well as gene silencing behavior that was monitored via the quantum dots[115]. Despite the advantages their utility may be hampered by cytotoxicity concerns[116].

1.4.2. Computed Tomography

Computed tomography (CT) is used to primarily provide anatomical information which is provided due to the differences in X-ray attenuation of different biological components such as bone, muscle, fat, water, and air. CT scans can provide very good spatial resolution while producing a 3-D image of an area of interest in great detail, with less radiation present than other techniques[117]. When utilized in conjunction with a nanoparticle platform clearance rates are reduced while allowing the system remain in the blood for a longer period of time, without releasing high doses of the contrast agent prior to clearance[118]. Materials used as the nanoparticle platform include core-shell, liposome, gold, dendrimer, and bismuth. Zhu et al. recently synthesized multifunctional dendrimer entrapped gold nanoparticles linked with alpha-tocopheryl succinate and folic acid as a theranostic agent utilizing CT as the contrast agent[119]. Targeting CT imaging of cancer cells was demonstrated both in vivo and in vitro while the system displayed therapeutic efficacy. Rabin et al. demonstrated the use of long circulating bismuth nanoparticles as an injectable CT contrast agent[120]. This system showed high stability at high concentrations, a prolonged circulation time and the ability to image mice *in vivo*.

1.4.3. Radionuclide Imaging (PET / SPECT)

For molecular imaging purposes radionuclide-based techniques are utilized, such as positron emission tomography (PET) and single photon emission computed tomography (SPECT). SPECT utilizes a camera to detect a dosage of γ radiation that is emitted from the tissue of interest upon administration. Radionuclides such as Tc-99m, I-131 and Ga-67 are typically administered and left to circulate in the blood[121]. Attaching these radionuclides to a nanoparticle platform with both targeting ligands and drug for use as a theranostic platform aids in directing it to appropriate tissue areas. After the nanoparticle platform has accumulated gamma detectors are employed and rotated around the body, which can aid in pin-pointing the location that is emitting the largest concentration of γ rays. Further this can provide a 360 degree image and combinations of these images can produce three-dimensional images of the area[122]. Advantages of using SPECT include the fact that it is quantitative which allows for precise measurements, little background interference, require no signal amplification, less expensive than PET, long half-lifes of radionuclides, multiple radionuclides can be detected at once, and has high sensitivity[123]. Disadvantages include a low spatial resolution in comparison to other techniques, high costs, and use of radiation and relatively cumbersome size of detection equipment[122]. Using SPECT as a contrast agent in theranostic nanoparticles has been achieved by Kao et al.[124]. Gold nanoparticles were labeled with I-131, conjugated with epidermal growth factor receptor to target specifically to A549 human lung cancer cells and C225 monoclonal antibody. The specific binding and uptake of the particles was confirmed as well as the therapeutic activity of the theranostic in mice models. Significant accumulation of the contrast agent was also visible in the mouse model.

Positron emission tomography (PET) also utilizes radionuclides and their emitted γ rays to produce images. Radionuclides utilized include In-111, Cu-64, and F-18, which are more expensive to produce and have a shorter half-life[125]. In contrast to SPECT, the radionuclide emits a positron that travels a short distance to interact with an electron before producing two γ rays which are then detected by two cameras in opposite directions which are set to specific time intervals[126]. An advantage of using PET over SPECT is that it directly produces a three-dimensional image, has higher sensitivity than SPECT and requires low concentration of radionuclides to produce an image. Disadvantages of using PET include spatial resolution limitations, cost of the equipment, can only image one radionuclide at a time, and radiation concerns are present[127]. Chen et al. synthesized biocompatible mesoporous silica nanoparticles for use a PET contrast agent[128]. These PEGylated particles were 80 nm in diameter and targeted to breast cancer tumors using a TRC105 antibody which effectively accumulated in the tumor *in vivo*. This system also delivered doxorubicin effectively and was able to monitor the progress of the system.

1.4.4. MRI Imaging

Magnetic resonance imaging is a prevalent diagnostic imaging technique that is used primarily for acquiring high resolution anatomical images in the body while providing excellent contrast with sub-millimeter resolution. It is also used for the determination of physio-chemical states and functional MRI can give detailed neurological information. MRI has many advantages over other imaging techniques such as X-ray and computed tomography, including the fact that it is non-invasive and uses non-ionizing radiation to acquire images. The image produced is 3 dimensional and

acquired through differing relaxation times between physiological tissues. The differences in these relaxation times can be either longitudinal (*T1)* or transverse (*T2*) and are used primarily for the purposes of generating a large amount of image contrast.

MRI relies on the magnetic properties of the hydrogen atoms present in water molecules, which have one proton and possess non-zero spin and is abundant in the body with a large magnetic moment. Hydrogen atoms can then interact and be influenced by external magnetic fields and radio waves. In a normal situation hydrogen atoms have no net magnetization, due to the low energy state and exist in a completely random orientation. Upon the application of a strong magnetic field, such as those present in MRI systems, the hydrogen protons will obtain a new orientation and orientation that can be parallel or anti-parallel. This magnetic field imposes torque on the magnetic moments of the nuclei, which forces them to remain at these angles proportional to the magnetic field B_0. The magnetic moments of the nuclei wobble around the axis with a given frequency, which is known as precessional motion and the frequency is called the Larmor frequency (ω). This equation is represented by:

$$\omega = B_0\gamma$$

When a radiofrequency pulse is applied by the instrument perpendicular to the magnetic field the water protons transition between high and low energy levels and this causes the water protons will deviate from their orientation with B0. The radiofrequency pulse is then removed and the aligned water protons will return to their original orientation with the magnetic field, which is known as relaxation. This phenomenon is the driving force behind MRI creating useful images and MRI signals are controlled by the rates these protons return to equilibrium. After this process is completed protons relax

through two simultaneous mechanisms, spin-lattice or longitudinal relaxation (r1) and spin-spin or transverse relaxation (r2). Longitudinal relaxation, T1, time is the recovery of net magnetization along the z-axis after the removal of the radiofrequency pulse. This is a first order process and the T1 is the time required to recover ~63% of the net magnetization of M0 and is represented in the following equation:

$$M = M_0(1 - e^{-\frac{\tau}{T1}})$$

The transverse relaxation (T2) is the loss of transverse magnetization, measures the time it takes for a nucleus to go from high to low energy state and is a much weaker signal than T1. The T2 is the sum of the magnetic moments of many nuclei as they precess, which eventually cancel each other out. The T2 is the time required for 37% of the transverse magnetization to decay from its original value I0 and is represented by the following equation:

$$I = I_0(1 - e^{-\frac{\tau}{T2}})$$

T1 weighted contrast is the primary mechanism of acquiring images with positive contrast in MRI. Factors that control this are the repetition time (TR), which is the time interval that exists between two successive excitation pulses. In order to generate T1 weighted contrast, a short TR is required, which allows tissues with short T1 to relax quickly before the next radiofrequency pulse and give large signal intensities. Tissues that have long T1 times will therefore undergo a small amount of relaxation during this time and give little to no signal intensity.

Pulse sequences in MRI are a very important part of MRI and are typically applied in specific order that are vital in generating an image. There are two main

methods used to obtain MRI images known as gradient echo and spin echo. Gradient echo sequence is the simplest type of MRI sequence available and consists of series of excitation pulses, which are separated by a repetition time known as *TR*. The data is acquired after the excitation pulses which is a time known as the echo time or *TE*, and is the time between the mid-point of the pulse and the mid-point of the data acquisition. The amount of contrast in the image can be altered through changing the *TE* and the *TR* times. Advantages of the gradient echo sequence are fast image acquisition, a low flip angle and requires less radiofrequency power. Disadvantages of using gradient echo are that it is difficult to generate *T2* contrast and is sensitive to susceptibility effects. The spin echo sequence is very similar to the gradient echo, except for the fact that there is a 180 pulse applied at *TE* / 2. The advantages of using spin echo are that it is useful for *T2* weighting, has high signal to noise ratios and minimal susceptibility effects. Disadvantages include ling scan times, which are costly and it requires more radiofrequency power.

In order to actually determine the *T1* pulse sequences are utilized, such as inversion recovery, saturation recovery and the null method. The inversion recovery pulse sequence is the most frequently used method to determine *T1*. For the purposes of the work presented here, gradient echo sequences only were used due to the short scan time and high contrast provided in *T1* weighted imaging. Fat has a short *T1* due to its slow tumbling rate and gives very bright images in *T1* weighted images. Water on the other hand has a long *T1* and appears dark on *T1* weighted images. If a short *TR* is applied there will be sufficient difference in contrast between the two, while in the case

of a long *TR* they will both be recovered before the next pule and there will be no differentiation in contrast.

Type	Probe	Sensitivity[111]	Nanoparticle Partner	Targeting Ligand$_1$
Magnetic Resonance Imaging (MRI)	Gadolinium (DTPA / DOTA)	10^{-3}-10^{-5}	Iron Oxide Nanoparticles	GD2 Antibody
			Lipid	Folic Acid
			Dendrimer	Folic Acid
			Micelle	LCP
Nuclear Imaging (PET / SPECT)	Radionuclides F-18, In-111, Cu-64	10^{-10}-10^{-12}	Micelle (SPECT)	Folic Acid
			Gold (SPECT)	RGD
			Silica (SPECT)	RGD
			Gold (PET)	CANF
			Silica (PET)	RGD
Computed Tomography (CT)	Iodine	Unspecified	Gold	GRP
			Gold	Aptamer
			Dendrimer	Folic Acid
			Bismuth	Peptide
Optical Techniques-Biolumescence and Fluorescence	Fluorescent dyes Quantum Dots	Fluorescence 10^{-15}-10^{-17} Bioluminescence 10^{-9}-10^{-12}	Quantum Dot	Aptamer
			Quantum Dot	RGD
			Polymer	Chlorotoxin Peptide
			PEG	Hyaluronic Acid
			Dendrimer	CPP

Table 1.5. Common imaging techniques with targeted nanoparticle platforms

[1] RGD: Arginine-Gylcine-Aspartic Acid, LCP: lung cancer targeting peptide, CANF: natriuretic peptide clearance recepetor, GRP: gastrin-release peptide, CPP: cell penetrating peptide

1.5. Gadolinium based contrast agents

Due to the relatively low sensitivity offered by MRI, contrast agents are needed to aid in distinguishing between healthy and diseased tissues. The water protons in the body have a very high tumbling rate, which gives very poor relaxation rates and weak MRI signals. MRI contrast agents catalytically reduce the rate of relaxation of surrounding water molecules by altering the T1 and T2, both of which greatly affect the contrast of an image, while reducing the signal to noise ratio. This effect is known as the relaxivity of the contrast agent, or its ability to change the hydrogen proton relaxation, and is in general the strongest indicator of how successful the contrast agent is. Typically contrast agents are composed of paramagnetic substances, usually of the lanthanide series. However, at the dosage amounts required to induce contrast in the tissues, these paramagnetic ions are toxic to the body. Thus they must be chelated to form both thermodynamically and kinetically stable complexes to ensure they remain intact in the body. Therefore the design of any MRI contrast agents includes two parts 1) the actual paramagnetic center (i.e. gadolinium) 2) chelating ligand. Of the various lanthanide elements, gadolinium (or Gd^{3+}) is the most commonly used as a paramagnetic center. This is due to the following advantageous features:

1) 7 unpaired electrons in the 3+ state, which imparts a high magnetic moment

2) A longer electronic relaxation time than other lanthanides

3) Exerts the strongest effect on T1

The chelating ligand itself must have a few important characteristics to from a successful contrast agent. The first is that it must be water soluble, for obvious reasons. The second is that they form kinetically stable complexes with gadolinium that are not

susceptible to transmetellation via other metals present in the body. The final is that after chelation occurs the ligand must have positions open for water exchange, which is one of the crucial factors for relaxivity.

1.5.1. Factors affecting relaxivity

There are 4 main factors that affect the relaxivity of MRI contrast agents which are based on the Solomon-Bloembergen-Morgan theory[129] and are represented in Figure 1-4. They are

1) number of coordinated water molecules

2) radial distance

3) Rotational correlation time and molecular diffusion

4) Water exchange rate.

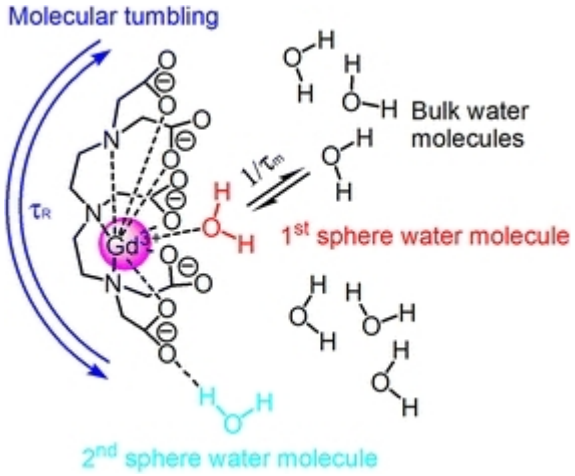

Figure 1.6. Solomon-Bloembergen-Morgan theory of relaxivity. Reprinted with permission from[130]. Copyright 2010.

Number of coordinated water molecules (q)

In the presence of gadolinium there are 3 types of water molecules are associated with the paramagnetic center as represented in figure 1-. These are as follows: 1) inner sphere water molecules that directly interact with the gadolinium. 2) second sphere waters that are bound to the chelating ligand through weak interactions 3) outer sphere water that interacts with the gadolinium due to the tumbling motion of both the water molecules and the ligand / Gd complex. All 3 of these water molecules are necessary to impart the relaxivity offered by the Gd magnetic moment to the surrounding water protons in the environment. Therefore when we discuss the relaxivity of an MRI contrast agent, it is really a combination of the inner sphere and outer sphere water effects. Modification of the binding ligand itself can lead to direct changes in the inner sphere water molecules, as it is directly related to the number of water molecules bound to the gadolinium itself. This is achieved by increasing the hydration number, known as q, which is most commonly a value of 1. Achieving multiple coordination sites on the gadolinium to interact with inner sphere water is a difficult task, however it can greatly increase relaxivity. This is possible because in aqueous form Gd^{3+} can have 8 water molecules coordinated in its first sphere, and while chelated by a ligand those 8 sites are coordinated leaving one free for water molecule binding. Altering the design of the contrast agent allows for alteration of q.

Radial distance

The distance between the paramagnetic center and the bound water molecule plays an important role in the relaxivity of a contrast agent. The relaxivity is proportional to $1/r^6$ (with r being the distance) so any increase in distance between the two will

decrease the relaxivity, while a decrease will increase the relaxivity. It has been found that the distance between Gd and water is in the range of 2.5-3.3 Angstroms[131]. If the distance between the

Rotational correlation time (τ_R) and Molecular Diffusion (τ_D)

The rotational correlation time is the time it takes for a molecule to rotate one radian, which is a process that takes picoseconds. This parameter has important implications in relaxivity because it affects the dipole-dipole interactions between the gadolinium and water protons. Increasing the τ_R will have the effect of increasing relaxivity, however at low magnetic field strengths decreased τ_R will affect relaxivity more[132]. τ_R is also affected by the molecular tumbling rate with lower tumbling rates leading to increased relaxivities. There are numerous ways to increase the τ_R but the most important is through attaching the contrast agent to a protein or macromolecular based carrier with high molecular weight. It was found that increasing that with increasing generations of a dendrimers-Gd complex the relaxivity increased correspondingly[133].

Water Exchange Rate

Water exchange between the chelated gadolinium in the ligand and the surrounding water molecules needs to be a fast process due to the fact that the effect of the relaxation is transferred from the gadolinium center to the surrounding water protons. Water exchange that is too fast is actually a detriment to creating high relaxivity contrast agents, because the water protons will experience a short residence lifetime in the gadolinium bound to the ligand. This means that it does not actually get relaxed, which

will mean no relaxivity occurs. Conversely if the water exchange is too slow, not enough of the water protons will experience the effect of the gadolinium.

In summary for the design of a good contrast agent with high relaxivity, the contrast agent should have fast water exchange, molecular correlation time must be optimized depending on field strength and the hydration number should be as high as it can be designed without sacrificing stability of the contrast agent.

1.5.2. Clinically approved MRI contrast agents

Currently all clinical gadolinium contrast agents used for T1 weighted imaging are based on either of the two following organic ligands. The first is based on diethylenetriamine derivatives, known as gadopentetic acid with the chemical formula ($C_{14}H_{18}N_3O_{10}$). This was used to create the first MRI contrast agent in 1988[134] and these contrast agents form linear structures. Upon complexation with hydrated gadolinium ions, the ligand is very flexible and rapidly wraps around the Gd^{3+} ion and leaves only a single inner sphere water molecule. The complexation reaction is very quick and the stable product is formed in seconds.

The others are based on 1,4,7,7-tetraazacyclododecane-1,4,7,10-tetraacetic acid, which is commonly known as DOTA and has the formula $(CH_2CH_2NCH_2CO_2H)_4$. This compound is a twelve membered tetraazamacrocyclic derivative and contrast agents formed from these are macrocyclic structures. When Gd^{3+} is complexed to the ligand there is an intermediate formed first with 4 to 5 water molecules remaining in the inner sphere, but this ligand is more rigid and thus takes much more time to form the final complex.

Another class of contrast agent are blood pool agents which are magnetic resonance angiography contrast agents. These agents reversibly bind with circulating albumin in the blood which affords them higher molecular weight and higher relaxivities due to shorter T1 relaxation times. Their primary advantage is that they don't diffuse through the vascular system which allows them to stay in the blood for a longer period of time and allow for longer imaging windows, which in turn can result in better signal to noise ratio. One example of a FDA approved agent is known as Vasovist (or MS-325), which binds to human serum albumin and has been shown to effectively enhance blood vessels[135].

Both of these ligands have several chelating arms and have an octadentate orientation of the ligands as well as coordination numbers of 9 with Gd ions with the last coordination site being occupied by a single water molecule (q=1), which is vital for creating contrast. These contrast agents, although widespread in use and applications have a number of drawbacks. One of the main ones is that upon intravenous injection they tend to diffuse to the extravenous area due to their low molecular weight. Another issue is that they are non-specific and are rapidly cleared via renal excretion. These contrast agents also have maximized relaxivities around 5 $mM^{-1}s^{-1}$ and require high dosages to have effective contrast. A list of FDA approved contrast agents is presented in Table 1.6.

Trademark Name	Active Component	Structure	*R1* (mm-1s-1)	USage
Dotarem	Gd-DOTA	Macrocyclic	4.2	Extracellular
ProHance	Gd-HP-DO3A	Macrocyclic	4.4	Extracellular
Gadavist	Gd-BT-DO3A	Macrocyclic	5.3	Extracellular
MultiHance	Gd-BOTPA	Linear	6.7	Extracellular
Optimark	Gd-DTPA-BMEA	Linear	5.2	Extracellular
Magnevist	Gd-DTPA	Linear	4.3	Extracellular
Omniscan	Gd-DTPA-BMA	Linear	4.6	Extracellular
Vasovist	MS-325	Linear	19	Blood-pool
Primovist	Gd-EOB-DTPA	Linear	7.3	Liver

Table 1.6. List of FDA approved MRI contrast agents. Also presented are their relaxivities ($mM^{-1}s^{-1}$) and location of action.

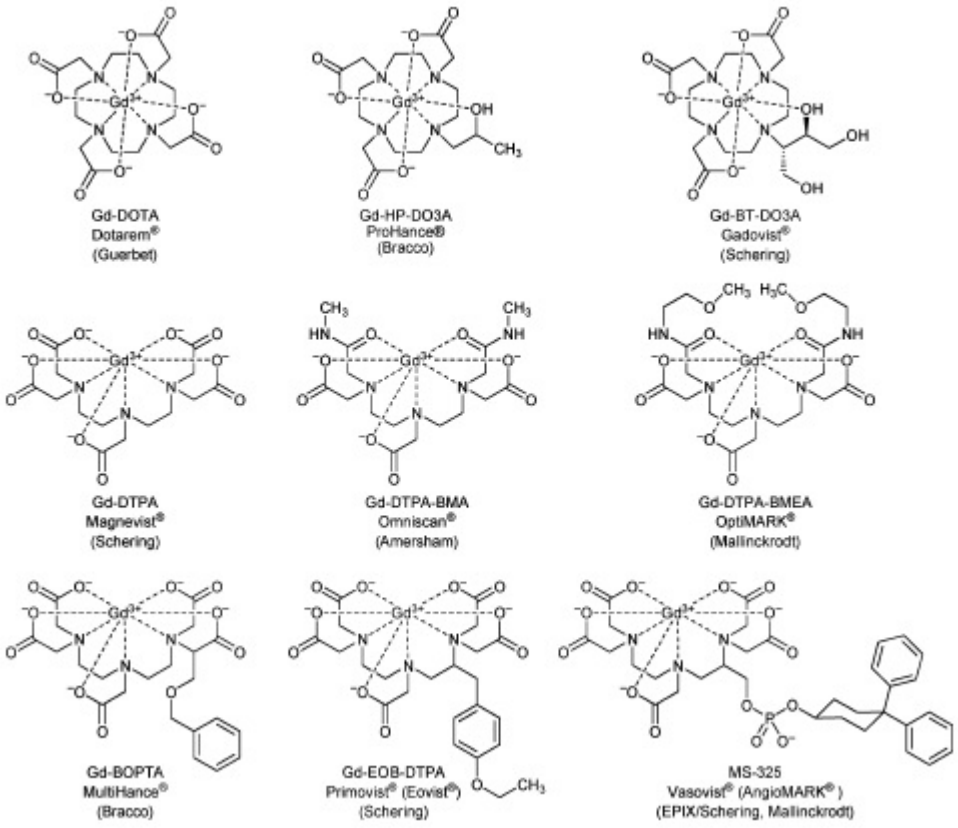

Figure 1.7. Structures of FDA approved MRI contrast agents.

1.5.3. Protein Based MRI contrast agent CA1.CD2

Due to the limitations with FDA approved MRI contrast agents much focus has been given to developing new and improved versions of contrast agents. Requirements for a contrast agent design are to create ligands that have high relaxivity values, low dosage requirements, display high affinity for gadolinium over physiological metals, present no toxicity issues, long retention times in the body which reduces the need for repeated dosage and finally the ability to be cleared through the bodies normal mechanisms. In order to design new contrast typically the factors that affect relaxivity (as discussed in section 1.) are altered with the most common being the number of hydrated

waters and the τ_R. Strategies that alter the τ_R are most commonly to conjugate chelating ligands to protein complexes, which has the effect of increasing molecular weight and subsequently relaxivity. An alternative method of designing MRI contrast agents was presented by Yang et al.[136] which was to design a gadolinium binding domain directly into a protein host. This protein based MRI contrast agent was known as CA1.CD2 or as it is known now, ProCA1. The host protein scaffold was chosen to be domain 1 of rate CD2, which is a cell adhesion protein found on the surface of T-cells, which is part of the signal transduction pathway. Its structure is composed of 9 β-strands, which forms two layers and has a common immunoglobin fold[137]. This host was chosen due to a variety of features which include; wide range of stability across pH and salt concentrations, and is very resistant to mutations. The chelating ligand was designed into CD2 by addition of a group of carboxyl side chains from the differing β-sheets present as the following amino acid changes from the host CD2 sequence: E15, E56, D58, D62, D64. Further one position of the metal binding site was left open to allow for fast water exchange between the gadolinium bound to the ligand and the bulk water, leading to high relaxivity values (Figure 1-6).

Figure 1.8. Structure of CA1.CD2 protein based MRI contrast agent. Reprinted with permission from [136]. Copyright 2008 American Chemical Society.

Also the designed binding site has very little internal flexibility due to the design being from rigid stretches. The end result of this design is that the protein based MRI contrast agent CA1.CD2 exhibited a per gadolinium relaxivity of 117 $mM^{-1}s^{-1}$ which is 20 fold greater than Gd-DTPA contrast agents. The τ_R was found to be ~10ns. Also this domain displayed very strong selectivity for Gd^{3+} over physiologic metals as well as no acute toxicity to cells with a Kd of 7.0×10^{-13} for Gd^{3+}. Contrast was maintained in animal models for a prolonged period of time, which has the effect of using this contrast agent for long procedures without the need for repeated injections. Enhanced contrast to noise ratio was also achieved at a 35 lower dosage than Gd-DTPA. Finally the contrast agent was cleared through the kidneys.

This domain has been modified extensively for enhancing its functionality. A HER-2 affibody[138] was fused to the C-terminal of ProCA1 and the results showed that this construct was able to impart significant contrast enhancement on SKOV-3 tumors at a 100 fold lower dose. Also the targeted construct was able to cross the endothelial boundary and had an even tissue distribution with problem retention time in tumor models. Another modification showed that by adding various sizes of PEG chains to the contrast agent the bio-distribution and blood retention times {157}}. These results taken as a whole show that the protein based MRI contrast agent ProCA1 is amenable to modification and maintains its excellent contrast agent properties through a variety of changes.

1.6. Nanoparticle based MRI Contrast Agents

Using MRI for accurate diagnosis of disease and as a biomarker is often challenging due to some of the limitations of the MRI modality. One of the first issues is

that diseased tissues have similar T1 times to healthy tissues and thus the need for contrast agents to enhance signal differentiation. The use of nanoparticles as platforms for MRI contrast has opened up numerous avenues for future contrast agent design. Using a nanoparticle base that is less than 150 nm in size will allow for many different things to be loaded into the core or attached to the surface of the particles. Using Gd^{3+} loaded or chelated nanoparticles combined with targeting motifs can help to ensure that disease detection can be done in a quicker and more accurate manner, with a reduced dosage requirement and be a vehicle to overcome any limitations that exist with MRI for diagnostic applications. As discussed earlier a reduced molecular tumbling rate will result in an increased relaxivity, and one of the best ways to achieve that is to attach or conjugate the Gd chelating ligand to a nanoparticle host. When a nanoparticle is used as the base platform for MRI the following advantages are found[139]:

1) Bio-distribution can be improved through surface modification or changing the nanoparticle composition
2) Relaxivity is increased due to a reduction of the tumbling rate
3) The nanoparticles can be modified through the addition of targeting ligands or peptides
4) The nanoparticles can have a large amount of gadolinium present in a small volume which will lead to a reduced dose required for contrast as well as reduction in possible toxic side effects due to free gadolinium

1.6.1. Examples of nanoparticle MRI contrast agents

There are a vast number of nanoparticle platforms available for the design of MRI contrast agents. The overall goal is to enhance the positive properties of the imaging

technique while not causing undue damage to the body. Factors that are important to consider with each class of nanoparticle are biocompatibility, relaxivity values, targeting properties and tenability of the response. What follows is some examples of nanoparticle platforms used as MRI contrast agents.

Liposomal Contrast Agents

Liposomes are defined as spherical vesicles composed of a bilayer of phospholipids that enclose a hydrophilic core and hydrophobic tails. Liposomes have many advantageous properties including biocompatibility, ease of production, prolonged stability, protection of cargo and their size can easily be controlled. However due to the need for water exchange in contrast agents, Gd chelators in the core of liposomes have limited success due to poor permeability[140]. To overcome this Gd chelators have been linked to the surface of the liposomes by linking them to the hydrophobic chains, which would put them on the outside after self-assembly. Kielar et al. synthesized liposomes with a DOTA complex functionalized with two hydrophobic chains to allow for self-assembly[141]. The liposomes were prepared with PEGylation and their diameters were between 45-60nm with r1 values were between 17 and 40 $mM^{-1}s^{-1}$ at 25°C.

Dendrimer Based Contrast Agents

Dendrimers are synthetic semi-biocompatible macromolecules that are well defined, hyperbranched and mono-disperse. They possess multiple free amino acids on their surface which leads to the ability to impart high surface functionality. Various families of dendrimers are used including polylysines, polypropyleneimines and polamidoamines (PAMAM). An easy way to characterize dendrimers is to count the number of tree branches that extend from the central core, known as generations. With

each increase of generation, molecular weight and particle diameter are increased, however this number can't be greater than 10 due to solubility concerns[142]. Also the size of the dendrimer is directly related to the route of clearance, as increased size changes the route from kidney to liver and spleen. Huang et al.[143] developed PAMAM Gd conjugates that were cross-linked to form clusters that contained biodegradable poly-disulfide linkages. This construct had an extended half-life of ~1.5 hour in animal models and high relaxivity of 11.7 $mM^{-1}s^{-1}$ per Gd^{3+}.

Iron Oxide Nanoparticles

Superparamagnetic iron oxide nanoparticles (SPIONs) are contrast agents used in MRI for T2 weighted imaging by providing high quantities of r2 relaxivity. Images produced by SPIONs are negative contrast. SPIONs have an iron oxide core, which is usually magnetitie Fe_3O_4 or mehemite γ-Fe_2O_3 and a polymer coating. One of the major advantages that SPION have is that they have much larger magnetic moments compared to Gd^{3+}. Also they have many unique properties such as a large surface area, quantum effects and ease of modification through surface chemistry[144]. There are generally two main classes first is SPIO and the second is ultra-small SPIO (USPIO). Size of size of SPION's range from between 10-40 nm for USPIO and 40-150 nm for SPION, with mono-dispersity. Various surface modifications of SPION enhance their ability to be tailored at the nanoscale level while enhancing their bio-availability and limiting any potential *in vivo* toxicity potential. Examples of coatings for SPIONs include dextran[145], chitosan[146], PAMAM dendrimer[147], PEG[148] and PLGA[149].

Smejkalova et al. prepared a hyaluronan acid polymeric micelles encapsulating oleic acid coated SPIONs[150]. The micelles had a size of approximately 100 nm and were

able to be loaded with 1-2 wt% SPION. These constructs were able to cluster inside the core of the micelles with high r2 values at low concentrations. Further when injected into tumor cells the micelles accumulated and displayed contrast enhancement. The combination of micelles and SPION can provide powerful contrast agents, with the potential for multi-functionality.

Micelle Based MRI Contrast nanoparticles

Micelles are amphiphillic spherical structures composed of hydrophobic chains and hydrophilic head groups that form in a core-shell manner. They are widely used due to the fact that they are easily prepared, can form uniform size structures, are easily tunable using a variety of methods and are generally biocompatible[151]. Responsive behavior is one of the most attractive features of using micelles as contrast agents, and polymers such Poly(N-isopropylacrylamidee)[152] or PNIPA and Elastin-like polypeptides (ELPs) make attractive candidates for these carriers. The composition of the hydrophobic tail, size and charge of the hydrophilic headgroups and the conditions used to promote self-assembly determine the size, morphology and the surface properties of the micelles. Typically micelles for nanoparticle contrast agents are synthesized by binding the Gd chelating agent to the polymer prior to formation and designed in such a way that during self-assembly the contrast agent is located on the hydrophilic heads of the micelle so it is accessible. Due to this formation water exchange between the chelators and the bulk water is not an issue. Another advantage of this formation process is the macromolecular structure formed in this assembly is extremely rigid. The combination of the high molecular weight which reduces molecular tumbling rate and the ridged structure

increases rotational correlation time, both serve to help increase the relaxivity of the constructs.

An example of a micelle based contrast agent used as a blood pool agent come from Grogna et al.[153]. Micellar contrast agents were developed by forming poly(ethyleneoxide)-b-poly(ε-caprolactone) (PEO-b-PCL) with PEG stealth and a Gd-DTPA contrast agent combination. This construct formed micelles between 14-40 nm with relaxivities of 12 $mM^{-1}s^{-1}$ which is 3 times higher than Gd-DTPA alone. Further the PEG allowed the construct to remain in circulation longer than free Gd-DTPA, which makes it a good candidate for a blood pool agent. Jeong et al[154] synthesized Biocompatible poly-[N-(2-hydroxyethyl)-D, L-aspartamide]-methoxypoly(ethyleneglycol)-hexadecylamine (PHEA-mPEG-C-16) conjugated with 1,4,7,10-tetraazacyclododecan- 1,4,7,10-tetraacetic acid-gadolinium (DOTA-Gd) for use as micelle based contrast agents. These micelles had higher relaxivity values than Omniscan and prolonged circulation time and contrast enhancement in rabbit liver models demonstrating potential for use as a liver disease detection platform.

Shiraishi et al.[155] synthesized macromolecular magnetic resonance imaging (MRI) contrast agents that were composed of poly(ethylene glycol)-b-poly(L-lysine) block copolymer (PEG-P(Lys)) chelated with 1,4,7,10-tetraazacyclododecane-1,4,7,10-tetraacetic acid (DOTA) to create Gd-DOTA micelle contrast agents. These are an example of using oppositely charged blocks that became neutral upon mixing. When the charge changed in solution, there was a noticeable change in the relaxivity of the constructs. Overall the constructs displayed high relaxivity values and enhanced tumor contrast in animal models. Kim et al.[156] recently developed a pH responsive micelle

contrast agent that demonstrated enhanced activity upon a change of pH in solution. Amphiphillic block co-polymers were synthesized out of methoxy poly(ethylene glycol)-b-poly($_L$-histidine)(PEG-p($_L$-His)) and methoxy poly(ethylene glycol)b-poly($_L$-lactic acid)-dietheylenetriaminopentaacetic acid dianhydrdide-gadolinium chelate (PEG-p($_L$-LA)-DTPA-Gd). At physiological pH the micelles have a spherical shape of ~40nm and r1 value of 8.56 $mM^{-1}s^{-1}$. When the pH drops to an acidic value of 6.5, which is representative of the intertumoral environment, the micelles dissociate into positively charge water soluble polymers with an increase of the r1 value to 12 $mM^{-1}s^{-1}$. These results were confirmed through positive contrast enhancement in tumor bearing mice. These two studies show the flexibility of using the micelle platform for contrast agents, with both demonstrating multifold enhancement in relaxivity compared to free gadolinium, as well as the ability to impart responsive behavior.

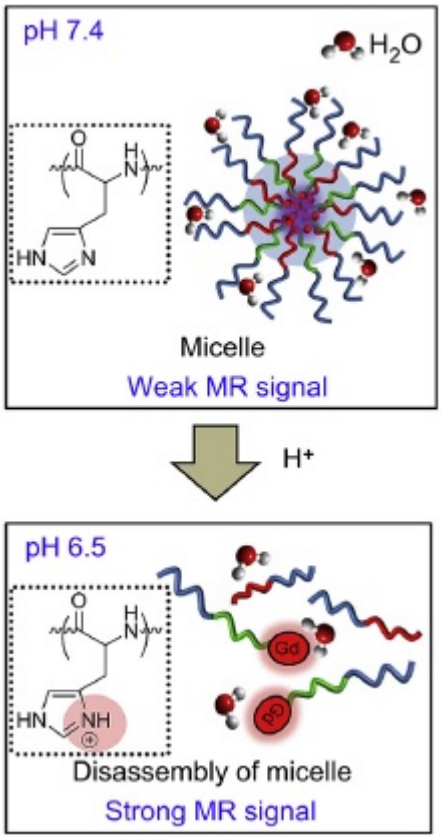

Figure 1.9. Scheme of pH responsive micelle based MRI contrast agents. As the pH drops the micelles dissociate leading to an enhancement of MRI signal. Reprinted with permission from [156]. Copyright 2014

1.7. Examples of micelle based theranostic systems

For the purposes of applicability to the system being presented in this work, this section will focus on examples of micelle based theranostic multi-functional nanoparticles. Liu et al. developed a novel micelle that was a pH sensitive β-cyclodextrin star copolymer functionalized with folic acid for active targeting, DOTA for Gd imaging and loaded with doxorubicin[157](Figure 1.8). This system underwent a process of self-assembly into ~26 nm micelles at pH 7.4 and had an in vitro doxorubicin release profile

that decreased with decreasing pH, accompanied by disintegration of the micelles. The system displayed effective ability to undergo endocytosis and provide cytotoxicity to HeLa cells and had a *T1* relaxivity of 11.4 $mM^{-1}s^{-1}$. When incubated into tumor positive rats, there was a large amount of accumulation of the particles into the liver and kidney of the mice, and positive contrast enhancement in the organs. Overall, this system is a powerful example of how powerful micelle based theranostics can be.

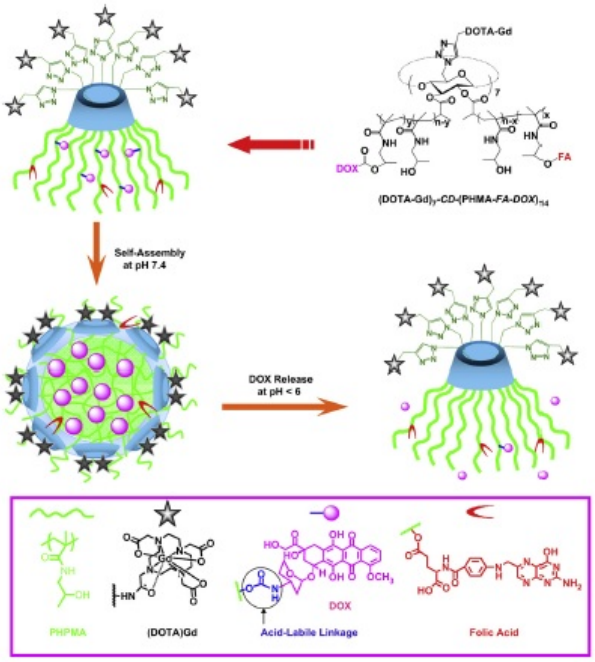

Figure 1.10. Self-assembling micelle for theranostic applications. Reprinted with permission from reference[157]. Copyright 2012 Elsevier.

Another example of a micelle based theranostic formulation was developed by Rowe et al.[158]. These micelles were composed of poly(N-isopropylacrylamide)-co-poly(N-acryloxysuccinimide)-co-poly(fluorescein O-methacrylate), functionalized with an RGD targeting peptide and loaded with methotrexate. These particles were shown to

be biocompatible, provide active targeting, imaging capabilities with a *T1* relaxivity of 33.4 $mM^{-1}s^{-1}$ and cytotoxic effects comparable to the free drug.

Yongjun at al. recently developed a system for combined MRI and treatment of hecpatocellular carcinoma[159]. This system was composed of PLA-PEG-PLL-DTPA, with the DTPA being used to bind gadolinium ions. Paclitaxel was encapsulated into the cores of the micelles and biotinylated alpha-fetoprotein antibodies were linked to the micelle surface. The particles demonstrated uniform size, positive zeta potential and high encapsulation efficiency as well as a *T1* relaxivity of 21.6 $mM^{-1}s^{-1}$ and superior cytoxicity to controls. These examples show that using micelles for theranostic applications allows for a level of superior control over size, shape, release properties and tunable properties.

1.8. Elastin-like Polypeptides as multifunctional nanoparticle systems

From the previous sections it is clear that the following properties are desirable in choosing a material to use as the base for multifunctional nanoparticle design:

1) Biocompatibility and ability to be cleared by the body's normal mechanisms

2) Control over size, charge, physical properties and assembly mechanism

3) Ability to store, protect and release cargo

4) Ease of modification to include targeting ligands, stealth properties or attachment of functional groups

5) Ability to impart responsive behavior to tune response of the nanoparticle

One material that allows for all of these desirable properties to be met is a class of responsive bio-polymers known as elastin-like polypeptides (ELPs). These responsive biopolymers are derived from repetitive hydrophobic human tropo-elastin[160]. ELPs

consist of a repeated sequence of amino acids $(GVGXP)_{n,}$ with the X position being occupied by any of the 20 amino acids except proline[161] and n being the number of pentapeptide repeats. One of the most critical and important features of ELPs, especially as it relates to developing multifunctional nanoparticle systems is the temperature responsive behavior these systems are known to exhibit. This behavior is a thermodynamic inverse phase transition in solution at a specific temperature known as the transition temperature (T_t). Below this temperature ELPs exist as soluble protein chains in solution while above this temperature ELPs are insoluble and eventually form a protein rich phase known as a coacervate. The T_t can be described as a lower critical solution temperature (LCST) and the process is rapid and entirely reversible. Besides temperature, other stimuli can trigger the T_t including solutes[162], pH[163] and light[164].

The use of ELPs has been rather wide spread mainly due to the fact that the behavior of the proteins can be tuned to specific stimuli. In ELP design the T_t can be specifically controlled through design of the system. The concentration of protein, length of protein chains, molecular weight of the ELP and nature of the guest residue can all be controlled to alter the T_t. Salt has a distinct effect on Tt and follows the Hoffmeister series primarily to salt out or reduce the T_t[165] and is also dependent on the concentration of the salt. Molecular weight of the ELP, which is primarily a function of chain length, is inversely proportional to the T_t, so when the molecular weight of the system is increased the T_t will decrease[166]. Also the concentration of the protein follows the same pattern, such that more highly concentrated ELP solutions will have a lower T_t {209}}. When ELPs are designed with specific guest residues that are sensitive to pH, changes in the pH can also alter the T_t[167]. Besides, pH guest residue substitution can alter the

hydrophobicity and hydrophillicity of the system which have dramatic effects on T_t. Substituting guest resides with side chains amiable to functionalization allows for conjugation of various entities to ELPs. With the ease of synthesis due to molecular biology techniques used and the 19 available substitution partners, the number of combinations possible to design a system to meet a specific T_t or T_t stimulus is endless. These combination of factors allow the ELP to be designed to meet specific needs of design for any number of conditions. As mentioned earlier for the design of multifunctional nanoparticle systems a number of requirements must be met. What follows is a breakdown of how ELPs are a suitable candidate.

1) Biocompatiblity: The first requirement is biocompatibility and normal clearance ability. ELPs are considered to be generally biocompatible while inducing minimal inflammatory response and immune effects through numerous studies in animal models[168]. Crosslinked ELP materials were implanted in 18 rabbits and their immune response measured at various time points[168]. It was found that the implants were completely biocompatible with no immune response or inflammation and was stable for a 6 week period. Studies on the degradation properties of ELPs have also been undertaken. Due to the organic, entirely amino acid based composition of ELPs, it has been thought that degradation should proceed without issue to break them down into individual amino acids to be cleared through the body. Numerous studies have been performed to support that assumption and show that ELPs are degraded by the body in a normal fashion[169]. It was found that ELPs of 59.4 kDa degraded at a rate of 2.5 wt%/day after intravenous administration, which means the ELP will not degrade too rapidly to deliver cargo, but will eventually be degraded for full removal.

2) Control over nanoparticle formation and properties: The second requirement is to be able to control the size, shape, charge and other physical properties of the nanoparticles. ELP nanoparticles are designed entirely at the gene level through the use of molecular biology techniques. This gives a level of complete control over the factors mentioned above. ELP nanoparticles are synthesized in many different fashions. The first and most prevalent way to self-assemble ELP nanoparticles is through the use of block co-polymers composed of alternating hydrophobic and hydrophilic blocks. Below the T_t these structures exist as soluble monomers while above the T_t the hydrophobic segments of the ELP become dehydrated and drives the structure into micelle self-assembly. These self-assembled micelle are composed of this hydrophobic segment as the core, with the hydrophilic segment staying hydrated and forms the micelle corona[170]. Variations in the ratios of blocks, as well as altering the T_t of the individual blocks has been found to influence the size and shape of the self-assembled micelles.

Another method to form ELP nanoparticles is to fuse a hydrophobic entity to one end of the ELP. This was first displayed with a hydrophilic segment with attached doxorubicin through a conjugation site at the C terminal[171]. This construct formed stable 40nm particles that were driven by the number of doxorubicin molecules attached and proved to exhibit success as a drug carrier in mouse models. This method is driven by the hydrophobicity of whatever is attached to the system. A study was undertaken to determine how the LogD of the molecules attached affected nanoparticle self-assembly[172] and it was found that a value of less than 1.5 did not induce formation and a value greater than 1.5 does. Therefore the efficacy of the system can be pre-determined by the hydrophobicity of the drug.

Utilization of the protein rich coacervate phase can also form ELP nanoparticles that serve as stable drug depots for large periods of time. The sequence GVGAP was utilized to form a coacervate into slightly larger nanoparticles, however when loaded with bone morphogenic proteins there was a delayed release lasting 14 days[173]. This shows how changing the guest residue changes the nature and characteristics of the particle formed.

Cross-linking of ELP nanoparticles is another way to control the nanoparticles, through stabilization of the structure. Numerous methods have been used to achieve this including chemical[174], photo induced[175] and enzyme induced[176] are available to demonstrate the wide ranges of options available. The degree of cross-linking and density are related directly to ELP design, which can be controlled through amino acid substitution either by the site of crosslinking or the number of crosslinking residues present in the gene. One example of sequence specific crosslinking of ELP comes from Chung et al.[177] where tetrakis(hydroxymethyl) phosphonium chloride (THPC) as a covalent crosslinking agent to react with primary and secondary amines. It was found that lysine provided the best crosslink efficiency in the presence of THPC acid, and thus the ELP was designed to have specific reaction sites. This study demonstrated this chemical as a sequence specific enhancer of hydrogel properties and also showed cytocompatiblity. Lim et al. demonstrated the same principle with THPP acid as well[178]. Glutaraldehyde used as the crosslinking agent was also achieved in a sequence specific manner by Benitez et al.[179]. This ELP was designed again with lysine reactive sites and it was found that after crosslinking of the fibers the sequence specificity of the gene design preserved the position of the targeting residues and provided stable native like mechanics. The

process proceeded in a two-step manner, with the first being a vapor phase initiation in glutaraldehyde followed by a quenching step in concentrated sodium chloride buffer without any glutaraldehyde to complete the reaction.

3) Ability to store and release drug: ELPs are excellent materials to be used as drug delivery vehicles. The first generation of ELP drug delivery vehicles centered on exploiting the thermal behavior of the proteins as a triggering mechanism for release. The idea is to use targeted hypothermia to heat a tumor (40-44°C) to cause the ELP to localize and aggregate at the site of interest using techniques such as ultrasound. The ELP can be designed to have a T_t between body temperature and the heating temperature[180] which will enhance this aggregation behavior. Dreher et al. demonstrated the efficacy of this method through the use of temperature cycling the system[181]. When the ELP aggregates in the tumor vasculature due to focused hypothermia, the local concentration of ELP is increased, and when that temperature is removed the aggregates dissolve into the tumor. This cycling caused the effect of creating a concentration gradient that drove the ELP into the extravascular space of the tumor. Further this cycling cause an increase in the rate of extravasation into the tumor space. This method provides an excellent way of using ELP as delivery vehicles through the use of passive targeting. This method has been proven to also enhance delivery of therapeutic loaded ELP nanoparticles. Doxorubicin loaded ELPs through hypothermia enhanced methods have been shown to have in vivo efficacy against tumor models, with prolonged circulation time, enhanced drug accumulation in the tumor and dose reduction[182].

ELPs are also capable of presenting a dual way of storing therapeutic cargo, with both encapsulation in the micelle core and therapeutic bound to the surface functionalized

corona of the micelles[183]. This sample demonstrated a dual mode drug release pattern with a burst release stage with a half-life of 1.9 hours of the encapsulated drug while the drug that was bound to the functionalized surface displayed a half-life of 57.8 hours. In vivo efficacy was also shown through a reduction in size of tumor growth in animal models as well as a reduction in toxicity as compared to the free drug.

4) Functionalization with targeting ligands: One advantage of the method of constructing ELP multifunctional nanoparticle systems is the ease of which functionalities can be added to the system. Through the use of molecular biology any number of targeting ligands can be added in a seamless fashion. One peptide that was used to demonstrate enhanced uptake of ELPs is known as cell penetrating peptides (CPP), which are non-specific and promote endocytosis. The addition of the SYN-B1 penetrating peptide to an ELP-paclitaxel conjugate that contained an acid sensitive linker was demonstrated by Moktan et al.[184]. This system was able to inhibit cell proliferation in a paclitaxel resistant cell line.

Active targeting peptide mechanisms have also been investigated. Simick et al. used the RGD peptide to target the $\alpha_v\beta_3$ integrin to demonstrate the combination of focused thermal targeting and high-avidity of targeting ELP nanoparticles[185]. This system showed a 14 fold increase cellular uptake compared to non-targeted ELPs as well as greater uptake in the micelle form compared to unimer form. Self-assembling micelles from block copolymers decorated with NGR tri-peptide ligand were developed as well to further demonstrate active targeting of ELPs[186]. Self-assembly of the micelles enhanced the availability of the NGR peptide to selectively targeted tumor vasculature in vivo along with greater retention and extravascular accumulation. Hassouneh et al. showed

multivalent effects of using fibronectin type III domain as a targeting mechanism to the integrin[187] in combination with thioredoxin. The fibronectin type III domain is a 10 kDa 100 amino acid long protein domain that after attachment to the C terminus of ELPs did not disrupt the formation of micelles, which existed between 24 and 37 nm diameter. This system again enhanced cellular uptake and binding in cells that over express the $\alpha_v\beta_3$ integrin when the temperature was above the critical micelle temperature.

5) Design the nanoparticle to have responsive behavior: One of the most attractive feature of ELPs as a class of proteins is the responsive behavior that they are known for. The stimuli responsive nature of the T_t mechanics can be driven by be triggered by a number of stimuli other than temperature including light[164], pH[167] or solution conditions. In order to change the nature of the stimulus usually, the most common method is to change the guest residue in the GVGXP sequence. For instance a model was developed to quantify the T_t as a function of pH, with one group being stimulated in highly basic conditions and the other in highly acidic conditions[188]. Using this knowledge a pH responsive ELP micelle system was developed by Callahan et al.[189].

Another example of using the triggered response of ELP for in vivo drug delivery applications comes from Hassouneh et al who developed a system that formed spherical micelles in the range of 50 nm in the presence of calcium[190]. A calcium binding sequence was inserted into ELP block copolymers that were calcium insensitive, such that when calcium was present in the system in the range of 50-500 mM it drove assembly. This study was motivated by the large difference in calcium concentrations between the intracellular and extracellular spaces.

Thus it is clear that ELPs offer numerous advantages that make them desirable candidates for use as multifunctional nanoparticle systems. Further there are numerous examples of ways to create these systems and how to exploit the advantages offered by ELPs.

1.8.1. Alternative approaches to modify ELPs

Our labs approach to making new ELP constructs was not based on methods that have been reported before. Stemming from the theory of ELP transition behavior new constructs were designed. It is thought that as ELPs go through their thermal transition behavior they move from a random coil state, to three associated chains that then take on the form of type II β-turns. Once an appropriate concentration of β-turns exists in solution they assembled into β-spirals that are stabilized by internal hydrophobic contacts. As more water is removed from the system they take on the form of fibers, which are composed of long triple stranded β-spirals. Eventually if held above T_t long enough these triple stranded ELPs settle into an aggregated phase separated system. This process of dehydration, folding and aggregation (Figure 1-10) is completely reversible and mediated by chain length, concentration and solution properties.

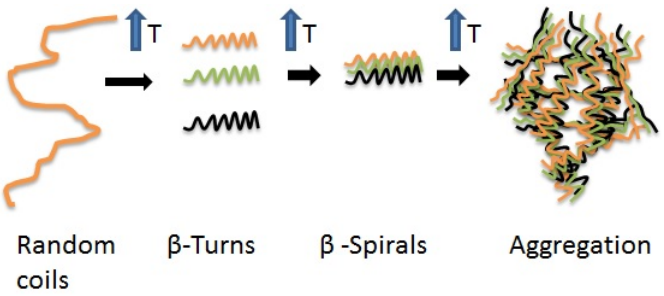

Figure 1.11. Representation of the ELP T_t mechanism as the temperature is raised.

In an attempt to influence the rate at which this transition process occurred an oligomerization domain known as foldon[191], a 27 amino acid globular domain located on the C terminus of T4 fibritin, was attached to the C terminus of ELPs of varying length. This oligomerization domain is a natural trimerizing domain, that has been shown to stabilize collagen triple helices as well as reduce their concentration dependence[192]. When attached to ELPs foldon was found to reduce the T_t of ELP constructs over a range of chain lengths, ELP concentration and solution conditions as compared to linear structures, which was the basis of my thesis work.

Further investigation of the ELP-foldon construct showed that at low salt and high pH conditions above the T_t, this system self-assembles into spherical micelles[193]. These micelles ranged in size from 25 to 30 nm in salt conditions less than 15 mM. As the salt concentration increased between 15 and 45 mM, the size of the particles increases to a diameter of 60-65 nm. Beyond a salt concentration of 45 mM the constructs aggregate and fall out of solution, the range of particle size is represented in Figure 1-11.

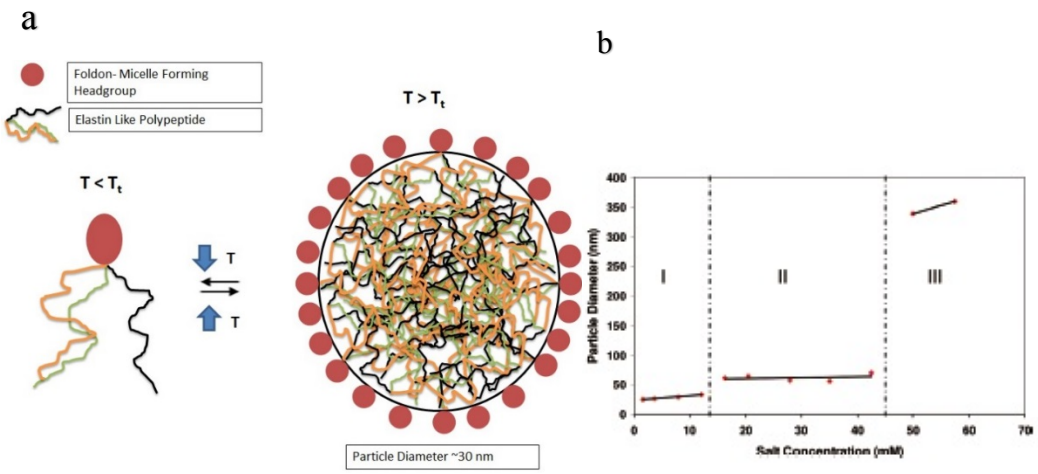

Figure 1.12. Schematic of ELP-foldon micelle formation **b)** representation of particle size as a function of salt concentration. 3 distinct regions are found.

The formation of these micelles can be described in the following ways. The foldon domain carries a net negative charge and acts as a hydrophilic head group in this system. When the T_t is passed the hydrophobic chains separate into the interior of the micelle while the foldon domain forms the corona of the micelle. The effect of salt on the micelles can be explained by the fact that as the salt increases the size of the foldon domain becomes smaller while the length of the ELP chains in the core increases. This is supported by a large increase in molecular weight as the salt increases to the second regime[194]. The pH of the solution must be kept high to allow for micelle self-assembly due to the fact that at pH above 9.6 it is above the pKa of N-terminal amines. At pH values below the pKa there is a net charge on the ELP core, which prevents micelle formation. Also below these pKa values there are end charges which prevent the arms from folding together, thus extending the chains further and disrupting particle formation. Further it was found that as the salt increased the micelles changed from a spherical shape to a cylindrical shape. These studies have shown our labs ability to create self-assembling micelles, wherein the size and shape can be controlled by changing the parameters of the environment.

1.9. Scope of the Project

The scope of this dissertation is to use elastin-like polypeptides as the basis for creating a multifunctional theranostic nanoparticle system. To create a theranostic system a step-wise approach was undertaken. The first step was to add a imaging modality to the base $(GVGVP)_{40}$-foldon nanoparticle system that we have fully designed, developed, and characterized. The protein based MRI contrast agent CA1.CD2 was chosen as the fusion

partner for a number of reasons. These include the fact that it is entirely protein based, has a similar protein structure, has defined hydrophilic character, and is amenable to alteration and resistant to change in solution. The first part of this work discusses the process of fusion of this domain to ELP-foldon using molecular biology techniques, followed by its expression and purification, as discussed in chapter II. After the successful fusion of the protein, the activity of both components was investigated and both domains retained their individual properties. This showed the fusion of these two components created a successful nanoparticle based MRI contrast agent that displayed higher relaxivity values on a per Gd^{3+} basis than clinical MRI contrast agents and displayed temperature responsive behavior, as discussed in chapter III.

The next step in creating the theranostic system was to introduce targeting ligands for site-specific localization of the contrast agent and particles, as discussed in chapter IV. Gastrin release peptide was chosen as the targeting peptide for this part of the study. Once this was incorporated the new ELP was characterized as well as its MRI activity to compare to non-targeted versions. To demonstrate the efficacy of the targeting peptide, three cancer cell lines were chosen with varying levels of receptor expression. After incubation of the targeted protein with cancer cells specific targeting and cellular localization was demonstrated using fluorescent microscopy and MRI. The final step was to demonstrate the ability to load therapeutic into the core of the nanoparticles and characterize the release properties as well as the cytotoxic effects of the constructs.

The final chapter discusses efforts made to modify the molecular architecture of the construct through substitution of different chain lengths as well modification of the guest

residues. Finally there are recommendations as to how to improve the construct for future use to overcome some of the limitations present.

This system displays and demonstrates many of the desirable feature of ELPs including 1) general biocompatibility 2) control over size shape and charge of particles 3) ability to store and release a therapeutic cargo 4) simple method to modify the system to include various functionalities 5) responsive behavior. Taken as a whole these steps represent the construction of fully protein based responsive nanoparticle for use in theranostic applications.

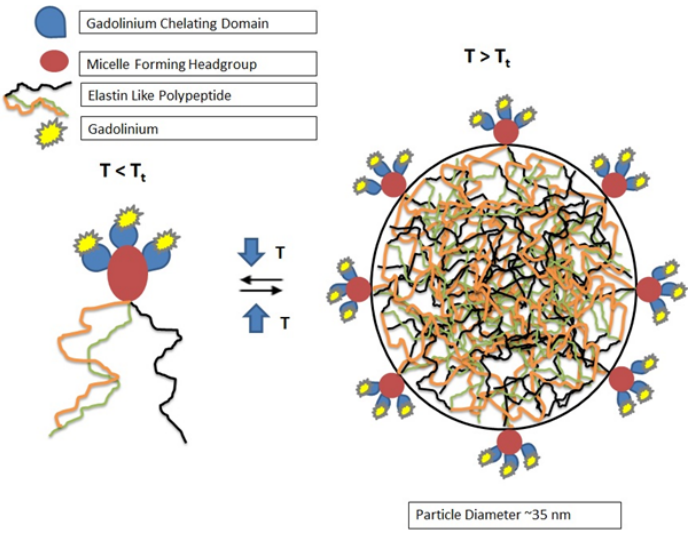

Figure: 1.13. ELP-foldon nanoparticle formation. Schematic showing how ELP-foldon-CA1.CD2 undergoes nanoparticle formation.

CHAPTER II

DESIGN, SYNTHESIS, EXPRESSION AND CHARACTERIZATION OF PROTEINS

2.1. Introduction

The scope of this work is to use elastin-like polypeptides as the basis for creating a multifunctional theranostic nanoparticle system (Figure 2.1). To create a theranostic system a step-wise approach was undertaken with the first step being the design of the system. Following this is a detailed explanation of the expression and purification methods as well as their relative levels of success. After this, an explanation of the characterization methods used to test protein purity and activity, gadolinium binding levels, and therapeutic protein interactions. Finally detailed explanations of cell culture protocols and images are presented. A summary of the constructs created and their properties can be found in Table 2.1.

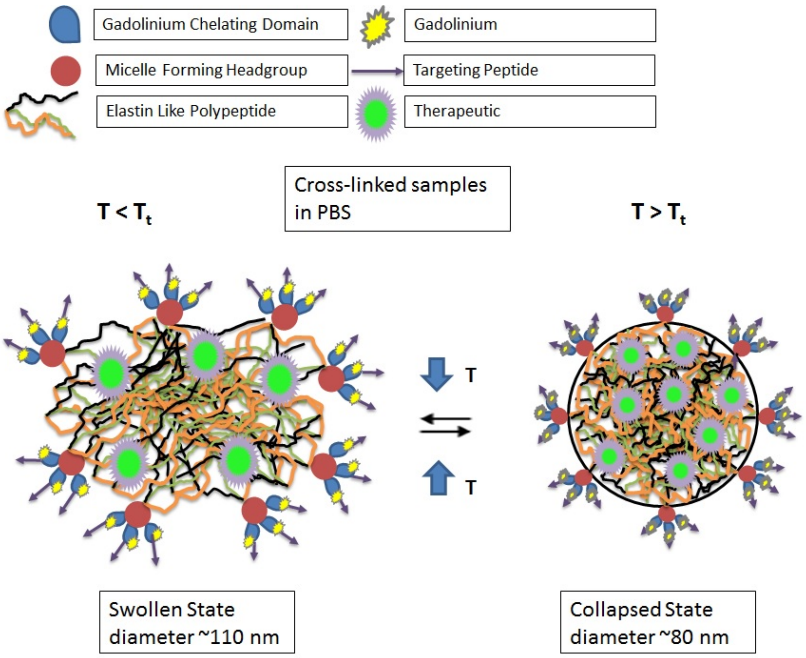

Figure 2.1. Final theranostic nanoparticle form. Schematic of final nanoparticle product produced from individual components used in this study.

Construct Name	Sequence	Molecular Weight (kDa)	T_t 25 µM PBS (°C)
ELP-IMG	MGH$(GVGVP)_{40}$-foldon-CA1.CD2	31.2	31.7
ELP-SPACER-IMG	MGH$(GVGVP)_{40}$-SPACER-foldon-CA1.CD2	33.4	31.5
E-ELP-SPACER-IMG	MGHGVGVPGEVGVP$(GVGVP)_{41}$-SPACER-foldon-CA1.CD2	34.2	30.8
10ELP-IMG	MGH$(GVGVP)_{10}$-CA1.CD2	15.9	>70
20ELP-IMG	MGH$(GVGVP)_{20}$-CA1.CD2	19.6	52.5
40ELP-IMG	MGH$(GVGVP)_{40}$-CA1.CD2	28.3	40.5
40c20ELP-IMG	MGHGVGVP_{41}GCGVP$(GVGVP)_{21}$-CA1.CD2	36.4	28.3
ELP-NS-THO	MGH$(GVGVP)_{40}$-foldon-CA1.CD2-GRP	32.4	31.4
ELP-THO	MGH$(GVGVP)_{40}$-foldon-CA1.CD2-SPACER-GRP	35.3	30.7

Table 2.1. Summary of the constructs created in this study. Presented are their respective molecular weights and transition temperatures (T_t).

2.2. Use of molecular biology to design new protein constructs

The design and synthesis of protein based polymers and other protein constructs requires the use of various molecular biology techniques. Through years of research I have acquired extensive experience making ELP genes of varying length, composition, and with various fusion proteins present utilizing these techniques. What follows is a brief explanation of some of the underlying principles used in the synthesis of the constructs used in this study.

The basic process of DNA cloning is the primary mechanism used to synthesize the constructs used in this study, wherein a large number of identical DNA molecules are

prepared. The key to utilizing this process is to have the DNA fragment in a vector that can replicate within a host cell. This recombinant DNA, which consists of the vector plus inserted DNA fragment, is placed in the host cell (*E.coli*.) it can replicate and generate a large number of copies.

In order to isolate specific sequences of DNA that constitute specific genes, the sequence must be able to be cleaved at distinct locations in its genome. This is achieved with the process of restriction enzyme digestion, which allows DNA molecules to be cut into small fragments. Restriction enzymes recognize specific sequences of base pairs that are typically 4 to 8 base pairs in length and called restriction sites. Upon recognition the enzymes will cleave both strands of DNA at this site and can leave staggered cuts (Figure 2.2). These cuts generate single stranded fragments at both tails, which are complimentary to those on fragments generated by the same restriction enzyme. These single stranded regions are called sticky ends and will base pair with those on the other DNA fragments with the same restriction enzyme site. These cut DNA fragments can then be inserted into vector DNA with the aid of enzyme ligases that covalently link the cut DNA fragment into a vector DNA with complimentary sticky ends. The process of linkage comes via a 3' to 5' phospho-diester bond between the 3' hydroxyl end of one restriction enzyme fragment and the 5' phosphate end of the other fragment. When DNA ligase supplemented with ATP is added to a reaction containing restriction enzyme digested fragments with compatible sticky ends, the pieces are covalently ligated together.

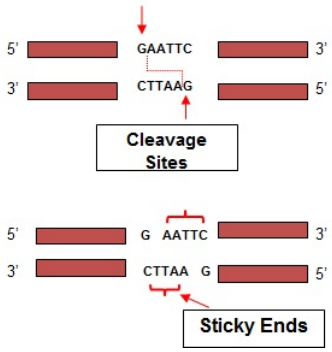

Figure 2.2. Restriction enzyme digestion producing sticky ends.

Now the fragment of interest is located within bacterial plasmid DNA. These plasmids are used as cloning vectors and are closed circular molecules of double stranded DNA that range in size from 1-200 kb and are capable of autonomous replication in a cell[195]. The most commonly used plasmids in recombinant DNA techniques are able to replicate in *Escherichia coli* (*E. coli*). One such vector is the one used in this study, pET20b, a common expression vector that contains the following sections: a replication origin, a drug resistant gene and a region where DNA fragments can be inserted (Figure 2.3).

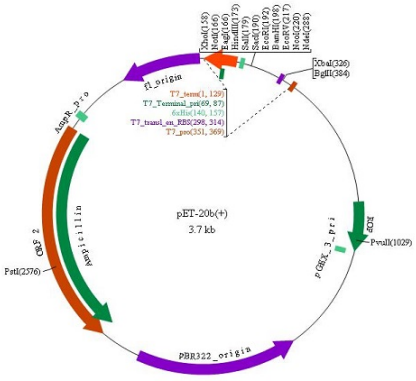

Figure 2.3. pET20b vector map. Highlighted replication region, insertion region and antibiotic resistant region.

The replication origin is a specific DNA sequence of 50-100 base pairs present in plasmids which replication of the DNA to be inserted is initiated. Once the DNA replication is initiated it continues around the circular plasmid regardless of the DNA sequence and thus any DNA inserted is replicated along with the plasmid DNA. The antibiotic resistant region in the plasmid encodes the enzyme β-lactamase, which gives antibiotic resistance, in this case ampicillin, to bacteria carrying them. The presences of these antibiotic resistant genes on plasmids allow isolation of bacteria containing the plasmid from those that do not by growing them on agar plates containing ampicillin where they survive and form colonies.

The process of transformation allows foreign DNA to be inserted into a cell. When *E.coli* cells are mixed with recombinant DNA a small fraction of the cells will take up the plasmid DNA. In order to facilitate this process the cells must be made competent through the use of "competent cells" containing Calcium chloride ($CaCl_2$). The $CaCl_2$ ions neutralize the repulsion between the cell membranes and the DNA. After heat shocking the competent cells a thermal gradient is created that allows the DNA to enter the cells. Placing the transformed mixture of cells on agar plates containing ampicillin, only cells containing the drug resistant gene in the plasmid will survive while those that do not take up the plasmid will die. Thus DNA fragments to be cloned can be inserted into plasmid vectors containing an ampicillin resistant gene. When this mixture of plasmid, *E.coli* and competent cells undergoes the transformation process the resulting cells contain the same inserted sequence of DNA but multiplied into many copies (Figure 2.4).

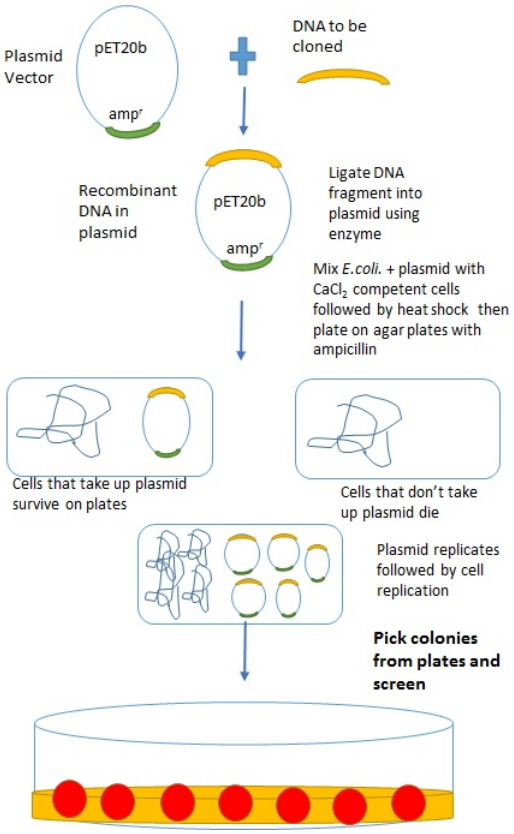

Figure 2.4. DNA cloning process.

2.3. Synthesis of ELP CA1.CD2 fusion protein

The base structure for these studies is $(GVGVP)_{40}$-foldon (Figure 2.5) and the gene encoding the ELP-foldon structure was synthesized as reported[193]. The amino acid structure for the foldon domain is GYIPEAPRDGQAYVRKDGEWVLLSTFL[191] and is 3 kDa in weight.

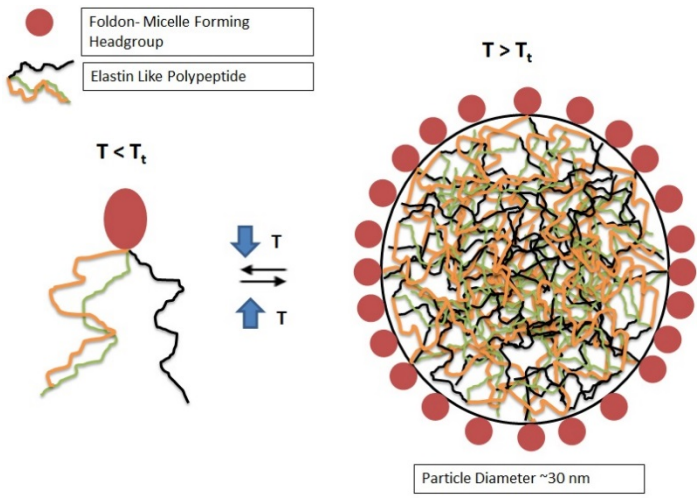

Figure 2.5. GVGVP$_{40}$-Foldon Micelle. Representation of three-armed star micelle formed by GVGVP$_{40}$-foldon.

To complete this work this all structures had to have an imaging domain fused to the ELP-foldon, which in this case is the 99 amino acid CA1.CD2 protein based MRI contrast agent[136]. This protein domain is encoded by the following amino acid sequence:

RDSGTVWGALGHGIELNIPNFQMTDDIDEVRWERGSTLVAEFKRKMKPFLKSGAFEIDANG DLDIKNLTRDDSGTYNVTVYSTNGTRILDKALDLRILE

A schematic representation of the design of the design of ELP-foldon + imaging domain structure is presented in Figure 2.6.

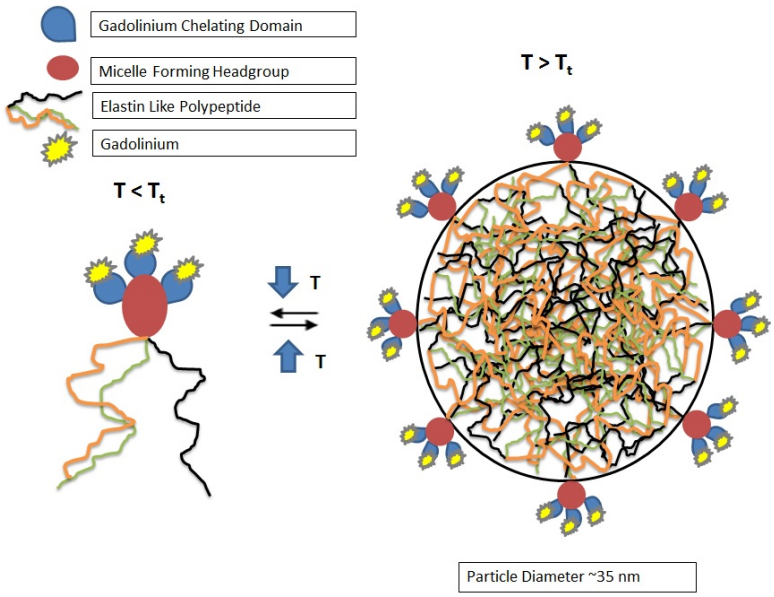

Figure 2.6. GVGVP$_{40}$-foldon CA1.CD2 micelle. Representation of three-armed star micelle formed by the fusion of GVGVP$_{40}$-foldon and the CA1.CD2 protein domain.

To utilize this domain with the base structure of ELP-foldon and to use the molecular biology techniques compatible with my previous work there were three main requirements:

1) Encode as a single domain that would be able to be ligated into a GVGVP$_{40}$-foldon vector
2) Contain recognition sites for NdeI, PflmI and BglI restriction enzymes with correct sticky ends
3) Contain no internal recognition sites for these restriction enzymes ensuring no digestion takes place internally

The first step was to create a series of overlapping oligonucleotides[196](Figure 2.7), which would encode the 99 amino acid CA1.CD2 domain and provide the necessary enzyme digestion sites to fulfill the requirements.

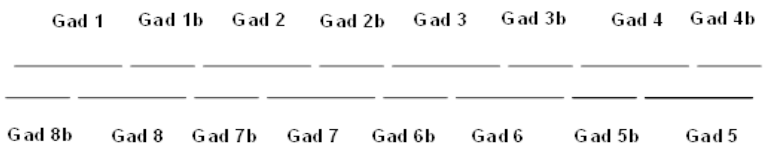

Figure 2.7. Alignment of designed oligonucleotides. Representation of the alignment of the oligonucleotides used to encode the CA1.CD2 gene

DNA Sequence	Oligo Name
CGTGACTCTGGTACCGTTTGGGGTGCGCTGGGTCACGGTATCGAACTGAACAT	**Gad1**
CCCGAACTTCCAGATGACCG	**Gad1b**
ACGACATCGACGAAGTTCGTTGGGAACGTGGTTCTACTCTGGTTGCGGAATTT	**Gad2**
AAACGTAAAATGAAACCGTT	**Gad2b**
CCTGAAATCTGGTGCGTTCGAAATCGACGCGAACGGTGACCTGGACATCAAAAACC	**Gad3**
TGACCCGTGACGACTCTGGT	**Gad3b**
ACCTACAACGTTACCGTTTACTCTACCAACGGTACCCGTATCCTGGACAAAGCGCT	**Gad4**
GGACCTGCGTATCCTGGAA	**Gad4b**
TTCCAGGATACGCAGGTCCAGCGCTTTGTCCAGGATA	**Gad5**
CGGGTACCGTTGGTAGAGTA	**Gad5b**
AACGGTAACGTTGTAGGTACCAGAGTCGTCACGGGTCAGGTTTTTGATGTCCAGGT	**Gad6**
CACCGTTCGCGTCGATTTCG	**Gad6b**
AACGCACCAGATTTCAGGAACGGTTTCATTTTACGTTTAAATTCCGCAACCAGAGT	**Gad7**
AGAACCACGTTCCCAAC	**Gad7b**
GAACTTCGTCGATGTCGTCGGTCATCTGGAAGTTCGGGATGTTCAGTTCGATACCG	**Gad8**
TGACCCAGCGCACCCCAAACGGTACCAGAGTCACG	**Gad8b**
AATTTACATATGGGCCACGGCGTGGGTCGTGACTCTGGTACCGTTTGG	**GadN Primer**
ATTTATGGCCGGCCCGGCCTCATTATTCCAGGATACGCAGGTCCAG	**GadC Primer**

Table 2.2. Oligonucleotides used to encode the CA1.CD2 gene.

When the oligonucleotides are assembled and the sequence checked, they encode the correct amino acid sequence. Further inserting the sequence into the New England BioLabs "cutter tool" allows for the visualization and location of the restriction enzyme sites that are present. Assembly of these oligonucleotides to prepare them for insertion into a compatible pET20b vector required five steps. The first step in the process is to mix each of the 16 oligonucleotides, excluding the N-terminal and C-terminal primers, together in equi-molar ratios of 10 pmol. This was followed by phosphorylation with T4 poly-nucleotide kinase (New England Biolabs). T4 PNK is used to catalyze the transfer and exchange of the phosphate from ATP to the free hydroxyl end of the 5' RNA. To utilized T4 PNK combine 160 pmol of DNA (approximately 25µl) with 5µl 10x reaction buffer, 5µl 1x T4 DNA ligase, 1µl T4 PNK and 14 µl nuclease free water. This mixture was incubated at 37°C for 30 in a water bath. Following this the reaction was heat inactivated at 65 °C for 20 minutes. Thermo-annealing then took place using a thermo-cycler (Thermo-Scientific PCRSprint). The annealing procedure was a process of heating to 95 °C. This annealed product was then run on agarose gel, extracted, and purified using a gel extraction kit (Qiagen). This product was annealed together after this using *E.coli* DNA ligase (New England BioLabs), which is used to catalyze the formation of phospho-diester bonds between 5' phosphate and 3' hydroxyl termini in DNA with cohesive ends. The *E. coli* DNA ligase reaction was composed of 21 µl of DNA from step 3, 21 µl of *E. coli* ligase buffer and 2 µl *E. coli* ligase. The mixture was held at 16 °C for 30 minutes, followed by heat inactivation by incubating at 65 °C for 20 minutes. Finally, the resulting annealed DNA is used as the template DNA in a 100 µl PCR reaction involving the N-terminal and C-terminal primers shown in Table 1. The reaction

was composed of 5 µl of the ligated product from previous step, 5 µl forward primer (Gad N primer), 5 µl reverse primer (Gad C primer), 50 µl of PCR master mix and 35 µl nuclease free water. PCR reaction took place and the end product was the final gene.

At this point the CA1.CD2 gene was fully constructed and compatible with our labs molecular biology methods. This DNA was digested with the two restriction enzymes NdeI and BglI to allow it to be inserted into a pET20b vector (Novagen), which contained complimentary sticky ends from an enzyme digestion with NdeI and SfiI restriction enzymes. The procedures for these reactions are as follows. In a 40 µl reaction I combined 15 µl of DNA template, 4 µl of buffer 4, .4 µl of BSA, 2 µl of NdeI, 2 µl of SfiI and 16.6 µl of nuclease free water. The reaction was then incubated for 3 hours at 37°C and followed by agarose gel running and purification. For a NdeI and BglI restriction enzyme digestion, I combined 15 µl of DNA template, 4 µl of buffer 3, 2 µl of NdeI, 2 µl of BglI and 17 µl of nuclease free water, which was then incubated for 3 hours at 37°C and followedd with agarose gel running and purification. Finally, a NdeI and PflmI restriction enzyme digestion combines 15 µl of DNA template with 4 µl of buffer 2, .4 µl of BSA, 2 µl of NdeI, 2 µl of PflMI and 16.6 µl of nuclease free water. The reaction was incubated for 3 hours at 37°C and proceed with agarose gel running, extraction and purification.

After gel purification, the insert and vector were ligated together using a quick ligation kit (New England BioLabs), which enables the ligation of cohesive or blunt ends of DNA fragments. The protocol for a quick ligation reaction is to combine 1µl (amounts can vary) of vector (pET20b DD with NdeI and SfiI), 4-9 µl of insert (CA1.CD2 PCR product from step 5) with nuclease free water up to 10 µl, 10 µl quick ligase buffer and 1

µl of quick ligase in a centrifuge tube. These components were combined, given a pulse in a micro centrifuge and allowed to sit at room temperature for 5 minutes, then chilled on ice before transforming.

To transform the plasmid the following protocol was utilized. First competent cells are removed from the -80°C freezer and thawed on ice. Next, 10 µl of the reaction mixture was chilled in a 1.5 ml microcentrifuge tube. A volume of 50 µl of competent cells is added to the DNA and mixed by gentle pipetting up and down. This mixture is placed on ice for 30 minutes, followed by a heat shock at 42 °C for 30 seconds. LB media without ampicillin is then added in a volume of 950 µl. This mixture is then held at 37°C for one hour. After one hour, 300 µl is spread onto pre-warmed agar plates and incubated overnight. Resulting colonies are picked and grown overnight in LB media with ampicillin at 37°C and 300 RPM shaking. Overnight cultures were mini-prepped according to standard protocols and were screened using PCR techniques, with T7 forward and T7 reverse as the forward and reverse primers for a pET20b vector. To perform a PCR 1 µl of template DNA, extracted from colonies on agarose plates, 2.5 µl forward primer, 2.5 µl reverse primer, 12.5 µl PCR master mix and 6.5 µl of nuclease free water are combined and placed in the thermo-cycler where a standard PCR protocol is applied.

The resulting gene contained 105 amino acids (green highlight CA1.CD2, blue highlight ELP overhang) and the sequence was verified by DNA sequencing (Cleveland Clinic Genomics Core), and is:

MGHGVGRDSGTVWGALGHGIELNIPNFQMTDDIDEVRWERGSTLVAEFKRKMK
PFLKSGAFEIDANGDLDIKNLTRDDSGTYNVTVYSTNGTRILDKALDLRILE

After checking the sequence on the NEB cutter tool the correct restriction enzyme digestion sites were present.

The results of this confirmed that the pET20b-CA1.CD2 construct was now ready to be modified in many ways, including through the addition of the GVGVP$_{40}$-foldon structure from Figure 2.5. To achieve the construct described in Figure 2.6, the pET20b-CA1.CD2 construct was double digested with NdeI and PflMI restriction enzymes to create a vector (3), while the GVGVP$_{40}$-foldon construct was double digested with NdeI and BglI (4). Ligation and transformation of 3 and 4 yielded the final construct for ELP-IMG (Figure 2.8).

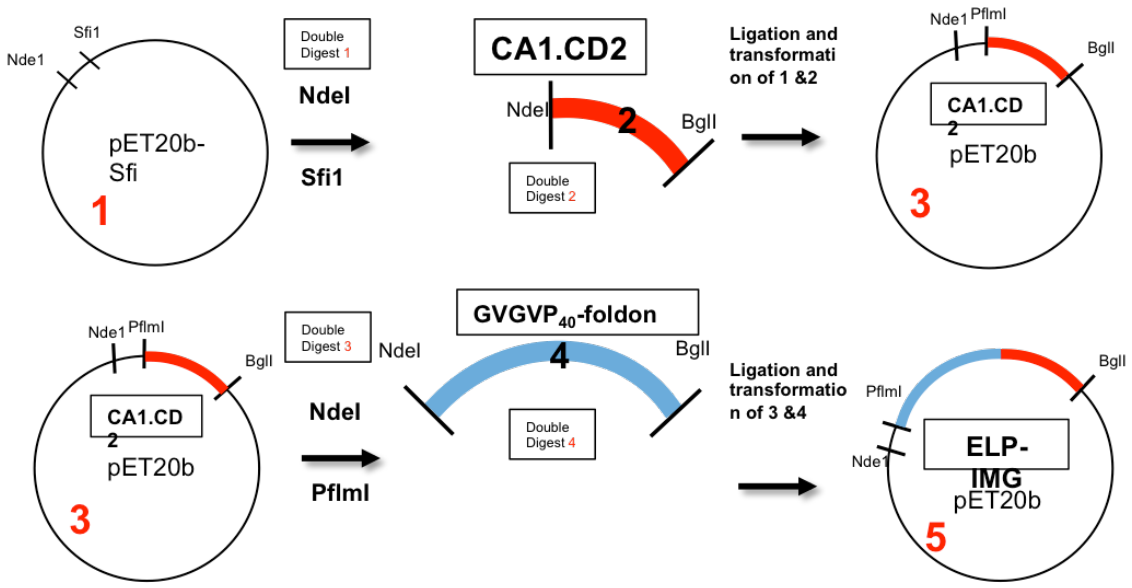

Figure 2.8. Design of ELP-IMG fusion protein. Schematic detailing the construction of the ELP-CA1.CD2 fusion protein. The step-by-step nature of the construction is clear, and the final construct retains the necessary cut-sites to use the system in a modular fashion.

This final construct, which is the base structure for this work, contains GVGVP$_{40}$foldon-CA1.CD2 (ELP-IMG), and the sequence was verified using DNA sequencing and the final construct contained the following:

MGHGVGVPGVGVPGVGVPGVGVPGVGVPGVGVPGVGVPGVGVPGVGVPGVGVPGVG
VPGVGVPGVGVPGVGVPGVGVPGVGVPGVGVPGVGVPGVGVPGVGVPGVGVPGVGVP
GVGVPGVGVPGVGVPGVGVPGVGVPGVGVPGVGVPGVGVPGVGVPGVGVPGVGVPGV
GVPGVGVPGVGVPGVGVPGVGVPGVGVPGVGVPGVGVPGVGVPGVGVPGYIPE
APRDGQAYVRKDGEWVLLSTFLGPGVGRDSGTVWGALGHGIELNIPNFQMTDDI
DEVRWERGSTLVAEFKRKMKPFLKSGAFEIDANGDLDIKNLTRDDSGTYNVTVY
STNGTRILDKALDLRILE

Blue regions represent ELP, green represents the foldon domain, and the yellow represents the CA1.CD2 domain.

2.4. Synthesis of ELP-CA1.CD2 fusion protein variations

One of the main objectives of this work was to create a flexible system that would be able to undergo modification in a simple manner utilizing only molecular biology. After the successful synthesis of ELP-IMG, variations were synthesized to determine the effects. The first variation was to create a spacing element between the foldon headgroups and the CA1.CD2 domain. Also, it has been theorized that in ELP-fusion proteins, a peptide spacer element may help retain the functional activity of the targeting protein[197]. The design of the spacing element was chosen so that it would be expected to have little effect on ELP properties due to neutral charge and balance of hydrophobic / hydrophilic amino acids. It is represented by the sequence:

WTSTGPQSSNTGNPSTSGQNNVPGVG

This sequence was inserted into a pET20b (previous work) vector and can be double digested digested with NdeI and BglI to allow it be inserted into another compatible vector. After digesting the pET20b-CA1.CD2 vector with NdeI and PflmI restriction enzymes, the two components were compatible and after ligation, transformation, and screening the new construct was sequenced as follows with the red highlights being the spacer element, and the yellow highlights being the CA1.CD2 domain.

MGHGVG**WTSTGPQSSNTGNPSTSGQNNVPGVG**RDSGTVWGALGHGIELNIPN
FQMTDDIDEVRWERGSTLVAEFKRKMKPFLKSGAFEIDANGDLDIKNLTRDDSG
TYNVTVYSTNGTRILDKALDLRILE

This construct was then digested with NdeI and PflMI to allow a $GVGVP_{40}$-foldon insert double digested with NdeI and BglI to be ligated into it. After completion DNA sequencing confirmed the construct, which we call **ELP-SPACER-IMG:** Blue highlights are ELP portions, green highlights are the foldon domain, red is the spacer element, and yellow is the CA1.CD2 domain.

MGHGVGVPGVGVPGVGVPGVGVPGVGVPGVGVPGVGVPGVGVPGVGVPGVG
VPGVGVPGVGVPGVGVPGVGVPGVGVPGVGVPGVGVPGVGVPGVGVPGVGVP
GVGVPGVGVPGVGVPGVGVPGVGVPGVGVPGVGVPGVGVPGVGVPGVGVPGV
GVPGVGVPGVGVPGVGVPGVGVPGVGVPGVGVPGVGVPGVGVPGVGVPGYIPE
APRDGQAYVRKDGEWVLLSTFL**WTSTGPQSSNTGNPSTSGQNNVPGVG**RDSG

TVWGALGHGIELNIPNFQMTDDIDEVRWERGSTLVAEFKRKMKPFLKSGAFEID
ANGDLDIKNLTRDDSGTYNVTVYSTNGTRILDKALDLRILE

The next variation that was created was to add a glutamic acid to the N-terminus in order to eliminate the pH dependence of the micelle formation. A construct was created separately with the sequence: MGHGVGVPGEGVP (VEV), inserted into a pET20b vector. This was accomplished in the same manner as described earlier with the ELP-SPACER-IMG construct being digested with NdeI and pflMI and the VEV digested with NdeI and BglI. The same process as described earlier was applied for ligation, transformation and screening and after DNA sequencing this construct was obtained. This construct is known as **E-ELP-SPACER-IMG** and the grey region is the glutamic acid containing portion, blue highlight regions represent ELP, green is the foldon domain, red is the spacer and yellow is the CA1.CD2 domain.

MGHGVGVPGEGVPGVGVPGVGVPGVGVPGVGVPGVGVPGVGVPGVGVPGVG
VPGVGVPGVGVPGVGVPGVGVPGVGVPGVGVPGVGVPGVGVPGVGVPGVGVP
GVGVPGVGVPGVGVPGVGVPGVGVPGVGVPGVGVPGVGVPGVGVPGVGVPGV
GVPGVGVPGVGVPGVGVPGVGVPGVGVPGVGVPGVGVPGVGVPGVGVPGVGV
PGVGVPGVGVPGYIPEAPRDGQAYVRKDGEWVLLSTFL**WTSTGPQSSNTGNPS**
TSGQNNVPGVGRDSGTVWGALGHGIELNIPNFQMTDDIDEVRWERGSTLVAEF
KRKMKPFLKSGAFEIDANGDLDIKNLTRDDSGTYNVTVYSTNGTRILDKALDLRI
LE

Constructs were also made that did not contain the foldon domain, in order to compare the behavior of the CA1.CD2 attached to monomeric ELP to the behavior of the

CA1.CD2 domain to the trimeric ELP. The process was the same as described previously however, instead of a $GVGP_{40}$-foldon used as the insert varying lengths of GVGVP were inserted into the vector. Lengths chosen were based on number repeats of GVGVP and were 10, 20 and 40 repeats, as well as a construct of the form 41-C-21GVGVP.

2-5. Construction of ELP-THO targeted construct

The genes that encode the ELP-THO structure ($GVGVP_{40}$-foldon-CA1.CD2-Spacer-GRP) were synthesized as discussed in previous sections. The C terminal fragment of the gastrin release peptide is represented by the amino acid sequence: GNHWAVGHLM. To modify the structure of ELP-IMG to allow for addition of gastrin release peptide a new set of oligonucleotides were created as well as a new primer (Table 2-3). There were two variations, one that included a flexible spacer between the head-groups and targeting element and one that did not. Also, the CA1.CD2 domain needed to be modified to remove the stop codon that was present in it, in order to add these elements after the CA1.CD2 to make a new C terminus.

DNA Sequence	Primer Name
TATGGGCCACGGCGTGGGTGGGAATCACTGGGCAGTGGGACACTTGATGTGAGCCCGGTGGGC	GRP Forward
CACCGGGCTCACATCAAGTGTCCCACTGCCCAGTGATTCCCACCCACGCCGTGGCCCA	GRP Reverse
TATGGGCCACGGCGTGGGTTGGACCTCTACTGGCCCGCAATCCTCTAACACTGGCAATCCGTCTACCTCTGGTCAAAATAACGTGCCGGGC	Spacer Forward
CGGCACGTTATTTTGACCAGAGGTAGACGGATTGCCAGTGTTAGAGGATTGCGGGCCAGTAGAGGTCCAACCCACGCCGTGGCCCA	Spacer Reverse
CGTATCCTGGAAGAGCCCGGCTGGCCATTTTTT	Gad No stop Forward
AAAAAATGGCCAGCCGGGCTCTTCCAGGATACG	Gad No stop Reverse

Table 2.3. Oligonucleotides used to encode GRP and spacer element.

Upon receipt of the GRP forward and reverse oligonucleotides they were annealed in the thermo cycler as described previously. The annealed GRP primers were inserted into a pET20b vector that had been double digested with NdeI and PflMI. These constructs were ligated together and transformed to give a new vector pET20b-GRP, which had the amino acid sequence: MGHGVGGNHWAVGHLM. The second variation of the construct that was created included the spacer element before the gastrin release peptide fragment. To achieve this the pET20-GRP vector was modified through the addition of the spacer element. The pET20b-GRP vector was double digested with NdeI

and PflMI, run on agarose gel and purified and the annealed spacer was ligated into this vector. The resulting construct had the amino acid sequence MGHGVG**WTSTGPQSSNTGNPSTSGQNNVPGVG**GNHWAVGHLM. This sequence contains ELP overhangs as highlighted in yellow, spacer element highlighted in red and the gastrin release peptide fragment highlighted in pink. These constructs both contain the appropriate restriction enzyme digestion sites for further modification with ELP's and also contain stop codons.

In order to incorporate the CA1.CD2 domain into these vectors a set of primers were created that would remove the stop codon from the domain, so the expression would end at the GRP fragment and not after the CA1.CD2 domain. The primers were annealed together using the thermo cycler, then used in a PCR reaction with T7 forward primer and run on an agarose gel followed by extraction and purification. The purified product was double digested with NdeI and BglI, run on agarose gel, and purified. This was used as the insert in a ligation with both of the vectors described above that had been digested with NdeI and PflMI (Figure 2.9).

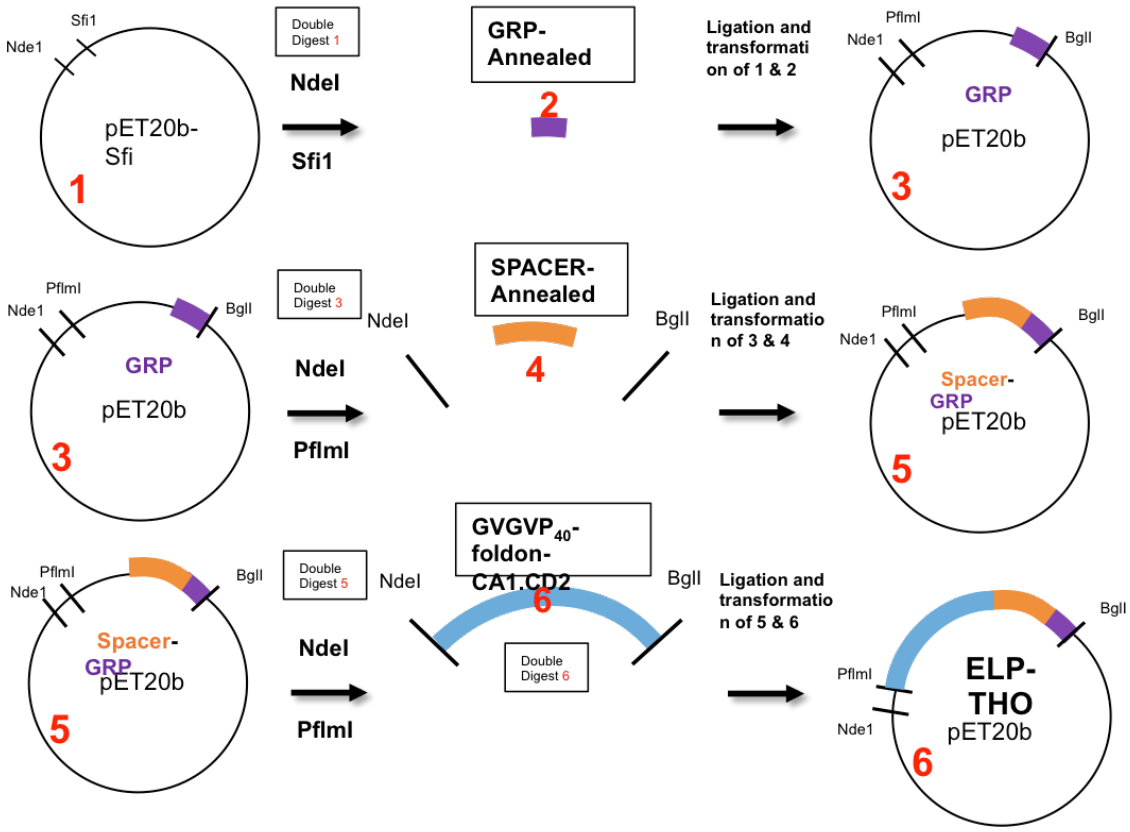

Figure 2.9. Design of ELP-THO protein. Schematic detailing the construction of the ELP-THO targeted protein. The step-by-step nature of the construction is clear, and the final construct retains the necessary cut-sites to use the system in a modular fashion.

After PCR screening the DNA sequences were confirmed (Cleveland Clinic Genomics Core) and resulted in the following amino acid sequence:

GVGVP40-foldon-CA1.CD2-GRP (ELP-NS-THO):

MGH$(GVGVP)_{40}$GYIPEAPRDGQAYVRKDGEWVLLSTFLGPGVGRDSGTVWGAL
GHGIELNIPNFQMTDDIDEVRWERGSTLVAEFKRKMKPFLKSGAFEIDANGDLDI
KNLTRDDSGTYNVTVYSTNGTRILDKALDLRILEGNHWAVGHLM

GVGVP40-foldon-CA1.CD2-Spacer-GRP (ELP-THO):

MGH$(GVGVP)_{40}$GYIPEAPRDGQAYVRKDGEWVLLSTFLGPGVGRDSGTVWGAL

GHGIELNIPNFQMTDDIDEVRWERGSTLVAEFKRKMKPFLKSGAFEIDANGDLDI

KNLTRDDSGTYNVTVYSTNGTRILDKALDLRILE

GPGVGWTSTGPQSSNTGNPSTSGQNNVPGNHWAVGHLM

2.6. Expression and Purification of ELPs

Typically elastin-like polypeptides (ELPs) are purified using a process known as inverse transition cycling (ITC)[198], which takes advantage of the inverse transition temperature (T_t) displayed by the proteins. ELP's are highly soluble below their T_t, but will aggregate and come out of solution rapidly when the temperature is raised above T_t due to hydrophobic collapse and aggregation. This creates a separate ELP-rich phase. This entire process is reversible and the ELP-rich phase can be solubilized when the temperature is dropped below the T_t. Regardlesss of composition the T_t of ELPs is dependent upon the concentration of protein, in an inverse-log fashion[199].

The stimuli that drive the T_t of the solution, as mentioned previously, can be easily tuned to a desired temperature through many different methods. Two most common ways include changing the nature of the guest residue[200] and changing the length of ELP chains through addition of pentapeptide repeats[199]. When different guest residues are introduced the balance of hydrophobic and hydrophilic components is altered. Hydrophobic guest residues have the effect of lowering the T_t and polar or charged residues raise the T_t. Longer ELP chains will have a lower T_t regardless of composition. The effect of salt on ELP T_t has been investigated thoroughly over the years. The type and concentration of salts are known to follow the Hofmeister series[165]

such that kosmotropes or Cl- and higher salts of the series will lower the T_t as well as an increase in the salt concentration will have a salting out effect. Salts that are lower on the series or chaotropes will have a salting in effect. NaCl is used extensively in ELP purification to drive the T_t and ease the purification process. Buffers used to re-suspend the ELP solution can vary depending upon the application and any specific characteristics of the fusion protein that are required. Proteins that are more hydrophobic tend to re-suspend better in pure water, while PBS is widely used to investigate suitability *in vivo*.

When a fusion protein is attached to an ELP construct, the ability to control the purification of the ELP through either gene design or addition of additives generally makes the purification of the target protein a simple process[162]. The thermal properties of the ELP are retained after the fusion[201], although there can be a difference between the T_t of the pure ELP and the T_t of the ELP-fusion protein. The fact that ELP can be genetically appended to its protein or peptide partner with precise control over the gene design of ELP fusion, such as the position of the fusion and that the thermal properties of the ELP tag can be easily tuned are considerations for the desirable use of ELPs for recombinant protein purification. If the ELP is used as a vehicle to purify protein targets that are otherwise difficult or require special methods, a protease site can be engineered between the target protein and the ELP gene. Some examples of successful ELP fusion proteins include ELP-Thioredoxin[202] purification, which was investigated as a function of ELP chain length. ELP was used to purify β-galactosidase, which is highly acidic and hydrophilic[203]. ELP-intein systems were used also to purify target proteins in conjunction with investigation of Hofmeister series to purify GFP and β-lactamase[204].

Expression of proteins is carried out in growth media, either Luria-Bertani (LB) or terrific broth (TB) supplemented with ampicillin. Various additives have been investigated to enhance the expression levels of ELP due to depletion, and there are many options to create hyper-expressions[205]. Starter cultures are prepared by either picking a fresh colony from an agar plate or taking a piece from glycerol frozen stocks in anywhere between 10-50 ml of volume and growing overnight at 37°C and 300 RPM shaking. After overnight growth, starter cultures were centrifuged at 3000 RCF (Dynac) to separate the soluble and insoluble part of the protein. The pellet was then re-suspended in fresh expression media from the flask for expression, and transferred to a 2 liter flask. Growth then took place until the optical density at 600 nm (OD_{600}) of the solution was between 0.-9-1 as measured on a UV-vis spectrophotometer (Thermo-Scientific Biomate 3). When this level was reached the protein was induced using 1 mM Isopropyl β-D-1-thiogalactopyranoside (IPTG), which is used to trigger the transcription of the lac operon, which induces expression of genes that are under control of the lac operon. After induction, the protein grew for another 5 to 5.5 hours. At the end of the growth period the media was centrifuged at 9000xg and 4°C, the supernatant was discarded and the pellets frozen for purification at a later time (Figure 2.10).

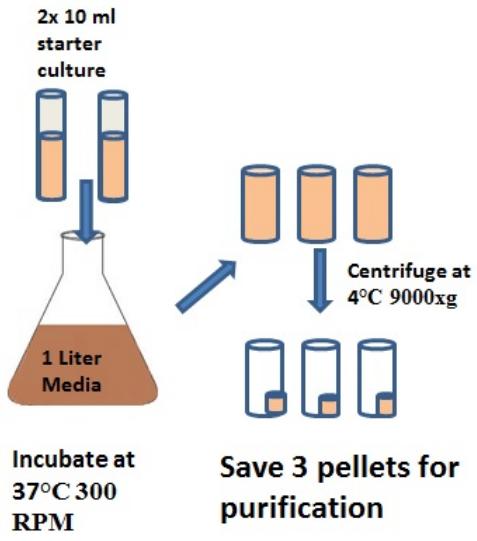

Figure 2.10. ELP expression process.

To determine which expression media and amount of starter culture required, as well as to ensure that ELP-IMG did not have significant deviation from the typical expression rates of GVGVP constructs used in our lab, growth curves were constructed by monitoring OD_{600} at regular time intervals. The results are shown in Figure 2.11 and show the expression growth rate does not deviate from other constructs grown in the lab. It was also shown that the fastest growth rate was achieved using TB media and a 50 ml starter culture, which was then used as the standard for expression of ELP-IMG.

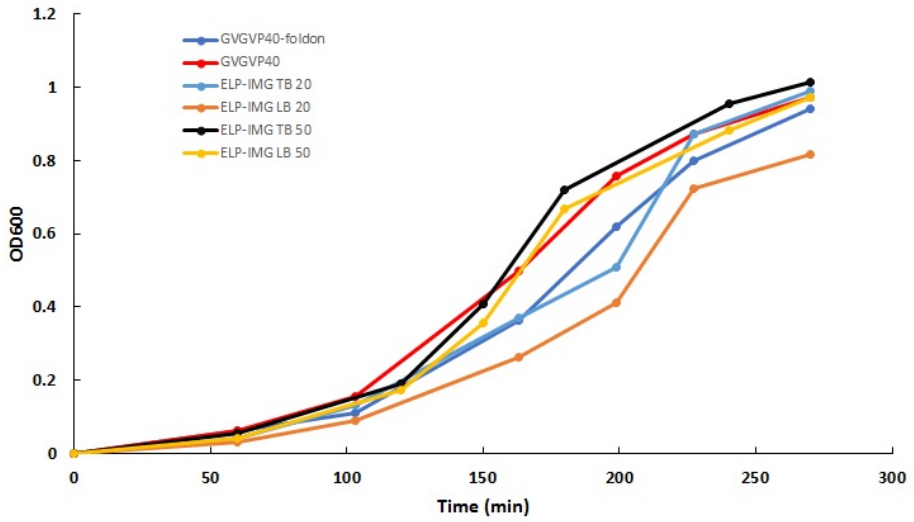

Fig 2.11. Growth rate curves for ELP-IMG. Growth rates of ELP-IMG in different media and varying volumes of starter culture compared to ELP-foldon.

Purification of ELP's using the ITC process, typically proceeds as follows. The cells contained in the frozen pellet are re-suspended in 10 ml of PBS per tube and combined into one. Sonication then took place with the tube an ice cold water bath and stored on ice for 1 hour after this to ensure complete cooling of the mixture. The protein is then centrifuged at 27,000xg at 4°C for 20 minutes to separate the soluble and insoluble fractions. The supernatant from this spin is kept due to the protein residing in the soluble fraction. The soluble portion is then heated above T_t in a centrifuge tube for at least 4 hours to allow the protein to aggregate out of solution. The aggregated proteins were centrifuged at 27,000xg at 40°C for 20 minutes. At the end of the centrifugation, the soluble and insoluble portions need to be separated immediately, with the protein now residing in the insoluble pellet. The process of hot and cold spins gets repeated 2.5 times total per purification and after the final cold spin, the purified protein resides in the soluble fraction (Figure 2.12).

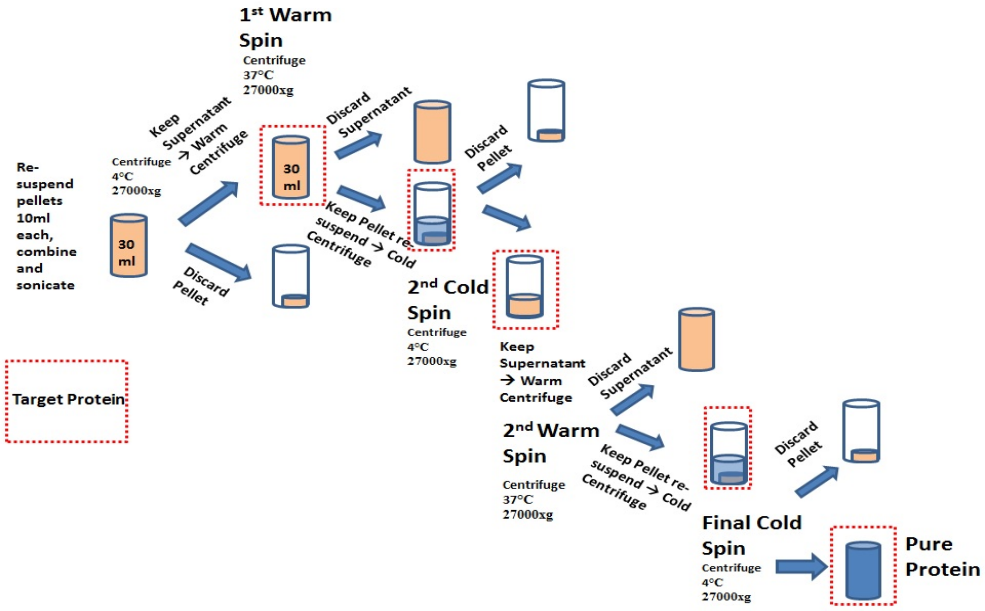

Figure 2.12. ELP purification process. Process of purifying ELP proteins to reach the desired pure target protein at the end.

2.6.1. Determination of soluble vs. insoluble content of ELP-IMG and ELP-THO

Purifed elastin-like polypeptides typically reside in the soluble fraction and can be purified using only inverse transition cycling (ITC). However, occasionally the insoluble nature fusion protein drives the polypeptide into the insoluble fraction limiting purification through simple ITC. The purification of the CA1.CD2 protein domain[206] was carried out using Glutathione Sepharose 4B beads[207], on a size exclusion column, which indicated that the protein was insoluble.

To determine the soluble or insoluble nature of the ELP-IMG / ELP-THO protein Bacterial Protein Extraction Reagent II was utilized (BPER II Pierce). BPER was designed to facilitate the extraction of soluble proteins from bacterial cells without the need for harsh chemicals, while being in a mild buffer of 20 mM Tris-HCL at pH 7.5.

Starting at the expression of the protein, every hour pre and post induction a 1ml sample was taken from the expression flask and centrifuged at 14,000xg on a micro-centrifuge (Eppendorf 5415C). The supernatant was removed and the pellet was frozen and stored for analysis (Figure 2.13).

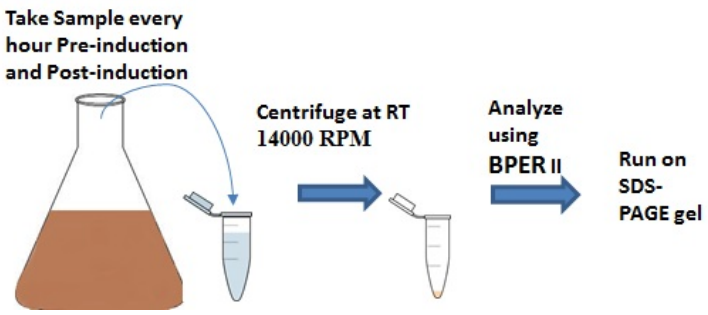

Figure 2.13. Determining soluble vs. insoluble content. Process of using BPER II to determine insoluble vs. soluble protein content.

To analyze the frozen pellets the following protocol was applied. Thaw the pellets for 10 minutes at room temperature and then re-suspend the cells in 150 µl of BPER II reagent by vigorous vortexing of the mixture until the cell suspension is homogeneous, then continue for one more minute. Following this centrifuge at 14,000 RPM for 5 minutes to separate the soluble proteins from the insoluble proteins. At the completion of this step separate the supernatant from the pellet. The supernatant contains the soluble fraction and will be used in SDS-PAGE analysis. Re-suspend the pellet in 150 µl of BPER II reagent, which contains the insoluble fraction for SDS-PAGE analysis. After the separation of the components run SDS-PAGE gel with 15 µl of each fraction to determine the solubility content.

SDS-PAGE gels were run with 15 well 4-20% gradient Tris-HEPES-SDS gel (Pierce) and samples were prepared in 4X loading buffer containing 1% SDS and DTT and run in

Tris-HEPES loading buffer on a mini protean gel system (Bio-Rad). Sample volumes of 15 µl were prepared and combined with 5 µl loading buffer and a full range rainbow molecular weight marker was used (GE healthcare). This is a representation of how the samples were loaded on the gel.

1	2	3	4	5	6	7	8	9	10	11	12	13	14	15
Marker	1hr pre sol	1hr pre insol	3hr pre sol	3hr pre insol	5hr pre sol	5hr pre insol	1hr post sol	1hr post insol	3hr post sol	3hr post insol	4hr post sol	4hr post insol	5hr post sol	5hr post

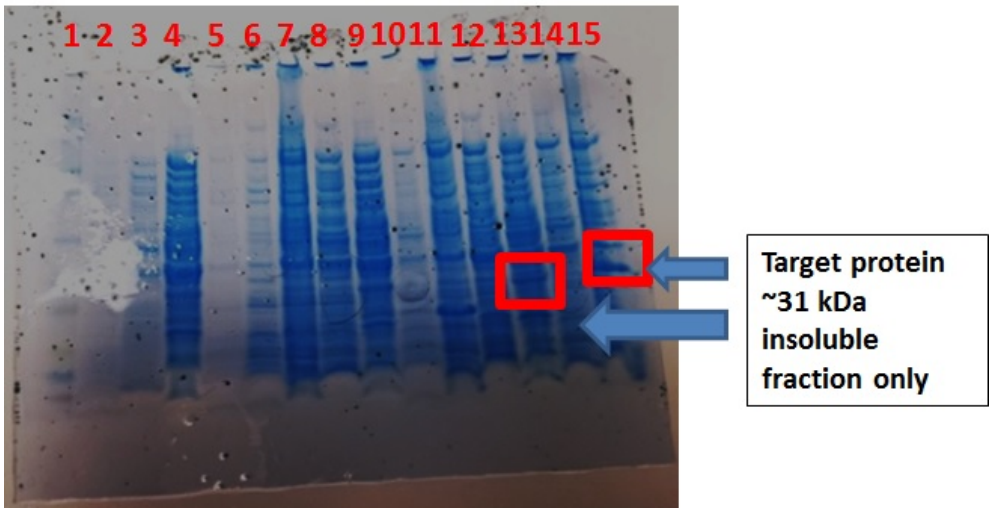

Figure 2.14. SDS-PAGE to determine soluble vs. insoluble protein content. The ELP-IMG protein was only visible in lanes 13 and 15, which are insoluble fractions 4 and 5 hours post induction with IPTG.

The results from this SDS-gel showed that the protein was in the insoluble fraction and thus standard ITC purification would most likely not be successful in purifying the protein.

2-6-2. Insoluble protein purification methods used to purify ELP-IMG and ELP-THO

There were five methods attempted to purify the fusion proteins. All methods require the purification to occur using the pellet from the first cold spin, which is where the insoluble protein is located. This is opposite to the regular purification procedure where the protein is purified from the supernatant. The first method was to follow the insoluble protein purification methods that are laid out with the BPER protocol, which is used for general inclusion body purification. The method was as follows:

Method 1: BPER Purification

After spinning the culture media down, the next step was to re-suspend the 1st cold pellet in 10 ml of BPER and vortex until the solution was homogeneous. This was followed by centrifugation for 25 minutes at 4°C and 27,000xg after which the supernatant was poured off and discarded. Then 200 µl of 10 mg/ml lysozyme stock solution was added to to the pellet followed by 19.8 ml of 1:20 diluted BPER II reagent. Once the pellet was re-suspended it was centrifuged for 25 minutes at 4°C and 27,000xg and the supernatant from this step was poured out. This process was repeated 2 more times then the final pellet was re-suspended in 2 ml of 6M Guanidine HCL. This solution gets diluted 20 fold using refolding buffer (50 mM K_2PO_4, 100 mM NaCl) and left to chill at 4°C for 48 hours. At the completion of the 48 hours the solution was centrifuged for 25 minutes at 4°C and 27,000xg and the resulting supernatant from this spin contained the final protein.

This protocol produced extremely poor yields of no more than 20 mg / L of culture, even after attempts at concentrating the solution using various methods. Particle formation was also non-existent. This can be explained, however, by the fact that the yield was never sufficient enough to keep the salt content low enough to be in the proper salt regime. It is believed that the extra steps in the BPER protocol were not necessary, and the excess centrifugation caused loss of protein.

Method 2: Purification using pure GVGVP$_{40}$-foldon

The first step was to re-suspend the first cold pellet of both GVGVP$_{40}$-foldon and ELP-IMG in 10 ml of 6M guanidine hydrochloride and combine the two. The solution was then vortexed until it was homogeneous followed by a dilution of the the solution 20 fold through addition of 380 ml refolding buffer and finally left to sit for 72 hours at 4°C. Centrifugation followed for 25 minutes at 4°C and 14,000xg, after which the supernatant was poured into another tube as it contained the fusion protein in the soluble fraction. It was then incubated at 45°C and the purification proceeded with these 380 ml as the first hot spin in regular ELP purification

This method produced yields between 30-40 mg / L of culture, which is far less than would be expected for GVGVP$_{40}$-foldon alone (typically 80-100 mg /L). This yield is sufficient, however SDS-PAGE analysis showed an anomaly with the protein (Figure 2.15). The multiple trimer domains that are present in this form of the construct caused issues with the self-assembly of nanoparticles leading to bi-modal distributions as the only particle populations that could be achieved. This is not optimal for use of the construct, so this method was not used. The next method skipped BPER and GVGVP$_{40}$-

foldon co-purification entirely and went directly to incubation in 6M guanidine hydrochloride.

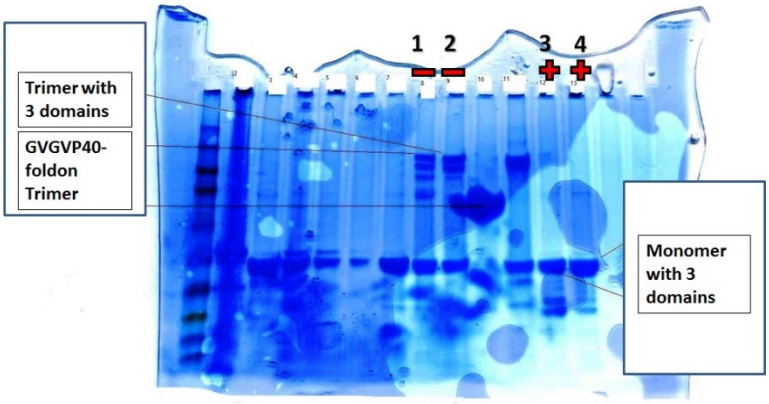

Figure 2.15. SDS-PAGE gel method 2. SDS-PAGE gel for purification using method 2, showing the multiple trimer domains as a result of the combination of proteins.

Method 3: Purification using pure 6M Guanidine HCL

The first cold pellet was re-suspended after sonication and centrifugation of ELP-IMG in 10 ml of 6M guanidine hydrochloride. The solution was vortexed until homogeneous and let sit for at least 6 hours. Then it was diluted 20-fold through addition of 180 ml refolding buffer and let sit for 72 hours at 4°C. Followed by centrifuging for 25 minutes at 4°C and 14,000xg and pouring off of the supernatant from this step. The supernatant was incubated at 45°C for 4 hours and centrifuged for 25 minutes at 40°C and 27,000xg. The supernatant from this spin was discarded and purification proceeded with the pellets. This yields 6 pellets in 6 tubes, which need to get purified individually. 250 µl of 6M guanidine HCL was added to each pellet and stirred gently until homogeneous, then re-suspended 1:20 with 4.75 ml of refolding buffer, with the eventual combination of all 6 pellets. This solution was then centrifuged for 25 minutes at 4°C and

27,000xg. The supernatant was then used to proceed with hot spin and was incubated at 45°C for 4 hours, followed by centrifuging for 25 minutes at 40°C and 27,000xg. At the conclusion of centrifuging the supernatant was discarded and purification proceeded with the pellet. The final pellet was re-suspended in 5 ml of appropriate solution and the concentration was measured.

This method successfully purified the protein with yields of 20-25 mg / L of culture. Self-assembly of nanoparticles took place as expected, however, the yield was less than optimal and the solution tended to have a very slight cloudy appearance and would precipitate if stored for more than 30 days.

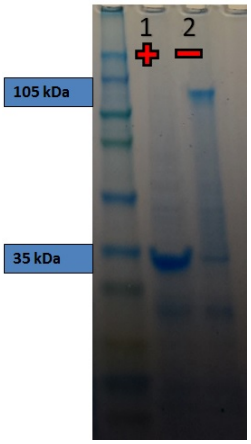

Figure 2.16. SDS-PAGE gel method 3. SDS-PAGE gel resulting from the method 3 purification schematic**.** Lanes with the + symbol indicate samples that were heated to 100°C to denature the foldon domain, while lanes with the – symbol indicate samples that are at room temperature, which we expect to trimerize due to the activity of the foldon domain. Lanes 1 shows the monomer form as expected while lane 2 shows trimer formation.

Method 4: Purification using pure 8M Urea and ITC:

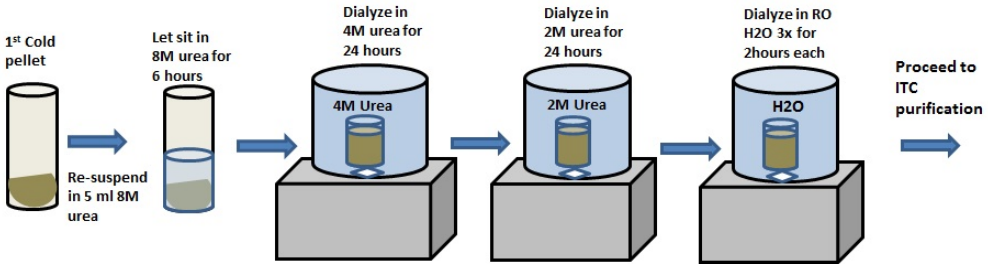

Figure 2.17. 8M urea + ITC purification method.

The first step was to re-suspend the first cold pellet in 5 ml of 8 M Urea and vortex until the solution is homogeneous, followed by sitting for 6 hours at room temperature. Then it was dialyzed against 4 M urea for 24 hours using 3000 MWCO dialysis tubing (Spectra-Por), followed by dialysis against 2 M urea for 24 hours using 3000 MWCO dialysis tubing (Spectra-Por). This was then dialyzed again using 3000 MWCO dialysis tubing (Spectra-Por) against RO H_2O for 2 hours with 3 changes of the water. Following this the solution was purified using the ITC method described earlier.

This method has been used to successfully purify the protein with high purity (Figure 2.18) and yields that are between 25 and 30 mg/L of culture. Self-assembly of nanoparticles took place as expected, however, a higher yield was desired. This method also eliminated the cloudiness as well as the precipitation problem.

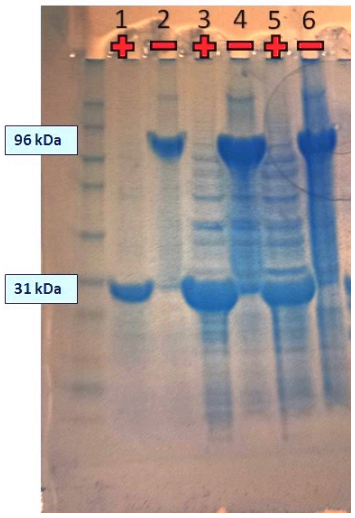

Figure 2.18. SDS-PAGE gel method 4. Lanes with the + symbol indicate samples that were heated to 100°C to denature the foldon domain, while lanes with the – symbol indicate samples that are at room temperature, which we expect to trimerize due to the activity of the foldon domain. Lanes 1 and 2 are completely purified samples, while 3-4 and 5-6 are samples that are no 100% purified and require another round of ITC.

Method 5: Purification using pure 8M Urea Only:

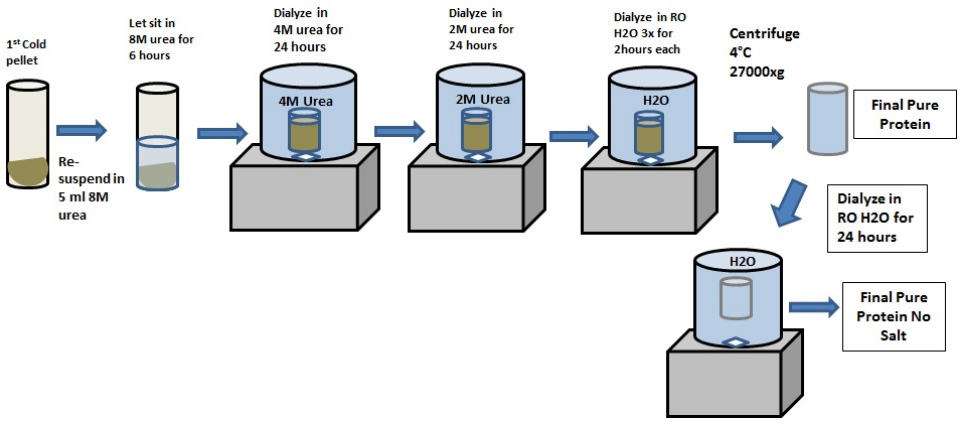

Figure 2.19. 8M urea only purification method.

The steps used in this method mirror the steps in method 4 up to the point of ITC purification. Instead of the usual 2.5 rounds of ITC, there was only one round of centrifugation at 27,000xg at 4° C. This was then followed by another round of dialysis in pure H_20 for 24 hours. At the conclusion of this the purified protein was present and ready for use.

This method has been used to successfully purify the protein with high purity (Figure 2.20) and yields that are between 70-90 mg/L of culture. Self-assembly of nanoparticles took place as expected and the yield was 2-3 times more than the other methods (Table 2.4), which makes this process ideal for sample preparation. This method also eliminated any cloudiness as well as the precipitation problem. Purification of the protein is performed using this method.

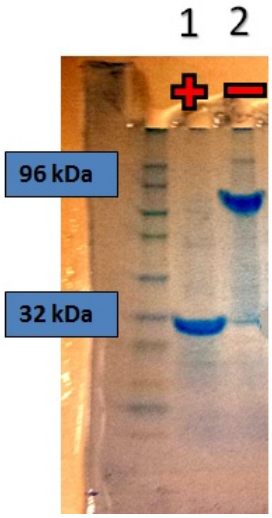

Figure 2.20. SDS-PAGE gel method 5**.** Lanes with the + symbol indicate samples that were heated to 100°C to denature the foldon domain, while lanes with the – symbol indicate samples that are at room temperature, which we expect to trimerize due to the activity of the foldon domain. High purity and yield are demonstrated in this gel.

Method	Additive	Nanoparticle formation	Yields (mg /L of culture)
1	BPER / lysozyme / GuHCL 6M	No	< 10
2	$GVGVP_{40}$-foldon	Bi-modal	30-40
3	6M GuHCL + ITC	Yes	20-25
4	8M UREA + ITC	Yes	25-30
5	8M UREA No ITC	Yes	70-90

Table 2.4. Summary of purification methods and their associated yields.

2.7. ELP-fusion protein characterization methods

ELPs after purification are characterized by a number of general methods to ensure molecular weight, folding behavior, purity, transition temperature profiles and nanoparticle formation of samples.

2.7.1. SDS-PAGE Gel

Polyacrylamide gel electrophoresis (PAGE) using sodium dodecyl suflate (SDS) anionic detergent to impart negative charge to the proteins is used to separate proteins according to their electrophoretic mobility. This is primarily a function of their molecular weight, such that larger proteins will take a longer time to migrate through the gel, while smaller proteins will migrate faster. Thus the technique is used to ensure that the purified protein is of the proper molecular weight. Further depending on the conformation of the protein and buffer or temperature used proper folding can be visualized (i.e. dimer or

trimer formation). A generalized procedure for running SDS-PAGE follows. ELP samples were prepared for analysis in 15 µl aliquots (highly concentrated samples should be diluted with H_2O, typically 5 µl sample + 10 µl H2O). Into these 5 µl of 4X DTT was added containing sample buffer dye. The sample was then heated to 100° C in a dry bath for at least 5 minutes and briefly pulsed in a micro centrifuge to collect condensation. Samples that need to visualize the trimer activity of foldon domain were not heated to ensure that the thermal stability limit of foldon is not passed. The gel box was then assembled and filled with running buffer and securing the gel in place. Samples were then loaded into gels using gel loading pipette tips and run at 100 V until the dye reached the bottom of the gel. At the conclusion of this the voltage was stopped and the gel cassette was removed, transferred to a plastic holder and washed 3X with RO H_2O. Comassie blue solution was added to the gel, covered and set on the shaker for at least 2 hours followed by de-staining with H_20 or de-staining solution (methanol/glacial acetic acid/H_2O).

2.7.2. UV-Vis Spectrophotometry

A spectrophotometer is used to measure the amount of light that passes through a sample in relation to the initial amount of light. In the case of our ELP fusion proteins, this is used to measure the onset of turbidity of the solutions by measuring at a constant wavelength, with a computer controlled temperature ramp. A brief procedure follows for the use of the Shimadzu UV-1800 series. ELP solutions were prepared in desired buffers and checked to ensure that they were free of turbidity or precipitation. The software was initiated and the method in the TM-Analysis software was set to read at 350nm with a sweep from 20-60°C at 1°C/min (can change if desired). If no turbidity is observed at the

completion, the T_t can either be above the range measured or the sample may be forming nanoparticles. At the conclusion of the run the T_t was determined by plotting the absorbance @350 versus temperature and find the steepest part of the turbidity curve. The point of intersection was found and this corresponds to the T_t.

2.7.3. Dynamic Light Scattering

Fixed angle dynamic light scattering is used to investigate the formation of nanoparticles of ELP fusion protein samples. The hydrodynamic radii of nanoparticles can be studied through the use of dynamic light scattering (DLS) in which a beam of light passes through the aqueous sample. As it passes through the sample the light is scattered by the particles in different directions and parts of the light then pass through a detector. The Brownian motion of the particles results in constantly changing measured intensity that fluctuates with time giving distribution intensity. The intensity-time correlation functions are then analyzed by software using algorithms to calculate the hydrodynamic radius of the nanoparticles. To accomplish this a Brookhaven 90 plus particle size instrument is used. Samples were measured at 350 nm, typically at a temperature below T_t (~20°C) and above T_t (~45-50°C). A brief procedure follows. Samples were prepared in appropriate concentrations of protein and salt for nanoparticle formation (<150 μM protein and <50 μM salt). The samples were filtered directly into cuvettes using .22μM filters (Millipore) and placed into the cuvette holder. BPIC software was opened and analysis was performed in triplicate (3 runs of 3 x 1minute each = 9 total).

2.8. Characterization of gadolinium loaded fusion protein samples

The ELP-IMG, ELP-IMG variations and ELP-THO proteins are defined by their fusion with the protein based MRI contrast agent CA1.CD2 domain. A critical component in determining the success of the fusion protein, and the construct as a whole is the successful binding and retention of gadolinium.

2.8.1. Inductively coupled plasma optical emission spectroscopy

Inductively couple plasma optical emission spectroscopy (ICP-OES) is an analytical technique used for the detection of relatively low amounts of metals in samples. This instrument uses argon gas to ignite a plasma torch that excites atoms and ions that will emit electromagnetic radiation at wavelengths that match those of the element of interest. Intensity of the emission recorded corresponds to the concentration of the element within the sample, based upon creation of calibration curves. The plasma reaches a temperature of ~ 7000 K, while a peristaltic pump delivers the sample into a nebulizer to be analyzed by turning the sample into mist inside the plasma flame. This process will break the sample down into only charge ions, which undergo a rapid collision process inside the chamber and give off radiation that corresponds to the characteristic wavelength.

In designing the experiments to determine the Gd^{3+} content bound to the ELP fusion proteins there were some important considerations that took place. These were as follows:

A. Samples must be clear: no turbid, precipitated or non-filtered protein samples

B. Choice of wavelength: For Gd^{3+} use multiple as there is confusion as to which would be the best, these include 342 and 376 nm

C. Make sure 3 replicates are performed

D. Use an internal standard to ensure that the protein is not interfering with the atomizing of the gadolinium → typical between 80-120% internal standard recovery is acceptable

E. Add 2 ppm of rhenium to each sample as the internal standard

F. After construction of calibration curve ensure that it has an R^2 value of at least .999

G. Measure blank sample of pure 2% nitric acid in h20 + internal standard and the lowest standard has to have an intensity of at least three times the blank for the measurement to be accurate

When using the instrument the following steps took place. The argon flow was turned on from the wall, followed by switching on of the instrument. The computer was then turned on and the WinLab32 program was initiated followed by the opening of the "JCgd3+IS" method. When using the instrument, it was imperative to construct a new calibration curve each time to gauge instrument response (Figure 2.23). The inlet tubing was placed into the blank sample, held for 20 seconds then analyzed. After this, the inlet tubing was placed in a solution of 2% nitric acid for washing (after each run as well). For the running of each protein sample the same steps took place. Results were generated and the instrument was cleaned and shut down.

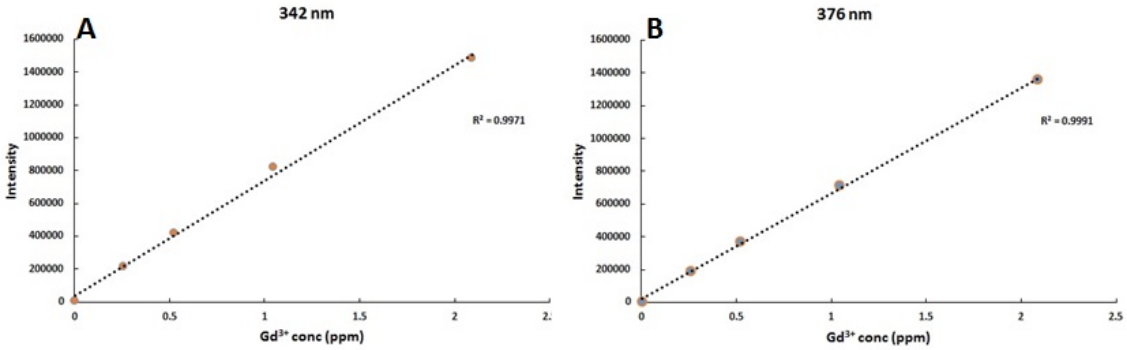

Figure 2.21. Calibration curves generated from ICP-OES analysis.

2.8.2. Free gadolinium detection assays

For any gadolinium chelating nanoparticle system there exists the possibility that unchelated gadolinium can exist in the formulation either due to instability of the soltion, excess gadolinium due to lack of available binding sites or precipitation. Free gadolinium is a known toxicant, which has been linked to nephrogenic systemic fibrosis in FDA approved MRI contrast agents[208]. For these reasons it is critical to have assays available to be able to detect whether or not there is free gadolinium present in the solution.

Arsenazo III ($C_{22}H_{16}As_2Na_2N_4O_{14}S_2$) is a bis-azo derivative of chromotropic acid (Figure 2.22) and is capable of forming stable complexes with a large number of ions[209]. Specifically it binds to metal ions forming a metal-ion complex but does not bind to complexed metal ions. This method allows for both a visual and numerical detection of this interaction. Visually there is a colorimetric interaction that occurs with a solution of pure aresenazo III appearing pinkish in color, as well as in solutions with little to no free gadolinium present. As the amount of free gadolinium increases the color shifts from pink to purple to finally green when there is an excess of free gadolonium in solution[210](Figure 2.23). These color shifts are also represented in a shift of the

abosrbance spectrum. When the dye is free in solution there is a strong absorption peak at 548 nm and when complexed with metals there is a peak absorption at 652 nm (Figure 2.24).

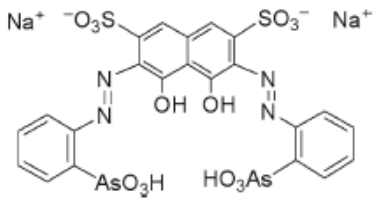

Figure 2.22. Chemical structure of Arsenazo III

Figure 2.23. Examples of ELP-Gd^{3+} arsenzao III complexes. Sample 1: Free Arsenazo III (pink), sample 2: 40foldon-CA1.CD2 with 5 μM $Gd3^{+}$ added drop-wise (all bound purple) sample 3: 40foldon-CA1.CD2 with 20 μM $Gd3^{+}$ added drop-wise (all bound purple) Sample 4: 40foldon-CA1.CD2 with 250 μM $Gd3^{+}$ added drop-wise (excess present as an intermediate orange) Sample 5: 40foldon with 5 μM $Gd3^{+}$ added drop-wise (excess present green).

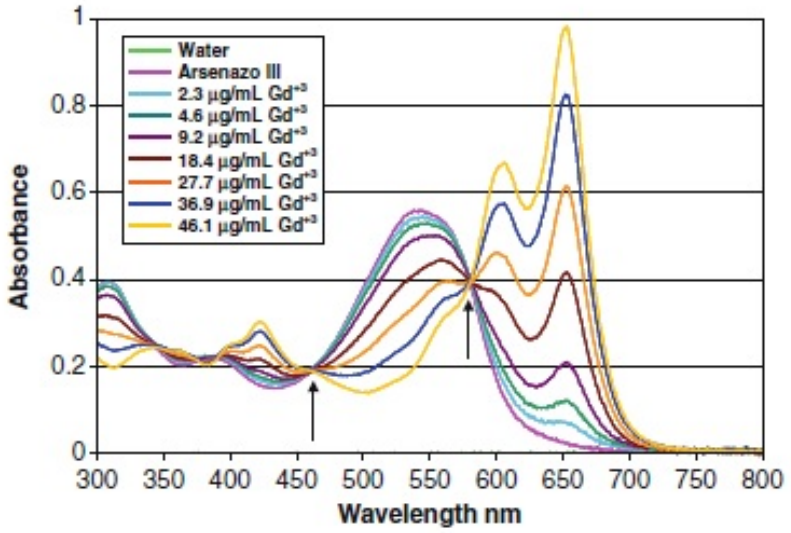

Figure 2.24. Absorption spectrum of Arsenazo III calibration standards.

The first step undertaken to perform the assay used in this study is to make a series of standards, which leads to the creation of a calibration curve, which is then used to determine the concentration of free gadolinium. The presence and amount of free gadolinium in protein samples can then be quantified using Arsenazo III. To construct the calibration curve gadolinium chloride (MW 263.61, Acros) is dissolved in water at concentrations spanning 0-48 µg / ml or 0-182 µM. A 20 mg/ml solution (21.8 mg dissolved in 1 ml RO H2O) is made which is used a stock solution and then diluted to 2 mg/ml in 1 ml which is used to make the calibration stocks (Table 2.5).

Sample	Volume of stock	Volume h20	GdCl H_20	Gd (µg/ml)	Concentration (µM)	Absorbance
1	0	1000	0	0	0	0
2	1.55	998.45	3.39	2	7.59	0.026
3	3.1	996.9	6.78	4	15.17	0.06
4	6.22	993.78	13.56	8	30.35	0.135
5	12.43	987.57	27.12	16	60.70	0.306
6	18.66	981.34	40.68	24	91.04	0.48
7	27.98	972.02	61.02	36	136.57	0.728
8	37.32	962.68	81.36	48	182.09	0.93

Table 2.5. . Calibration Standards for Arsenazo III. Calibration standard preparation table and their resulting absorbance measurements.

To measure the calibration standards, which were made into 1 ml volumes, 100 µl of 0.2 mM Arsenazo III, 50 µl of calibration standard (represented as sample 1-8) and 850 µl of water are mixed together. A blank is created composed of just 950 µl water and 50 µl Arsenazo III. A UV-vis spectrophotometer (Thermo Scientific Bio-mate 3) was used to get the absorbance readings at 652 nm, using the Arsenazo III and water standard as the blank. A Beer's law plot is constructed by plotting the absorbance at 652 nm versus Gd^{3+} concentration.

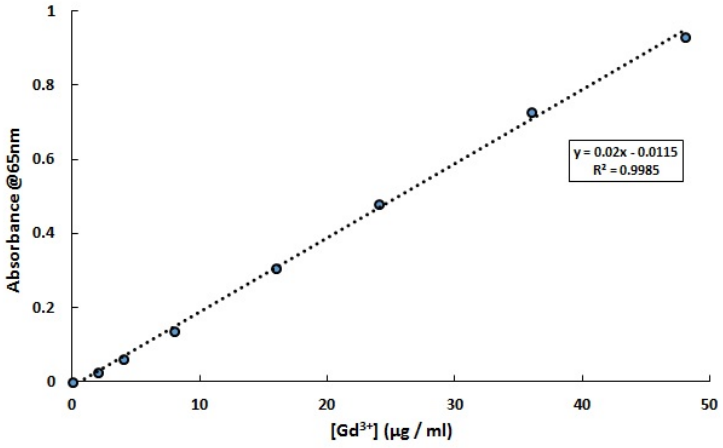

Figure 2.25. Calibration curve of arsenazo III. Arsenazo III calibration curve constructed from a series of standards. The slope of the line represents the extinction coefficient used in this study.

To determine the amount of free gadolinium present in a sample the same procedure is applied but instead of 50 µl calibration standard 50 µl of nanoparticle / Gd^{3+} conjugate is added. The mixture is composed of 850 µl water, 50 µl sample and 100 µl of Arsenazo III. The absorbance of the sample is then divided by the extinction coefficient as represented in equation

$$[\boldsymbol{Free\ Gd}\ (\boldsymbol{\mu g\ /ml})] = \frac{Abs\ of\ sample + 0.01}{0.02} * 1000$$

This assay covers a range of 0-182 µM of free gadolinium that may be present in the sample. As most of the samples presented in this study have a working range of 10-150 µM gd^{3+} present, this represents an easy way to determine the amount free. For simplicity purposes and ease of facilitating a large number of samples, a microplate reader can be substituted for the UV reader. A Synergy H1 microplate reader (Biotek) with a 96 well plate was also used to process a series of samples (Figure 2.26).

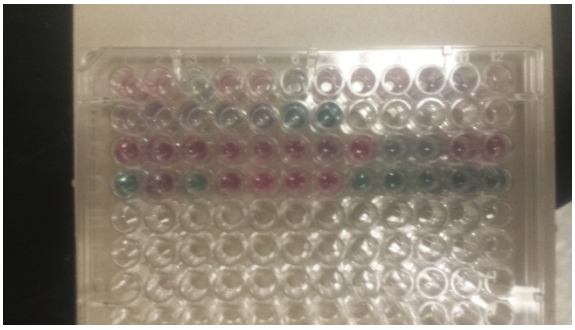

Figure 2.26. ELP samples in 96 well plate for microplate analysis. ELP-Gd^{3+} samples in 96 well plate to test for amount of gadolinium present. Sample preparation also gives a visual representation of gadolinium present in excess.

Xylenol Orange Assay

Another common indicator for presence of lanthanide ions is xylenol orange[211], whose chemical structure is represented in Figure 2.27. The color of the solution of xylenol orange is largely dependent upon the pH; at acidic pH the solution is yellow, while at basic pH the solution is purple. The change in color is due to the de-protonation of the phenolic hydroxyl group, which in turn leads to an extended electronic de-localization which then shifts the absorption wavelength to higher values[212]. This effect is the same in the presence of metal coordination. When a stable Gd chelate is present such as the one presented in this study or any of the many clinically available (Gd-DTPA, Gd-DOTA and derivatives) the xylenol orange is not able to extract the metal ion from the chelate, thus any change in color or absorbance is only due to free metal ions.

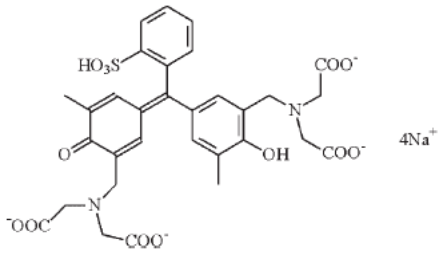

Figure 2.27. Chemical structure of xylenol orange

Xylenol orange, like Arsenazo III, is able to provide both a visual and numerical representation of the free Gd^{3+} in a solution. Xylenol orange has two absorption maxima, at 433 and 573 nm, with the 433 being more intense. As free Gd^{3+} increases in the sample, the second band increases while the first one decreases (Figure 2.28).

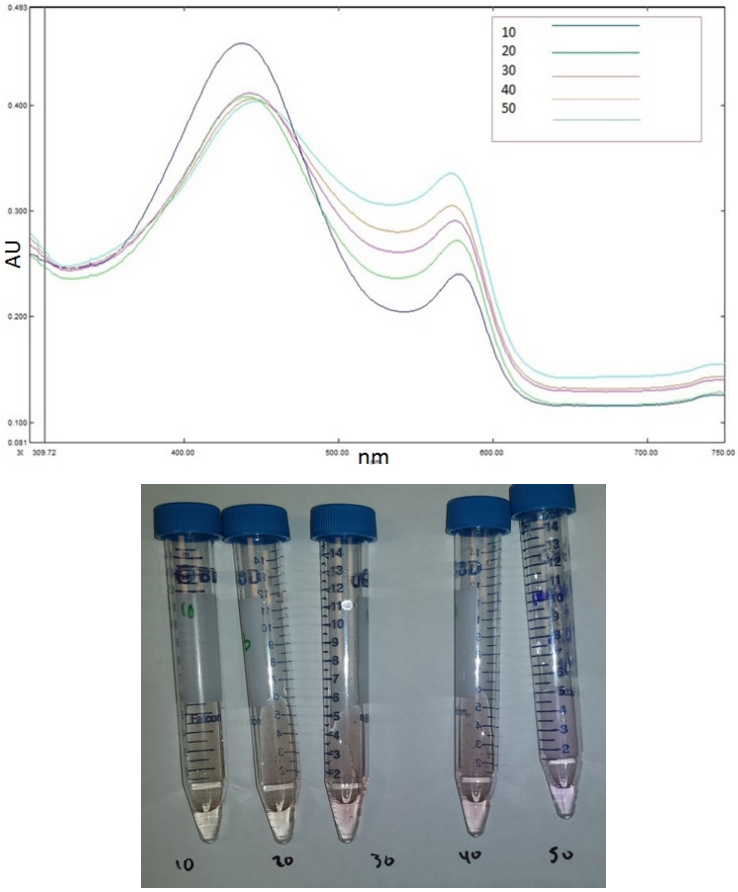

Figure 2.28. Xylenol orange chemical shift determined spectrophotometrically **a)** Gd^{3+} content as determined spectro-photometrically. Increasing Gd^{3+} content causes the band at 573 nm to increase while the band at 433 nm decreases. Spectra was taken in acetic buffer solution pH 5.8 across a range of gadolinium from 0-50 μM. **b)** Samples of Gd^{3+} + xylenol orange with the visible shift in color upon addition of excess free gd^{3+}.

In order to obtain this spectrum a working sample of xylenol orange was first prepared by dissolving 3 mg of xylenol orange (Acros) in 250 ml acetate buffer at pH 5.8. This working stock was frozen in 50 ml aliquots and protected from air, to prevent any issues with the pH of the solution. When the curve was ready to be prepared this solution

was thawed and 2 ml transferred to a quartz cuvette. Each gadolinium standard was prepared from a 1 mM stock (made from dissolving 3.72 mg of $GdCl_3$ (Acros) in RO H_2O) and made in 10- 80 µM concentrations. A 200 µl of each standard was added to the quartz cuvette and vigorously shaken to ensure complete mixture. A wavelength scan was performed using UV probe software on a UV-vis spectrophotometer (Shimadzu UV-1800) from 700 to 300 nm. The free Gd^{3+} content is proportional to the ratios of the 573 and 433 nm wavelength absorbance and across a concentration range of free Gd^{3+} a linear relationship is observed (Figure 2.29).

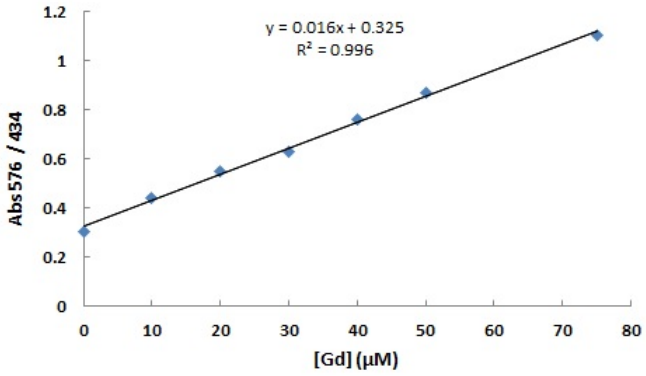

Figure 2.29. Calibration curve for xylenol orange. Calibration curve for xylenol orange / Gd^{3+} determined spectrophotometrically, as the ratio of two absorbance maxima.

To measure the amount of free Gd^{3+} in an ELP nanoparticle / Gd chelate, we use the slope of this line as an extinction coefficient and divide the absorbance of the solution by it, represented in equation;

$$[free\ Gd3+\ (\mu M)] = \frac{\left(Ratio\ Abs\frac{573}{433}\right) - 0.325}{0.016}$$

Examples of solutions of ELP nanoparticle / Gd^{3+} chelate are presented with the color shift being rather visible (Figure 2.30). The orange to light purple solutions correspond to < 10% free gadolinium while the brighter purple solution on the left is 27% free gadolinium.

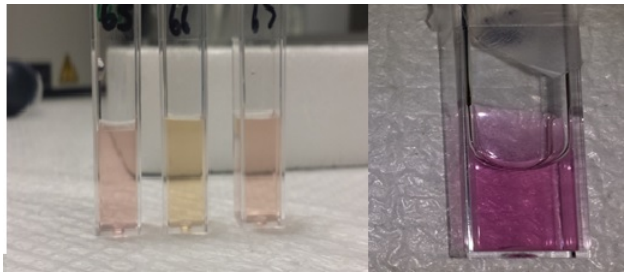

Figure 2.30. ELP-Gd^{3+} xylenol orange complexes. Examples of ELP / Gd^{3+} chelates in presence of xylenol orange solution used to determine free Gd^{3+} content.

Xylenol orange was also used to determine the saturation point at which addition of Gd^{3+} to ELP nanoparticle solutions exceeded the > 10% free Gd^{3+} limit (Figure 2.31).

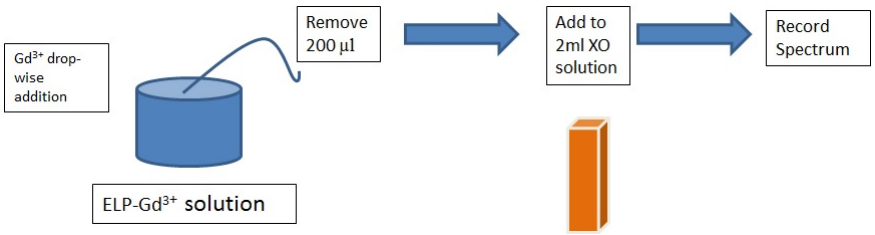

Figure 2.31. Using xylenol orange to determine excess amounts. Usage of xylenol orange to find point of gadolinium addition saturation.

A cross-linked protein of 50 µM concentration is placed in a 5ml round bottom flask and gadolinium in citrate buffer is added in a step-wise manner of 10µM drops with constant stirring. Thirty-minute time points are taken between additions of more

gadolinium. Before the addition of the next amount of gadolinium 200 µl of sample is removed and added to 2ml of xylenol orange solution and absorbance spectrum is recorded. Using the equation and the spectrum recorded it was found that as long as the addition of gadolinium was in 1:1 molar ratio with the protein, there was less than 10% free gadolinium in the solution. As the 1:1 ratio was exceeded the amount of excess increased significantly (Figure 2.32).

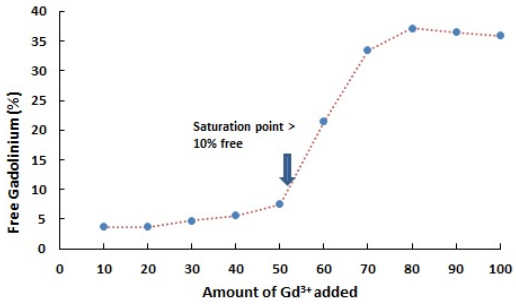

ratio abs	gadolinium addition (µM)	amt free (µM)	amt free (%)
0.331	10	0.375	3.750
0.337	20	0.75	3.750
0.348	30	1.4375	4.792
0.361	40	2.25	5.625
0.385	50	3.75	7.500
0.531	60	12.875	21.458
0.7	70	23.4375	33.482
0.8	80	29.6875	37.109
0.85	90	32.8125	36.458
0.9	100	35.9375	35.938

Figure 2.32. Gadolinium addition saturation point.

2.8.3. ELP-IMG metal binding complexes

Terbium III (Fisher Scientific) was used as a probe to determine metal binding affinities of ELP-IMG fusion proteins as compared to ELP-foldon. A Hitachi fluourescent spectrophotomer was used with an excitation wavelength of 283 nm and emission wavelength of 545 nm. Constant protein concentration of 50 µM was used for both ELP-IMG and ELP-foldon and these solutions were loaded into a quartz cuvette. Terbium III was titrated into the cuvette and measurements were recorded as a function of absorbance. From figure 2.33 it is clear that ELP-IMG has a dramatic increase in absorbance as higher concentration of terbium III is added to the cuvette, while ELP-foldon is virtually unaffected by the addition of the terbium.

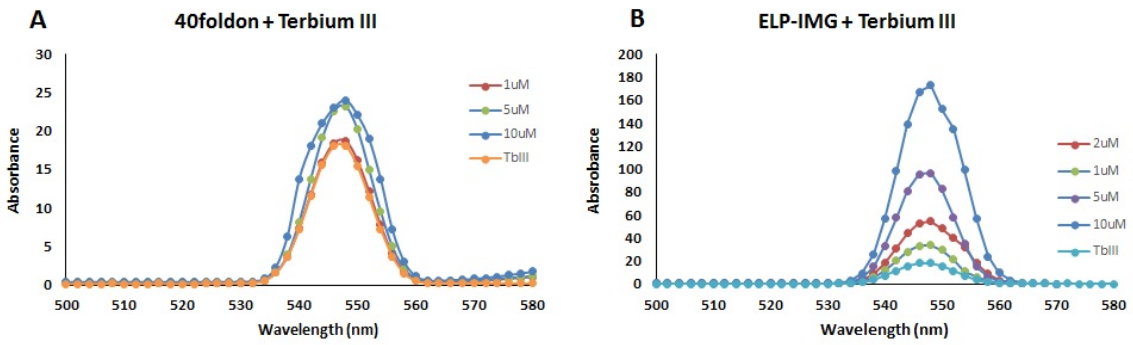

Figure 2.33. Terbium III + ELP-IMG vs Terbium III + ELP-Foldon. Comparison of ELP-IMG + Terbium III and ELP-Foldon + Terbium III showing that an increase in metal binding complex is seen for ELP-IMG, while ELP-Foldon has little to no effect on the terbium solution.

2.9. Detailed Cell Culture Protocols

To investigate the active targeting properties of ELP-THO constructs cancer cell lines were obtained, cultured and passaged. Cells were cultured from storage in vapor phase of liquid nitrogen in the following manner:

Culture protocol

Vial obtained from ATCC was thawed in a heat bath at 37°C while keeping the O-ring and cap out of water to avoid contamination. Once this was completed, the tube was removed from water and sprayed with 70% ethanol to decontaminate the surface. The tube was then spun at 125xg for five to 7 minutes in a micro centrifuge. At the conclusion of centrifuging the media was aspirated and the pellet was re-suspended in an appropriate amount of pre-warmed fresh growth media and incubated at 37°C and 5% CO_2.

Cell passage protocol

Cells were checked at appropriate intervals under a microscope and when they reached approximately 75% confluence and are fully attached to flask surface they were ready for passage. The first step was to remove and discard the cell culture medium into a separate flask. Then between 2 and 10 ml of Trypsin-EDTA solution was added to the flask and incubated at 37°C and 5% CO_2 for between 5 and 15 minutes. It is important to visually inspect the cells to ensure that they are detaching from the surface. At this point add 6 to 8 ml of fresh media to flask and transfer all of the contents to a 15 ml centrifuge tube followed by centrifuging at 125xg for 10 minutes to remove any excess trypsin present. The media was the aspirated and the pellet re-suspended in 10 ml of fresh growth media. Finally an appropriate amount of growth media was added to the flask and incubated at 37°C and 5% CO_2.

Well Seeding protocol

To seed the wells, for further study, from passaged cells 100 µl of the re-suspended cells were first transferred to a hemocytometer in order to count the total amount of cells. Once cell count was determined the amount needed per well was calculated and the appropriate amount of cell pellet suspension was added to the well, followed by filling to volume with fresh growth media. Once wells were seeded and filled they were incubated at 37°C and 5% CO_2. After 16 hours of seeding wells were checked to ensure that attachment was taking place and 24 hours after experiments were able to begin.

Protein incubation study protocol

To visualize proteins in cells they needed to be dyed with the use fluorescein isothiocyanate (FITC), which was dissolved in DMF at 10 mg/ml and mixed completely. Once the solution was mixed a 15-20 fold molar excess of FITC solution was added to the protein and immediately mixed. The solution was then incubated for 1 hour at room temperature, and wrapped in aluminum foil to protect from light. Before use, the solutions need excess FITC to be removed either through dialysis or use of the dye removal columns. Finally, once they are ready, they can be incubated with cells in appropriate molar concentrations for desired time periods.

Protein and cell interaction analysis—Cell fixation protocol

After the desired incubation time of protein and cells is reached the first step is to aspirate the media from flask and then wash the cells with sterile ice-cold PBS 2 times, followed by removal of media and PBS. The cells were then washed with ice cold 4% paraformaldehyde (PFA) solution for 5 to 8 minutes, followed by removal of the PFA solution and a wash step with ice cold PBS for 5 more minutes. At this point DAPI solution is added to the well to stain the nuclei and let to sit for 5 minutes, after which inverted field microscopy was started.

Antibody Detection protocol

Level of gastrin-release pepetide receptor content was visualized using the following antibodies; Anti-gastrin release peptide primary antibody (Ab22623) and goat polyclonal secondary antibody to Rabbit IgG (compatible with primary) conjugated to Alexa flour 488 (Ab 96883) were ordered from Abcam. U87 RFP and PC3 cells both overexpress

GRP in a high level and thus we expected positive results from the antibody test, while H441 expresses at an extremely low level (figure 2.34). To perform these experiments the same fixation protocol was applied as discussed in step 5. After fixation with PFA, a solution composed of PBS containing 5% goat serum and .1% triton X-100 was added to the wells then allowed to sit for 20 minutes. The well was aspirated, then a solution containing 5% serum, .1% triton X-100 and 1% primary antibody and left to sit overnight at 4°C. Once this solution was removed the wells were washed 3 times with warm PBS for 5 minutes each time, to remove any unattached material. Next, while in the dark, the seconday antibody, which was contained in a solution composed PBS, 5% serum, .1% triton X-100 and .1% seconday antibody, was added to the well and left to sit 20 minutes in the dark. Finally DAPI is added to the well and imaged on the inverted field microscope.

A

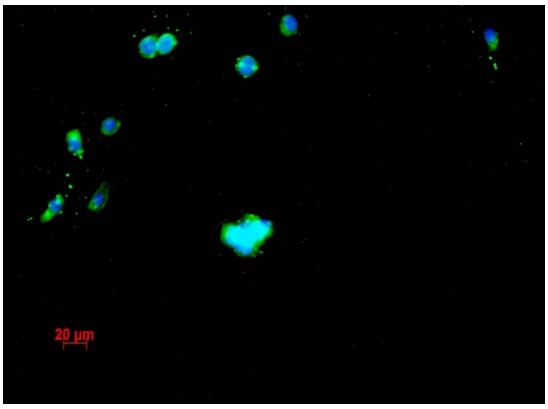

B

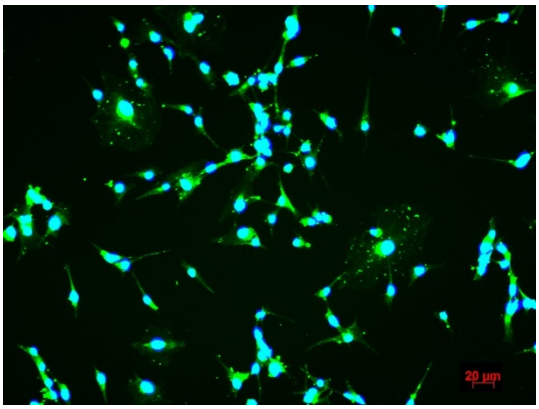

C

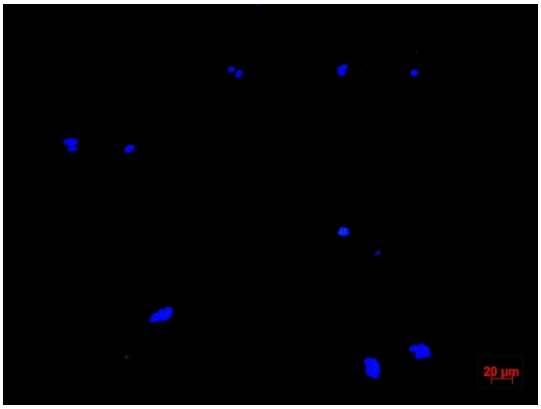

Figure 2.34. Antibody staining test. A) PC3 cells B) U87 C) H441. The positive indication of GRPR is displayed by the large amounts of green staining in A and B, while no green staining is present in C, indicating GRPR negative.

Live / Dead Assay Protocol

To determine the overall vitality of the cell population a Live / Dead assay can be used (Life technologies). The first step is to take a fresh passage of cells and seed them in wells at appropriate concentrations for 24 hours for at least 24 hours. After ensuring attachment and health of the cells, the media is changed and left to incubate at 37°C and

5% CO_2 for one hour. Protein samples at varying concentrations and for varying time points, are then incubated with the cells to determine the level of effect that they may be having on the cell population. Once incubation time has been completed, the media from the well is removed and 100-150 µl of live/dead media to the well, or enough to ensure complete coverage of the cells. All of these steps must be performed in the dark to ensure that the reagents are not activated by light. The combination of cells + proteins + live / dead assay mixtures is then incubated for at least 30 minutes at 37 °C 5% CO_2. At the end of this period the cells can then be imaged with an inverted fluorescent microscope or covered with D-PBS and stored for later viewing.

Imaging of Live/Dead results with ImageJ Software

During imaging take at least one image at each point in the well of interest using the green wavelength channel, one at red wavelength channel then save the images, and label appropriately. Make sure to take 4 images per well, representing each corner of the well and getting a good representation of the population as a whole (figure 2.35). It is also a good idea to take images using only the brightfield channel as a reference in case there is any auto-fluorescence. A second control that should be performed is to have one well that is left without any protein to represent an entirely alive population and to have a second well that is combined with a toxicant like 70% ethanol to represent an all dead population (figure 2.36). The next step is to open the ImageJ program and use the plugin called Shapelogic, which allows for counting of particles. Choose a region of interest and using the plugin count number of green and number of red particles. Using these numbers you can then make a ration of live to dead and find a survival percentage.

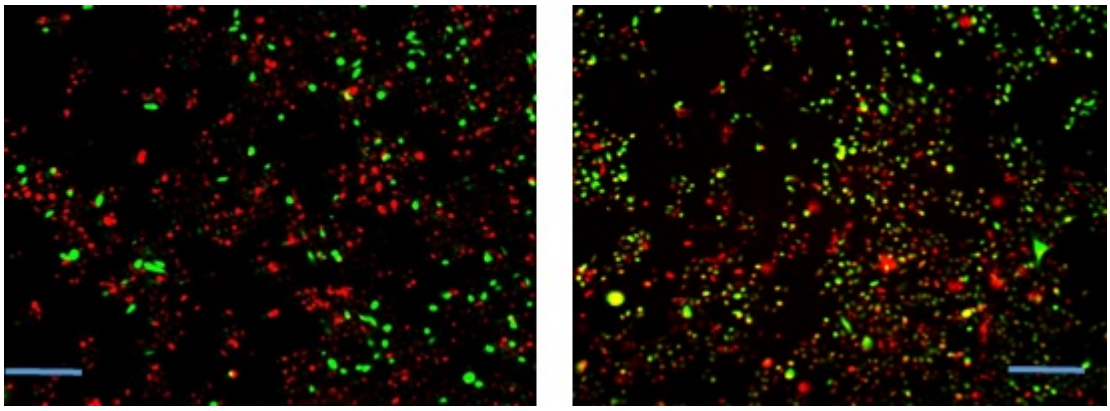

Figure 2.35. Live / Dead staining images with mixed populations.

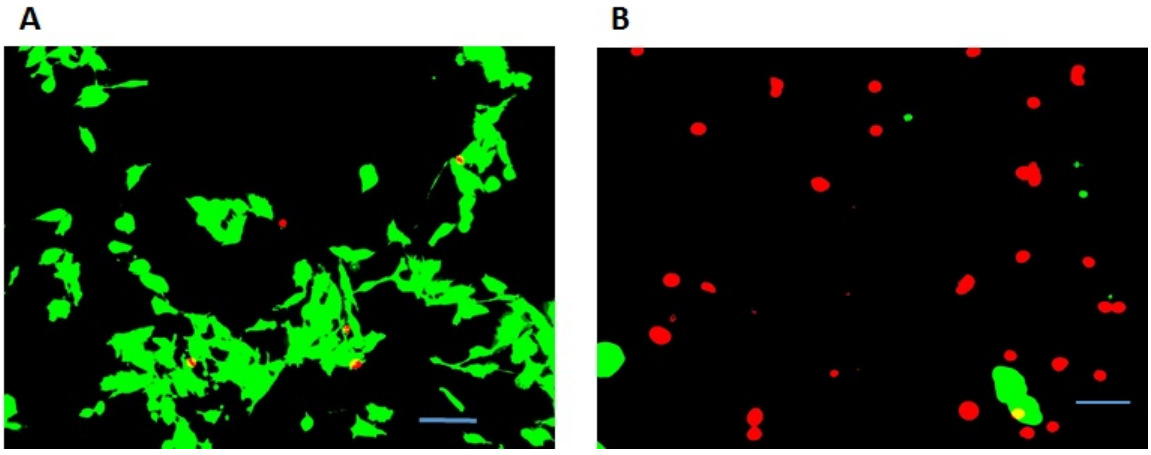

Figure 2.36. Live / Dead staining images with a) all live b) all dead. Live / Dead assay applied, to a sample as a positive control (all alive) A, and a negative control B (all dead).

2.9.1. Examples of Cell images

PC3 cells: The shape, spacing and homogeneity of the cells is a good indication they are healthy and growing well. As they grow more confluent than this they begin to cluster and will grow very rapidly. It is a good idea to keep the flask seeding density low if they are not planning on being used frequently (figure 2.37 A).

H441 cells: These cells tend to grow in a segregated and clustered manner. During growth it may appear that large quantities of the cells are not attaching, thus necessitating media changes that are not part of passaging. Also they may take longer time than the other two cell lines between passages and grow in lower number, so that must be planned accordingly when attempting to match up cell based experiments (figure 2.37 B).

U-87 RFP: These cells have been spliced with red fluorescent protein and thus they can be imaged in fluorescent microscope without the addition of dyes using the red wavelength channel. These cells are a nueroglioblastoma and grow in a branching manner out from a central area (figure 2.37 C).

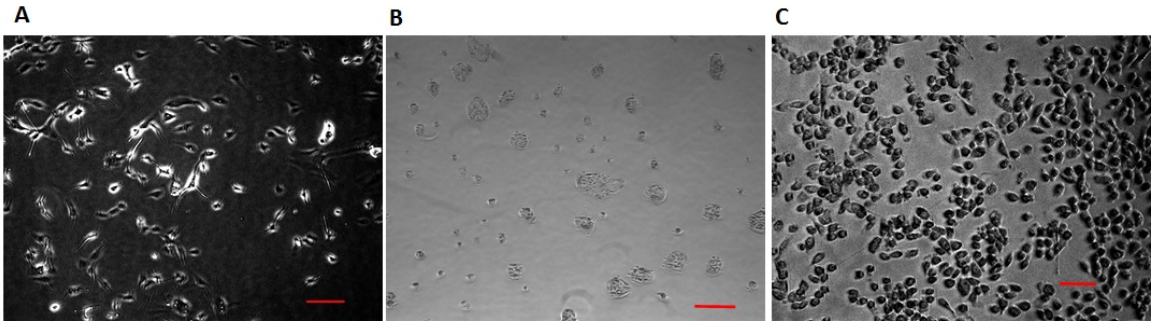

Figure 2.37. Images of healthy growth of cell lines. Bright field image of A) U-87RFP B) H441 C) PC3 cells taken as an example of healthy cell growth.

CHAPTER III

MRI ACTIVITY OF SELF-ASSEMBLING NANOPARTICLES OF ELASTIN-LIKE POLYPEPTIDES

3.1. Abstract

Presented is a fully protein based self-assembling nanoparticle system for use as an MRI contrast agent. These particles are formed using the thermally responsive behavior of elastin-like polypeptides (ELP's), which comprise the core of the particle. We have previously reported thermo reversible micelle formation of ELP's and have modified the system by fusing the protein based MRI contrast agent, CA1.CD2 to the C terminus of ELP-foldon to create a new system (ELP-IMG). Micelles formed by ELP-IMG are cross-linked to form stable nanoparticles. These nanoparticles are environmentally responsive, effectively bind and retain gadolinium while effectively providing contrast in *T1* weighted imaging with higher relaxivity than clinical contrast agents. This fusion protein is entirely protein based and was designed using molecular

biology techniques that allow for effortless expansion and modification of the construct. Due to these reasons this fusion protein serves as an excellent platform for the creation of a class of protein based theranostic nanoparticles. Here we detail the design, synthesis, expression, purification and characterization of the system.

3.2. Introduction

Soft material nanoparticles formed by self-assembly of polymer macromolecules is an area of great interest in cancer diagnostics and imaging[111]. Nanoparticles less than 150 nm in diameter generally avoid rapid clearance by the body[213], possess the ability to extravasate into the tumor vasculature and be retained there due to the enhanced permeability and retention effect (EPR)[67]. They can also utilize targeting ligands to allow them to be targeted to specific disease states[14]. The base platform for theranostic systems is a nanoparticle structure often composed of inorganic materials such as gold nanoparticles[214], magnetic iron oxide[144] or organic materials such as liposomes[215], polymer macromolecules[216] and polymeric micelles[217]. Multifunctional theranostic (therapeutics + diagnostics) nanoparticles are gaining traction in nano-materials research and can be described as materials that aim to combine these features into a single package[218]. These agents are capable of delivering a therapeutic dose to a molecular target and providing diagnostic imaging at the same time[5].

Magnetic resonance imaging (MRI) is a technique used to acquire images of the body that are of high resolution and depict the anatomy clearly. In order to use MRI for disease detection however, there needs to be a significant enhancement of signal due to diseased tissues and healthy tissues having similar signal intensity[139]. An approach to enhance the signal is to use paramagnetic lanthanide ions such as gadolinium as contrast

agents, which interact with water protons and lead to a decrease in *T1* relaxation time[219]. The most common MRI contrast agent clinically approved for use are gadolinium-DTPA (diethylene triamine pentaacetic acid) or gadolinium-DOTA (1,4,7,10-tetraazacyclo-dodecane-1,4,7,10-tetraacetic acid). These contrast agents are limited by their relatively low relaxivities (~ 4-5 $mM^{-1}s^{-1}$), low rotational correlation time, limited number of coordinated water molecules and short tissues retention times[137]. A protein based MRI contrast agent, CA1.CD2[136] is a novel gadolinium chelating protein that was rationally designed to overcome these limitations and was chosen as the diagnostic imaging component of this nanoparticle based MRI contrast agent. CA1.CD2 is derived from domain 1 of rat CD2 and was rationally designed to contain a high coordination Gd^{3+} binding site. This domain displays large *r1* relaxivity values (~120 $mM^{-1}s^{-1}$), excellent contrast in *T1* weighted imaging, a hydration number q of 2, strong selectivity for Gd^{3+} over physiologic metals and enhanced tissue retention time[3-136]. Other features that made this a desirable fusion partner is that it is entirely protein based which is encoded using only oligonucleotides, is composed of β sheet architecture and has strong stability against pH changes. Further the domain displays no acute toxicity *in vivo* and was shown to be cleared through the kidneys[14].

We have previously reported the self-assembly of ELP micelles through the addition of a negatively charged trimer forming oligomerization domain[193] known as foldon[191]. These particles are temperature, pH and salt dependent and are some of the smallest ELP particles reported in literature[41]. Elastin-like polypeptides are part of a class of environmentally responsive biopolymers found in nature that are based on a repetitive peptide sequence of GαGβP[161]. The α position can consist of any amino acid and β

position can be any amino acid except for proline[161]. A distinct feature of ELP's is that they undergo a sharp phase transition above a specific transition temperature (T_t), known as a lower critical solution temperature (LCST)[220]. Transition from above and below the T_t is a reversible process which is dependent on the length, concentration and amino acid composition of the polypeptides, and can be triggered by many different stimuli including pH[189], light[221] and ionic strength[222]. Due to their responsive nature, biocompatibility and specific control potential of T_t, ELP's have been used as the platform for many ideas including drug delivery[223], tissue engineering[224], microfluidics[225] and hydrogels[226]. Using molecular biology techniques we were able to synthesize this system in a manner that allows for seamless integration of other domains[227].

ELP's used as the platform for protein based nanoparticle MRI contrast agents possess many distinct advantages. These include the ability to control the size of the particles, precise tuning of the transition temperature and mechanism of stimulus. Modification of the amino acid sequence using modular molecular biology techniques allows for any number of targeting ligands or motifs to be included in the system which will allow result in an accumulation of contrast agent at a site of interest and subsequently increasing local concentration[139], reducing dosage requirements[228] and avoiding potential side effects related to excess gadolinium[208].

This paper will detail the process of incorporating the protein based MRI contrast agent CA1.CD2 with the three armed star elastin like polypeptide micelles to form a new MRI active multifunctional nanoparticle system (ELP-IMG). We show that the fusion protein of CA1.CD2 and ELP micelles maintain their individual properties. The ability to combine multiple functional properties in a single peptide provides a simpler approach to

form theranostic nanoparticles, compared to other multi-step synthetic methods. In addition, it provides a modular approach for designing particles with different properties without the need for post-translational modification. Thus this new fusion protein can serve as a modular platform for use in environmentally responsive organic theranostic systems.

3.3 Materials and methods

3.3.1. Gene Design and Preparation

The gene encoding the ELP-foldon structure was synthesized as reported previously[193,229]. The base structure for the formation of particles has the amino acid sequence MGH$(GVGVP)_{40}$-GYIPEAPRDGQAYVRKDGEWVLLSTFL. The use of directional ligation makes the process modular, allowing for simple incorporation of other domains.

To synthesize the DNA that encoded the 99 amino acid CA1.CD2 gene, 18 oligonucleotides were synthetically assembled including an N-terminal and C-terminal primer[196]. A detailed explanation of the process can be found in the materials and methods section.

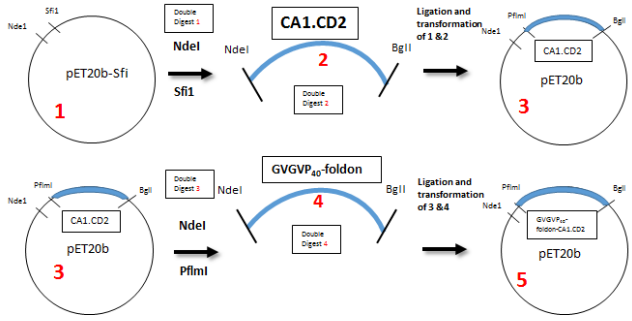

Figure 3.1. Schematic detailing the construction of the ELP-IMG fusion protein. Any variation of ELP can be used as the base component at the N terminal and peptide targeting sequences as well as spacing elements can be implemented at the C terminal.

3.3.2. Expression and Purification of Fusion Proteins

Starter cultures were prepared from frozen stocks in 10ml LB media supplement with 100 mg/L ampicillin at 37°C. The starter cultures were then added to 1 L of LB medium and shaken at 300 rpm and 37°C. OD_{600} readings were taken until the mixture reached a level between 0.9-1.0 at which time 240 mg of IPTG was added for induction. After 5 hours of shaking the cells were collected by centrifuging at 7000xg for 30 minutes. The cells were then lysed after being re-suspended in 30 ml of PBS using a sonic dismembrator. The soluble and insoluble fractions were separated by centrifugation at 4°C and 19000xg. ELP-IMG was determined to be in the insoluble fraction through SDS-PAGE analysis and thus the cold pellet contained the protein. It was then re-suspended in 10 ml of denaturing agent for 1 hour after which 190 ml of PBS was added and left to sit overnight. Centrifugation at 4°C and 7000xg followed and the protein was then present in the soluble fraction. Supernatant was collected and heated to 40°C at which point ELP-IMG precipitated out of solution followed by centrifugation at 17000xg

and 40°C. Two more rounds of the thermal cycling process were the performed and the final pellet was re-suspended in PBS.

3.3.3. Characterization of Proteins

Protein purity, trimer formation and molecular weight confirmation was performed using SDS-PAGE with 4-20% gradient Tris-HEPES-SDS gel. Samples were prepared in loading buffer containing 1% SDS and either heated above the denaturing temperature of the foldon domain[230] (>70°C) for 5 minutes or left at room temperature to confirm the association of foldon. Molar concentrations of the purified proteins were determined based on calculated extinction coefficients[231] and absorbance at 280 nm measured on a Biomate 3 (Thermo Scientific).

The transition temperature of the fusion protein was determined by measuring the UV-absorbance of solutions at 350 nm on a Shimadzu 1800 UV-vis spectrophotometer with an attached temperature control cell. 25 μM protein samples were made in PBS at neutral pH. Temperature ramp was done at 1°C / min across a range of 20-55°

Particle sizing was performed on a 90 plus Brookhaven particle size analyzer (Brookhaven Instruments). This unit is a fixed angle dynamic light scattering system with a Peltier temperature control system. Samples were made as 25 μM solutions in 1X PBS at varying pH conditions. The solutions were filtered using a .22 μM filter (Millipore) and loaded into quartz cuvettes. The pH was adjusted through the addition of filtered 1N NaOH.

Measurements were performed in triplicate and made in 2-minute long runs. The results were analyzed by the BIC software, which utilized a non-negatively constrained

least squares algorithm (Brookhaven Instruments) and were reported as mean diameter of multimodal size distribution (MSD).

3.3.4. Crosslinking of Nanoparticles

Protein samples of varying concentrations were diluted in filtered H_2O and had the pH adjusted to 10.2-10.4 using 1N NaOH. Stir bars were added to the sample and they were heated to 55°C with constant stirring for 1 hour. After 1 hour 10% glutaraldehyde was added to the solution to facilitate cross-linking of the micelles. Samples were kept in this state for at least 18 hours after which they were filtered using a .22 μM filter (Millipore). Samples were then dialyzed using 1000 Da MWCO 7 dialysis membranes (Spectra-Por) against PBS overnight. To test stability a sample of crosslinked particles was analyzed over a course of 44 days both above and below the T_t. Particle size measurements of the cross-linked micelles were then analyzed as described.

3.3.5. Gadolinium Binding and Characterization

Gadolinium chloride in citrate buffer at pH 4 was added to protein samples in appropriate molar concentrations with constant stirring overnight. Samples were then dialyzed at 4°C against PBS for at least 6 hours. After the addition of Gd^{3+} to protein solutions the samples were dialyzed to remove any potential excess Gd^{3+} and tested using the xylenol orange[232] and Arsenazo III[233] assays to ensure there was no free gadolinium present. Confirmation of the amount of gadolinium bound to fusion protein samples was determined by inductively coupled plasma optical emission spectroscopy (ICP-OES) [Perkins-Elmer] after the samples were diluted 300 times in 2% nitric acid.

T1 Relaxivity Measurements

Aliquots of varying concentrations of Gd^{3+} loaded fusion proteins were loaded into NMR tubes. The *T1* values of the proteins were measured using a minispec Mq60 1.4 T 60 mHz analyzer (Bruker). Runs were performed at 40°C and 10 points of measurement were taken. Relaxivity was calculated using the following equation: $R1 = \left[\left(\frac{1}{T1_{Gd}}\right) - \left(\frac{1}{T1_{Pbs}}\right)\right]/C$, where C is the concentration of gadolinium bound to the protein.

In vitro MRI Imaging

MRI images were obtained on an Espree 1.5T clinical scanner (Siemens). Samples were contained in NMR tubes containing at least 200 µl of sample and arranged asymmetrically in a plastic rack holder. Control samples consisted of H20, PBS, and free Gd^{3+} free in solution. Images were produced using a gradient echo sequence (TE = 5.12 ms, TR =150 ms, resolution matrix 512x336, 111 slices, slice thickness= 2mm). Sample images were collected and analyzed using OpenDicom viewer software.

3.4 Results

Protein Synthesis and Expression

The fusion protein was successfully synthesized and purified with a yield between 70 and 90 mg per liter of culture. SDS-PAGE (Figure 3-2) showed that when the foldon domain is heated above its thermal stability limit (lane 1 + symbol) we expect the trimer to dissociate into a monomer structure which is visible as the single band on the gel at 32 kDa. By keeping the sample at room temperature (lane 2 – symbol) we demonstrate the

proper folding of the foldon domain by showing trimer structures that are 3 times the molecular weight of the monomer at 96 kDa.

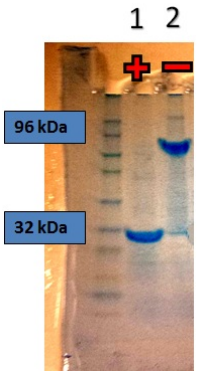

Figure 3.2. SDS-PAGE gel of ELP-IMG fusion protein structures. Samples were kept at room temperature (24°C) or heated above the thermal stability limit of foldon domain (100°C).

Transition Temperature Measurements

The transition temperature of the construct with bound Gd^{3+} and without bound Gd^{3+} was determined using a UV-vis spectrophotometer at 25 μM protein concentrations in PBS. The fusion protein at neutral pH and physiologic salt conditions has a T_t of 31.7°C. The addition of Gd^{3+} to the fusion protein has no effect on the T_t value of the system.

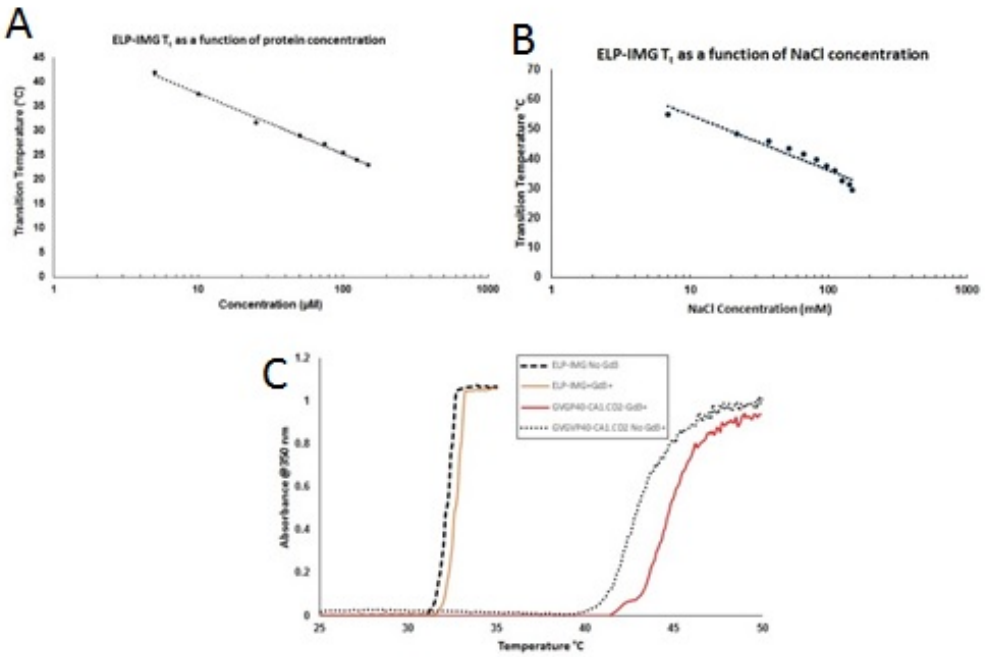

Figure 3.3. Transition temperature panel of ELP-IMG fusion proteins. A) ELP-IMG T_t as a function of protein concentration in PBS. B) ELP-IMG T_t as a function of salt concentration C) Determination of ELP-Fusion protein Transition temperature (T_t) as a comparison of linear and trimer structures. T_t is characterized for gd^{3+} bound proteins (solid) and proteins with no gd^{3+} present (dashes).ELP-IMG T_t as a function of concentration in PBS.

Construct	Sequence	Weight kDa	T_t (°C)
ELP40	MGH(GVGVP)40	17	41.5
GVGVP40-foldon	MGH(GVGVP)40- GYIPEAPRDG QAYVRKDGEWVLLSTFL	20	34.5
GVGVP40-CA1.CD2	MGH(GVGVP)40- GPGVGRDSGTV WGALGHGIELNIPNFQMTDDID EVRWERGSTLVAEFKRKMKPFLKS GAFEIDANGDLDIKNLTRDDSGTY NVTVYSTNGTRILDKALDLRILE	29	40.1
GVGVP40-foldon-CA1.CD2 (ELP-IMG)	MGH(GVGVP)40-GYIPEAPRDGQ AYVRKDGEWVLLSTFL GPGVG RDSGTVWGALGHGIELNIPNFQ MTDDIDEVRWERGSTLVAEFKR KMKPFLKSGAFEIDANGDLDIKN LTRDDSGTYNVTVYSTNGTRILD KALDLRILE	31.2	31.7

Table 3.1. Transition temperature comparison (25 μM in PBS).

Dynamic Light Scattering

Dynamic light scattering (DLS) was then used to confirm that micelle formation was occurring at low salt and high pH conditions as depicted in Figure 3.4. At neutral pH and high salt conditions aggregation occurs into particles above 700 nm in size. However, at salt concentrations below 20 mM and pH between 10.2-10.4 the construct forms particles ~ 32 nm in diameter. This is comparable to ELP-foldon[16] without the CA1.CD2 domain.

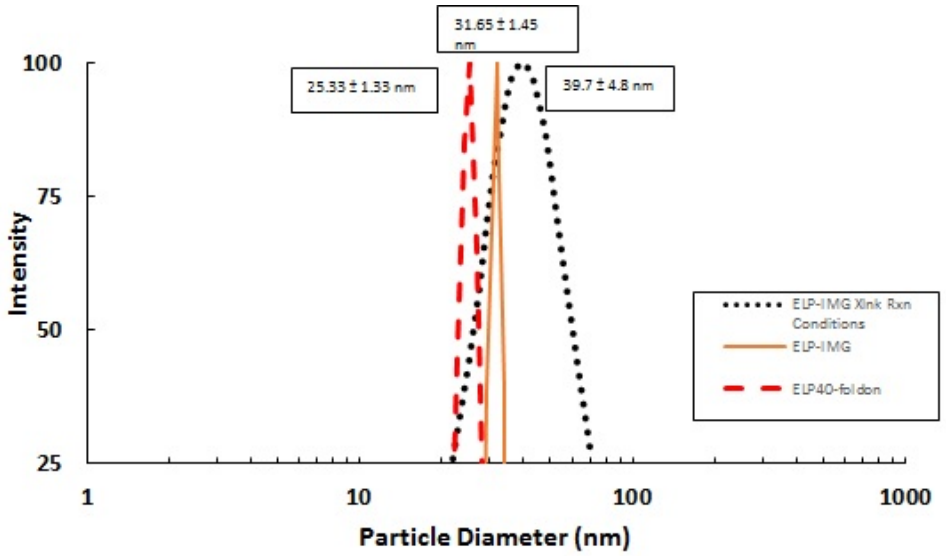

Figure 3.4. Dynamic light scattering of ELP-IMG compared to ELP-foldon. Tests were performed on samples of 25μM concentration at 42°C. A narrow distribution between 26 and 34 nm is observed. After crosslinking the size increased to ~40 nm with a broader distribution.

In order to prevent the samples from aggregating in physiologic conditions polypeptide micelles were cross-linked with glutaraldehyde. This cross-linking allows the system to exist as particles above or below the T_t in and dialysis in PBS prevents particle aggregation. The DLS results of the cross-linking experiment are shown in Figure 3.5. As the temperature is raised above the T_t (42°C), the constructs collapse and have an average size of 82.2 ± 5.7 nm and is not significantly affected by bound Gd^{3+} being present. To show the diameter changes that occur from crosslinking conditions to PBS, heated 4M NaCl was added in a drop-wise manner to crosslinked samples while continuously monitoring the particle size (Figure 3.7). In order to successfully complete this test the salt had to be added in time points of at least 15 minutes and had to be held at the same temperature as the protein in the DLS cell. The results are analogous to the dialysis

process, as the slow addition of salt results in particles that are approximately the same size as when the dialysis process is applied.

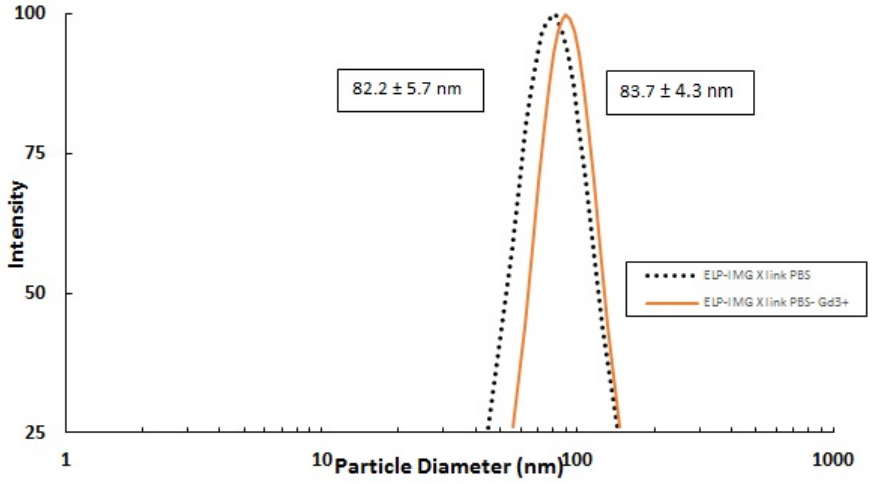

Figure 3.5. DLS of cross-linked ELP-IMG. Dynamic light scattering results of cross-linked solutions of 25 μM $GVGP_{40}$-foldon-CA1.CD2 fusion protein. Samples were cross-linked with 10% glutaraldehyde for 24 hours at 55°C filtered with a .22 uM filter, cooled and dialyzed against PBS. Samples were then transferred to quartz cuvettes Samples were run for in triplicate for 2 minutes each. After cross-linking the samples gadolinium solution was added in a drop wise manner then they were analyzed to determine if there was any change in particle size.

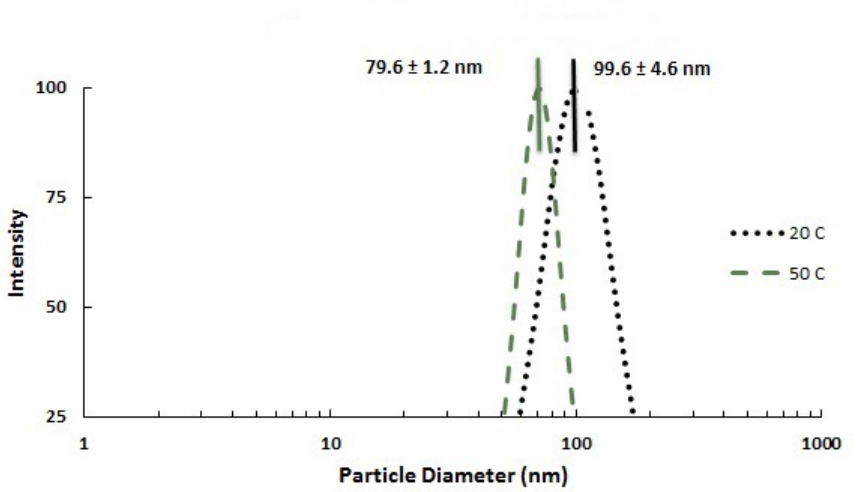

Figure 3.6. Shrinking and swelling behavior of crosslinked ELP-IMG samples in PBS.

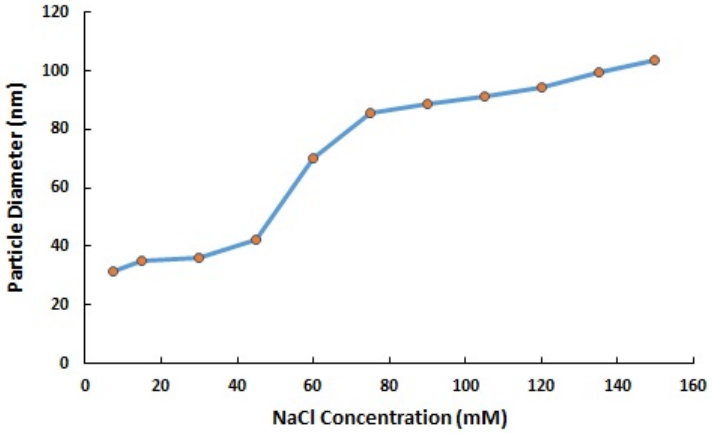

Figure 3.7. Particle size change in relation to amount of NaCl added.

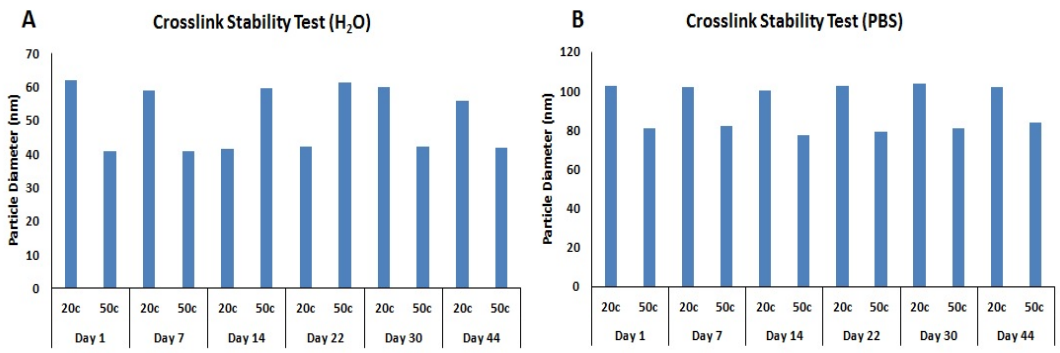

Figure 3.8. Crosslink stability of ELP-IMG samples in H_2O reaction conditions (A) and after dialysis in PBS (B)

When the crosslinked constructs are cycled from below to above their T_t, the strength of the crosslinks is confirmed and there is no longer dissociation of the particles into monomer form below the T_t (Figure 3.6). This shrinking and swelling behavior is carried over from crosslinking reaction conditions when dialysis in PBS occurs. Further these particles display strong stability over time, as they were tested over a course of 44 days. Each time they were tested particle size was measured above and below T_t, to ensure the stability of the crosslinks. Between tests samples were stored at 4°C.

Transmission electron microscopy on a FEI tecna G2 Twin instrument was performed on dehydrated cross-linked fusion protein samples. A 5 µL sample was placed on the TEM grid at room temperature and left to dry and any excess sample was wiped off the grid. The samples were then imaged at 160Kv as shown in Figure 3.9.

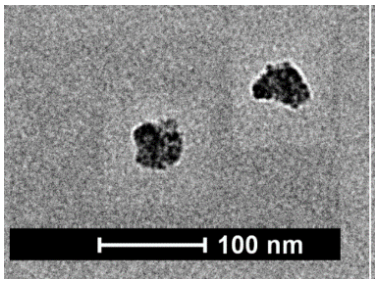

Figure 3.9. TEM results of crosslinked ELP-IMG in PBS. TEM results of dehydrated cross-linked 10 μM protein sample ELP-IMG constructs in 1xPBS and neutral pH.

Relaxometry

Gd^{3+} loaded fusion proteins were used to determine the *T1* relaxivity of the construct at 1.4T field strength. To ensure that no free Gd was present in samples the methods of section 2.7 were applied. Relaxivity values were plotted according to the following equation. Varying gadolinium concentrations and the slope of the resulting line gives the values for *T1* relaxivity (Figure 3.10).

$$\left[\left(\frac{1}{T1_{Gd}}\right) - \left(\frac{1}{T1_{Pbs}}\right)\right] = R1[Gd^{3+}]$$

The results of the relaxivity experiments show that the fusion protein is capable of providing *T1* relaxivity of 21.7 $mM^{-1}s^{-1}$for cross-linked nanoparticle samples, 31.7 $mM^{-1}s^{-1}$for soluble constructs samples and 34.8 $mM^{-1}s^{-1}$ for soluble monomers. These values are significantly higher than clinical MRI contrast agents (~4 $mM^{-1}s^{-1}$).

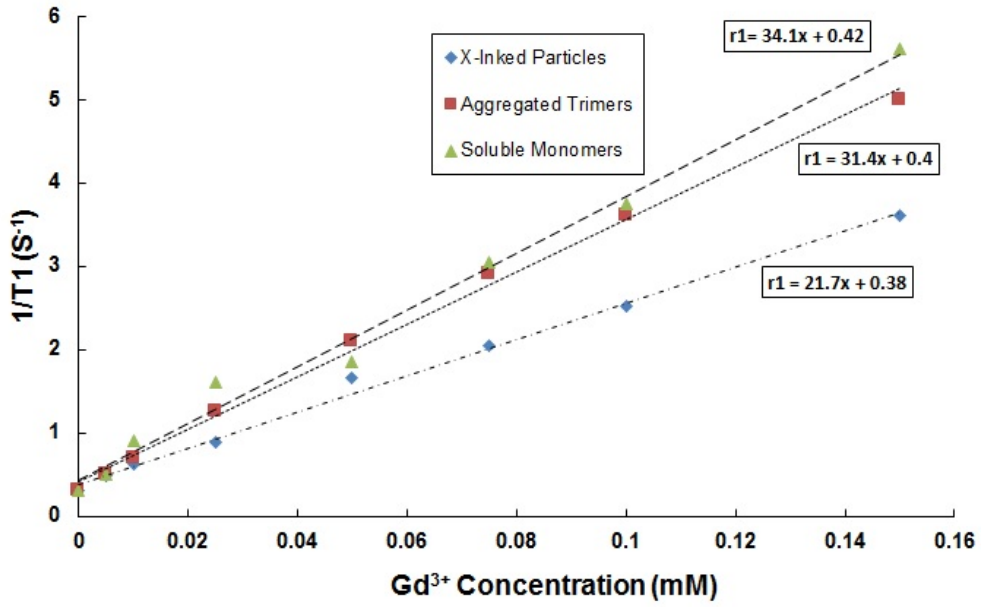

Figure 3.10. Relaxivity plots for ELP-IMG in various conditions. Relaxivity plots for cross-linked fusion protein samples, soluble trimer protein samples and soluble monomers. The results show a linear relationship between Gd^{3+} concentration and 1/*T1* values. The slope of the lines is the value of the relaxivity r1 of the constructs

In vitro MRI Imaging

The results of the MRI experiments confirmed the relaxometry findings. Fusion protein samples with bound gadolinium were used to determine the contrast provided in *T1* weighted images using a 1.5 T scanner (Siemens Espree). The results of the imaging show that the fusion protein is capable of producing contrast in *T1* weighting (Figure 3.11) and that the intensity of the contrast increases slightly with increasing Gd^{3+} concentration. These results correlate with what is found for the CA1.CD2 domain alone[136]

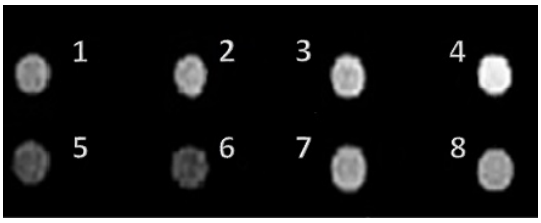

Figure 3.11. T1 weighted MR images of ELP-IMG. *T1* weighted MR image of fusion protein samples using GRE sequence (TE = 5.12 ms, TR =150 ms, resolution matrix 512x336, 111 slices, slice thickness= 2mm). Samples 1-4 are soluble protein samples at varying concentrations in 1xPBS and neutral pH. Samples 5-8 are cross-linked nano-particles and are in 1xPBS at neutral pH. The images are arranged in the following order 1) 0.025 mM Gd^{3+}- ELP-IMG 2) 0.050 mM Gd^{3+}-ELP-IMG 3) 0.1 mM Gd^{3+} ELP-IMG 4) 0.15 mM Gd^{3+} ELP-IMG 5) 0.01 mM Gd^{3+} ELP-IMG 6) 0.025 mM Gd^{3+} ELP-IMG 7) 0.05 mM Gd^{3+} ELP-IMG 8) 0.1 mM Gd^{3+} ELP-IMG

3.5 Discussion

The addition of an imaging domain to self-assembling ELP nanoparticles to create a new nanoparticle based MRI contrast agent opens up numerous possibilities for its use as a potential biomarker system or as a theranostic platform. A distinct advantage of this system is the ability to seamlessly integrate any ELP-foldon construct as the base using molecular biology. The T_t or any other condition used to drive the stimuli can be optimized for potential use *in vivo* through amino acid substitution. Further addition of any peptide based targeting moiety can be accomplished in the same manner. This allows for the creation of any number of systems composed of entirely organic components, without the need for any post-translational modification. This eliminates the need for any excess conjugation steps or further chemistry being performed on the system in order to

add functionality. To our knowledge this is the first MRI active elastin-like polypeptide nanoparticle system reported in literature.

The first and most important part of this fusion was to ensure that both proteins retained their positive properties after the fusion takes place. The ELP retains its responsive behavior while the imaging domain retains the ability to effectively bind gadolinium. ELP constructs are defined by their transition temperature (T_t), which is a measure of the temperature at which the protein transitions from a soluble state below the T_t to an insoluble state above the T_t. The T_t of ELP-IMG is 31.7°C with or without bound gadolinium ions, compared to 34.5°C for ELP-foldon. Similarly when the construct was created without the foldon domain, the T_t was 40.8°C compared to 41.5°C for ELP_{40}. This is a good indication that the CA1.CD2 domain binding gadolinium does not interfere with ELP properties nor does the trimerizing foldon domain cause a loss of CA1.CD2 domain properties.

When Dynamic light scattering was performed on these samples it was shown that the ELP-IMG constructs forms stable micellar nanoparticles in non-physiologic conditions (low salt, high pH), which is indicative of previously seen activity from ELP-foldon constructs. The foldon domain at the C terminal of ELP carries a net negative charge and will act as a hydrophilic head group creating micelle structures with 3 hydrophobic ELP chains and a charged head group. We anticipated that the CA1.CD2 domain would not interfere with the activity of the ELP-foldon structure due to its similar architecture; stability across a range of pH's and net negative charge. In essence the CA1.CD2 positioned after the foldon domain acts an extension of the head group to encourage micelle formation. The results of dynamic light scattering showed that this was

the case as in conditions of low salt and high pH the fusion protein formed micelles with an average diameter of 31.65 ± 1.45 nm. In low salt conditions the charge on the head groups is sufficiently shielded in order to prevent aggregation and allow micelle formation to take place.

To use the micelles as a theranostic platform the micelles need to be stable in physiologic conditions i.e. high salt and neutral pH. A method to stabilize micelles into a single nancoparticle shape regardless of temperature, salt or solution conditions is through the use of crosslinking[42]. Various methods have proven to be effective for cross-linking micelles including dimethyl 3,3-dithiobispropionimidate (DTBP)[234], disulfide based cross-linkers[235] and glutaraldehyde[236]. Glutaraldehyde was chosen as the cross-linking agent since it is considered most effective at high pH values, in which the micelles form. After the crosslinking reaction took place the size of the micelles increased to 39.7 ± 4.8 nm with a broader distribution than non-crosslinked micelles. To be utilized in physiologic conditions dialysis into PBS dynamic took place after which light scattering revealed that the constructs had increased in size to about 82.5 ± 5.7 nm at 42°C which is approximately 2.5 times the size of non-cross-linked ELP-IMG constructs. The increased salt content may cause the construct to swell as the shielding on the headgroup decreases and the headgroup decreases in size. This was further confirmed by the addition of salt to crosslinked samples and monitoring particle size changes (Figure 3.7). The strength and stability of the crosslink reaction was also shown through the shrinking and swelling behavior of the particles as well as monitoring their stability over the course of 44 days. It is possible that due to the nature of glutaraldehyde cross-linking being non-specific head-groups are being cross-linked together creating nanoscale

aggregates of micelles rather than individual micelle structures. Further the crosslinking reaction causes a slight increase in diameter, indicating that multiple micelles may be being crosslinked together. This is consistent with the TEM image of the constructs in Figure 3.9. However, the strength and nature of the glutaraldehyde cross-linking is sufficient enough to prevent the structures from losing their nanoparticle structure and becoming completely soluble again.

Relaxometry measurements show that the ELP-IMG constructs display a *r1* relaxivity value of 35.4 $mM^{-1}s^{-1}$ for soluble monomers, 31.7 $mM^{-1}s^{-1}$ for soluble trimer constructs and 21.7 $mM^{-1}s^{-1}$ for cross-linked samples. These results are less than what is reported for the CA1.CD2 domain on its own, which is 117 $mM^{-1}s^{-1}$ however, they are still 5 times larger than that of Gd-DTPA and comparable to other micelle based contrast agents with Gd^{3+} chelators[237]. One possible explanation for the drop in relaxivity of the constructs is that the CA1.CD2 domains become crowded when they form after the foldon headgroups in micelle structures. When Gd^{3+} ions are closely packed together as they would be in this situation it brings two paramagnetic centers into close proximity[238], which in turn causes, a reduction of proton relaxivity (*r1*) by increasing the transverse electronic relaxivity[12]. To understand this further, on a per volume basis the number of trimers per micelle can be calculated using the molecular weight of trimer as 93,600 g/mol, a density of $1.2*10^3$ g/L and the radius of an ELP-IMG micelle as 16nm. The volume of an ELP-IMG trimer is $363.15nm^3$. The volume of ELP-IMG micelle can be calculated using $4//3\pi r^3$, giving a value of 17,157 nm^3. The number of trimers per micelle can then be calculated as 47 and with 3 gadolinium binding sites per headgroup, it is a total of 141 gadolinium binding sites per micelle.

In the cross-linked constructs the relaxivity decreases further. This can most likely be explained by the non-specific nature of using glutaraldehyde cross-linking for this process. The crosslinking process brings multiple headgroups closer together. Thus if multiple CA1.CD2 domains are being cross-linked together or packed on top of each other in the cross-linked structure the proximity of paramagnetic centers would be even closer. Compounding this would be a possible loss of availability to bulk water in the particle, which would reduce the ability of water exchange to take place for the CA1.CD2 domain as compared to the water available in the soluble constructs. When these are crosslinked the number of gadolinium binding sites per headgroup most likely increases even further potentially explaining the crowding condition. In order to optimize the relaxivity properties of the construct different ELP architectures, including mixtures of linear and trimer structures need to be investigated to attempt to reduce headgroup crowding

3.6 Conclusion

Taken as a whole, this fusion protein represents a promising wholly peptide based MRI contrast agent with potential for use in *in vivo* applications and as a future platform for theranostic systems. The system exists as a nano scaled structure in physiologic conditions that is dependent only on the temperature of solution to drive the transition. Diagnostic imaging in MRI is provided by the fusion of the CA1.CD2 domain, which provides positive contrast in *T1* weighted imaging at low gadolinium concentrations. Further expansion or modification of the construct is made possible through simple molecular biology procedures eliminating the need for post-translational modification.

CHAPTER IV

ACTIVE TARGETING EFFECTS OF THERANOSTIC NANOPARTICLES OF ELASTIN-LIKE POLYPEPTIDES

4.1. Abstract

The addition of active targeting to a theranostic protein system based nanoparticle system, which is capable of MRI contrast and disease state targeting specificity is described. This theranostic system is composed of nanoparticles of the protein-based polymer elastin-like polypeptide. We previously described the development of nanoparticle contrast agents based on the fusion of these particles with a MRI binding domain. The system has been further enhanced to provide specific targeting through the addition of the gastrin-release peptide decorated on the outside of the nanoparticles. The construct displays relaxivity that is approximately four times higher than current clinical contrast agents and the contrast agent provides enhancement in cell lines in a short time frame. Being entirely protein based and highly amenable to alteration, this platform serves as an excellent candidate for soft matter theranostic systems.

4.2. Introduction

Theranostics is a revolutionary new field of research that aims to combine both therapeutic and diagnostic imaging components into a single nanoparticle formulation[218]. Eventually formulations of this nature will help to create a future of personalized medicine, where treatments are designed to meet the specific needs and can be tailored to the specific response of individual patients[6]. Due to the variability in response for each patient to a therapeutic formulation, this concept may help to increase the efficacy of cancer treatment. The use of theranostic nanoparticles decorated with targeting elements and molecular imaging can lead to site specific treatments and positive recognition of the interactions[111]. This approach has multi-fold benefits, which include individualized dose response recognition, real-time monitoring of the response to combinatorial treatments and the possible creation of a new class of biomarkers for recognition of phenotypes.

Nanoparticles are vital to the success of creating theranostic systems and can be composed of inorganic or organic components including polymers[239], lipids[39], dendrimers[41] and magnetic iron oxide[144]. In the case of cancer cells, the size and shape of nanoparticles offer great advantages in their ability to localize to these cells more so than to normal cells through the enhanced permeability and retention effect (EPR)[67] and a general method known as passive targeting. This strategy has been shown to be successful in demonstrating a level of accumulation of nanoparticles at the target site. The EPR effect is limited by the poor vascularization of large tumors as well an insufficient accumulation of nanoparticles to achieve diagnostic imaging[240].

These limitations can be overcome through the use of active targeting, which involves the attachment of targeting ligands or peptides to the surface of the

nanoparticles[77]. The targeting ligands have high affinity for various receptors or antigens present on the cell surface. When the targeted particles interact with these receptors, binding occurs through ligand-receptor interactions that can lead to receptor-mediated endocytosis and localization of the nanoparticle inside the tumor[81]. In order for active targeting to be successful the receptors must be over-expressed on the cell surface and should be evenly distributed to ensure the whole surface has a chance to experience the targeted nanoparticle[241]. The gastrin release peptide targeting ligand is a bombesin analogue used for prostate cancer specific targeting. This peptide targets to the gastrin-release peptide receptor (GRPR) which is a G-protein coupled receptor[106] and is over-expressed on many types of cancers including pancreas[106], breast[107], and prostate[108]. A recent study found that GRPR was highly over-expressed in lower grade prostate cancer tumors, indicating that the GRPR is a potential target for early detection using theranostic nanoparticles[81]. Prostate cancer is the second most highly diagnosed cancer in men and the second leading cause of cancer related death[1]. If prostate cancer becomes too advanced, it will reach a state where it is not treatable known as prostate resistant cancer (PRC), thus early detection is critical[96].

The use of magnetic resonance imaging (MRI) as the imaging modality for this theranostic system is desirable due to the fact that it is a non-invasive technique, high anatomical contrast and high spatial resolution[242]. When utilized for the purpose of disease detection and diagnosis of cancer states, however, there is a lack of sufficient contrast between the cancerous state and the surrounding healthy tissue[219]. MRI contrast agents are used to overcome this limitation, with the majority being based on the lanthanide, gadolinium[243], which produces positive contrast images. Although contrast

agents are widespread in use, both in clinical and diagnostic practice, they have several drawbacks. These include a relatively low relaxivity on the order of 3-8 $mM^{-1}s^{-1}$, which leads to a large amount of contrast agent required to generate sufficient contrast[137]. Second, typical contrast agents are cleared rapidly from the vasculature through renal mechanisms, which lead to poor tissue retention and the need for repeated dosages. Using nanoparticle based contrast agents has shown the ability to overcome these limitations mainly through an increase in rotational correlation time which increases the molecular tumbling rate and increases with increasing molecular weight[132]. Further combing nanoparticle based MRI with active targeting strategies allows for specific targeting and imaging of a disease state with enhanced contrast accumulation[244].

We have previously reported the design and characterization of elastin-like polypeptide (ELP) based micelles[193]. These nanoparticles are environmentally responsive and form with the aid of a negatively charged head group. ELPs are a genetically encoded responsive biopolymer based on the repetitive pentapeptide sequence VPGXG[161]. The X position is typically valine, but is substitutable for any of the amino acids except for proline, which makes for a limitless number of combinations. The most desirable feature of ELPs is their transition temperature (T_t) behavior where in an increase in the temperature of solution causes the ELP to change from a soluble state to an insoluble state where they aggregate into coacervates[245]. This behavior is rapid, reversible and able to altered in many ways including chain length and weight of the ELP[199], the composition of the guest residue[200] and solute conditions[246], giving a wide range of options for tuning the response of the protein to different conditions. As the basis for a theranostic system, the combination of tunable responsive behavior, control over composition, size, and

charge along with generally biocompatible behavior make ELPs an excellent material choice.

Fusion with the protein based MRI contrast agent CA1.CD2 was successfully achieved, and described in previous chapters. This cross-linked nanoparticle system displayed a relaxivity approximately five times that of clinical contrast agents, and displayed tolerance to being incubated with human serum as well as with zinc indicating stability of gadolinium binding. New modifications to the system include the addition of active targeting elements, through use of the gastrin release peptide c terminal fragment. This peptide was added to the system using common molecular biology techniques, and included a flexible spacer element between the headgroups and the targeting peptide. After expression and purification of the protein the contrast agent properties were examined, and the targeting efficacy of the modified ELP nanoparticles was investigated in three cancer cell lines. This system is the first ELP based theranostic nanoparticle reported in literature and is a promising candidate for use in many applications.

4.3. Materials and Methods

4.3.1. Gene Design and preparation

The genes that encode the ELP-THO structure ($GVGVP_{40}$-foldon-CA1.CD2-Spacer-GRP) were synthesized as previously reported. To modify the structure of ELP-foldon-CA1.CD2 to allow for addition of gastrin release peptide receptor a new set of oligonucleotides were created, as represented in Table 1, which includes a flexible spacer between the head-groups and targeting elements. The amino acid sequence, which

contains the spacer and the targeting element, is represented by:

GPGVGWTSTGPQSSNTGNPSTSGQNNVPGNHWAVGHLM

DNA Sequence	Primer Name
TATGGGCCACGGCGTGGGTGGGAATCACTGGGCAGTGGGACACTTG ATGTGAGCCCGGTGGGC	**GRP Forward**
CACCGGGCTCACATCAAGTGTCCCACTGCCCAGTGATTCCCACCCAC GCCGTGGCCCA	**GRP Reverse**
TATGGGCCACGGCGTGGGTTGGACCTCTACTGGCCCGCAATCCTCTA ACACTGGCAATCCGTCTACCTCTGGTCAAAATAACGTGCCGGGC	**Spacer Forward**
CGGCACGTTATTTTGACCAGAGGTAGACGGATTGCCAGTGTTAGAG GATTGCGGGCCAGTAGAGGTCCAACCCACGCCGTGGCCCA	**Spacer Reverse**

Table 4.1. Oligonucleotides used to create ELP-THO construct. Representation of oligonucleotides used to encode the spacer and gastrin release peptide receptor fragment.

4.3.2. Protein expression, purification, and characterization

Starter cultures were prepared from frozen stocks in 50 ml TB media supplement with 100 mg/L ampicillin at 37°C. The starter cultures were then added to 1 L of TB medium and shaken at 300 rpm and 37°C. OD_{600} readings were taken until the mixture reached a level between 0.9 and 1.0 at which time 240 mg of IPTG was added for induction. After shaking for a time of 5 hours the cells were collected by centrifugation at 9000xg for 30 minutes at 4°C. The cells were then lysed after being re-suspended in 30 ml of PBS using a sonicator. The soluble and insoluble fractions were separated by

centrifugation at 4°C and 27000xg. The protein was determined to be in the insoluble fraction in our previous study, which required the need for denaturation. The insoluble fraction from the first cold spin was re-suspended in 8M urea and sat at 4°C for at least 6 hours and subsequently dialyzed against 4 M urea at 4°C overnight, followed by dialysis against 2 M urea at 4°C overnight. Dialysis then took place against water three times for at least 2 hours followed by centrifugation at 4°C and 27000xg. The soluble portion from this centrifugation contained the final protein, which then was dialyzed against water at 4°C for at least 24 hours to remove any residual salts from the denaturation process.

Protein purity, trimer formation and molecular weight confirmation was performed using SDS-PAGE with 4-20% gradient Tris-HEPES-SDS gel. Molar concentrations of the purified proteins were determined based on calculated extinction coefficients[231] and absorbance at 280 nm measured on a Biomate 3 (Thermo Scientific).

The transition temperature of the fusion protein was determined by measuring the UV-absorbance of solutions at 350 nm on a Shimadzu 1800 UV-vis spectrophotometer with an attached temperature control cell. Particle sizing was performed on a 90 plus Brookhaven particle size analyzer (Brookhaven Instruments). This unit is a fixed angle dynamic light scattering system with a Peltier temperature control system. Samples were made as 25 μM solutions in PBS at varying pH conditions. The solutions were filtered using a 0.22 μm filter (Millipore) and loaded into quartz cuvettes and the pH was adjusted through the addition of filtered 10 N NaOH. Measurements were performed in triplicate and made in 2-minute long runs. The results were analyzed by the BIC software, which utilized a non-negatively constrained least squares algorithm

(Brookhaven Instruments) and were reported as mean diameter of multimodal size distribution (MSD).

For crosslinking reactions protein samples of varying concentrations were diluted in filtered water with the pH adjusted to 10.2-10.4 using 10 N NaOH. Stir bars were added to the sample and they were heated to 55°C with constant stirring for 1 hour. After 1 hour pre-warmed 10% glutaraldehyde (~2 µl) was added to the solution to facilitate cross-linking of the micelles. Samples were kept in this state for at least 18 hours after which they were filtered using a .22 µM filter (Millipore). Samples were then dialyzed using 1000 Da MWCO float-a-lyzer dialysis tubes (Spectra-Por) against PBS overnight. Particle size measurements of the cross-linked micelles were then analyzed as described.

Transmission electron microscopy (TEM) took place on FEI tecna G2 twin instrument on crosslinked protein samples in PBS at room temperature.

4.3.3. MRI imaging properties and characterization

Gadolinium chloride in citrate buffer was added to cross-linked protein samples in appropriate molar concentrations with constant stirring overnight. Samples were then dialyzed at 4°C against PBS for at least 6 hours to remove any potential excess Gd^{3+} and tested using the xylenol orange[212] and Arsenazo III[210] assays to ensure there was no free gadolinium present. Confirmation of the amount of gadolinium bound to fusion protein samples was determined by inductively coupled plasma optical emission spectroscopy (ICP-OES) [Perkins-Elmer]. The samples were diluted 300 times in 2% nitric acid using rhenium as an internal standard and compared to calibration plots. Aliquots of varying concentrations of Gd^{3+} loaded fusion proteins were loaded into NMR tubes. The *T1*

values of the proteins were measured using a mini-spec Mq60 1.4 T 60 mHz analyzer (Bruker). Runs were performed at 40°C and 10 points of measurement were taken. MRI images were obtained on an Espree 1.5 T clinical scanner (Siemens). Samples were contained in NMR tubes containing at least 200 µl of sample and arranged asymmetrically in a plastic rack holder. Images were produced using a gradient echo sequence (TE = 5.12 ms, TR =150 ms, resolution matrix 512x336, 111 slices, slice thickness = 2 mm), and these images were collected and analyzed using OpenDicom viewer software.

4.3.4. Cell Culture and Passaging

Cancer cell lines were chosen based on their expression levels of gastrin release peptide receptor[108]. The three lines chosen were pC3 prostate cancer cells[247], U87 RFP glioblastoma[248], and H441 lung cancer[249]. The pC3 and H441 lines were ordered from ATCC and the U87 RFP glioblastoma cells were a gift from Dr. Joanne Belovich. All cells were grown in a sealed incubator at 37°C and 5% CO_2. U87 cells were grown in Eagle's minimum medium 10% FBS supplemented with 5 ml L glutamine (0.292 gm/L), 5 ml 100 x non-essential amino acids (10 mM concentration of each within the solution), 10 ml 1x HEPES buffer, 5 ml pen strep (100 I.U. /ml penicillin and 100 ug/ml streptomycin) and 0.5 ml of 250 mg/ml amphotericia-B. Prostate cancer cell line, pC3 (ATCC CRL-1435) was ordered from ATCC and grown in F-12K media with 10% FBS. H441 (ATCC HTB-174) lung cancer cells were ordered from ATCC and grown in RPMI-1640 media with 10% FBS. Cells were passaged when they reached 75-80% confluence. Standard passage protocols were applied and passage number was kept less than 8 before using a fresh culture of cells.

4.3.5. ELP Targeting Properties and Fluorescent Imaging

From a fresh passage of cells, total number of cells was counted. Once seeding density was determined for each well per plate to transfer into, an appropriate amount of cell suspension was added to each well and diluted with an appropriate amount of fresh media. Cells were left to grow on the plates and were checked after 24 hours to ensure that attachment took place. Once that was determined the media was aspirated and replaced with fresh media and left to sit for 1 hour after which, protein samples at appropriate concentrations were incubated with the cells. ELP's were labeled with Flourescein isothioctanate (FITC), using a labeling kit (Pierce) and following standard protocols. After incubation times were completed the media was aspirated from the wells and cells were washed 2 times with ice cold sterile PBS and removed. Following this cells were washed with ice cold 4% paraformaldehyde for 5 to 8 minutes, followed by washing one more times in ice cold PBS for minutes. Solution was removed and DAPI was added and allowed to sit for 5 minutes before filling well with PBS and beginning microscopy studies. An inverted fluorescent microscope (Zeiss Axiovert) was used for imaging localization of ELP's within the cells at wavelengths corresponding to FITC (588 nm) and DAPI (461 nm) or red for RFP proteins (615 nm). Images were collected and processed in ImageJ.

4.3.6. MR Imaging of cells

ELP-THO-Gd^{3+} at 4 different protein concentrations was incubated with PC3 cells for 4 hours. As controls both ELP-IMG-Gd^{3+} and $Gd^{3+}Cl$ in citrate buffer were incubated with the cells for the same time period. At the completion of incubation period, the cells were washed three times with ice-cold PBS and removed from their wells with

trypsin. After trypsinization of the cells, volumes of 500 µl were then transferred into micro-centrifuge tubes and spun down. The resulting pellets in solution were kept on ice and taken immediately for MR imaging.

4.4. Results

Protein Synthesis, Expression and Characterization

Expression of the protein was successful and produced yields between 80 and100 mg/ml per liter of culture. Results of SDS-PAGE gel show that the trimer structures were folding correctly and are represented in Figure 4.1.

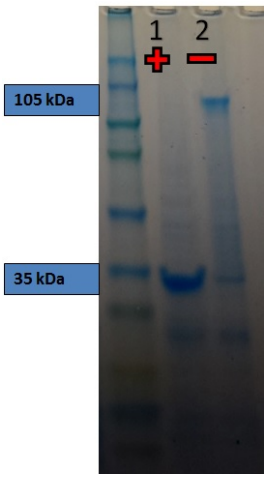

Figure 4.1. SDS-PAGE results of protein expression. Lane 2 represents the sample at room temperature with the trimer form present slightly above the 102 kDa marker and the monomeric form is represented by Lane 1 at 100°C with a molecular weight between the 31 and 38 kDa marker.

The amino acid sequence of the construct was confirmed by DNA sequencing (Cleveland Clinic genomics core) and was found to be MGH-$(GVGVP)_{40}$-GYIPEAPRDGQAYVRKDGEWVLLSTFL

GPGVGRDSGTVWGALGHGIELNIPNFQMTDDIDEVRWERGSTLVAEFKRKMKPF LKSGAFEIDANGDLDIKNLTRDDSGTYNVTVYSTNGTRILDKALDLRILE GPGVGWTSTGPQSSNTGNPSTSGQNNVPGNHWAVGHLM. The molecular weight of this construct in monomer form is calculated to be 35,267 daltons.

Transition temperatures (T_t) of protein samples were measured at a range of 25 protein concentrations in PBS, as well as a 25 μM protein concentration sample in varying salt conditions. At neutral pH and in PBS the transition temperature of the protein at a concentration of 25 μM is 32.4 °C. When gadolinium is added to the system the T_t is unchanged. Figure 4.2 represents a collection of T_t measurements taken as a function of concentration and salt in comparison to the same construct without targeting elements.

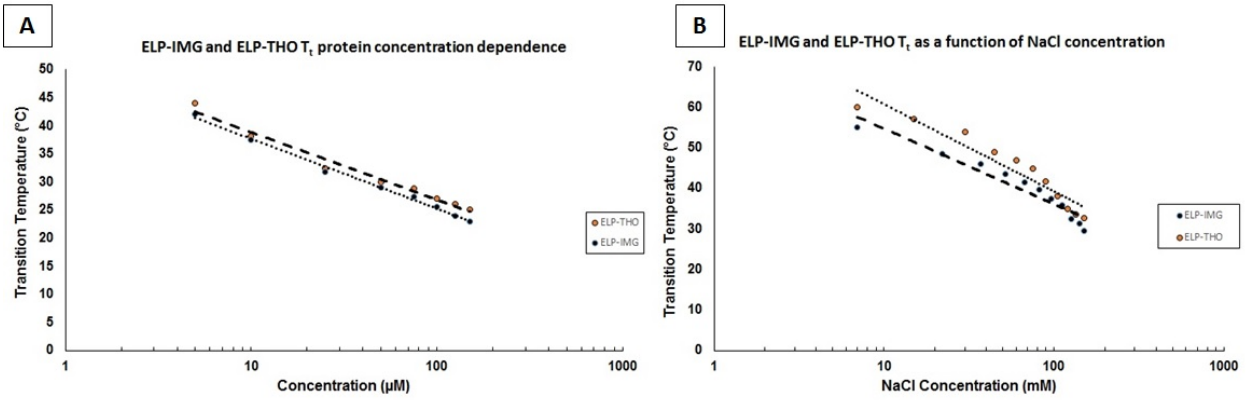

Figure 4.2. Transition temperature measurements as compared to ELP-IMG. Comparison of T_t values between ELP-THO and ELP-IMG: A) As a function of protein concentration B) As a function of NaCl concentration. Values of the two constructs are comparable indicating insignificant change in protein character after addition of targeting elements.

When dynamic light scattering was performed on the samples the self-assembly of micelles was confirmed. In micelle forming conditions (salt <30 mM pH 10.2-10.4), the constructs self-assemble into micelles above T_t with an average diameter of 37.7 ± 2.9 nm, and is comparable to previous iterations of the constructs (Figure 4.3c). After cross-linking the nanoparticles have an average diameter of 44 ± 3.8 nm with a slightly broader distribution. After dialysis in PBS overnight, the construct's particle diameter above the T_t increases to 70.8 ±1.8 nm, while below the T_t the particle diameter swells to a size of 94.8 ±5.8 nm and the constructs do not dissociate. These particle diameters are visible in Figure 4.3.

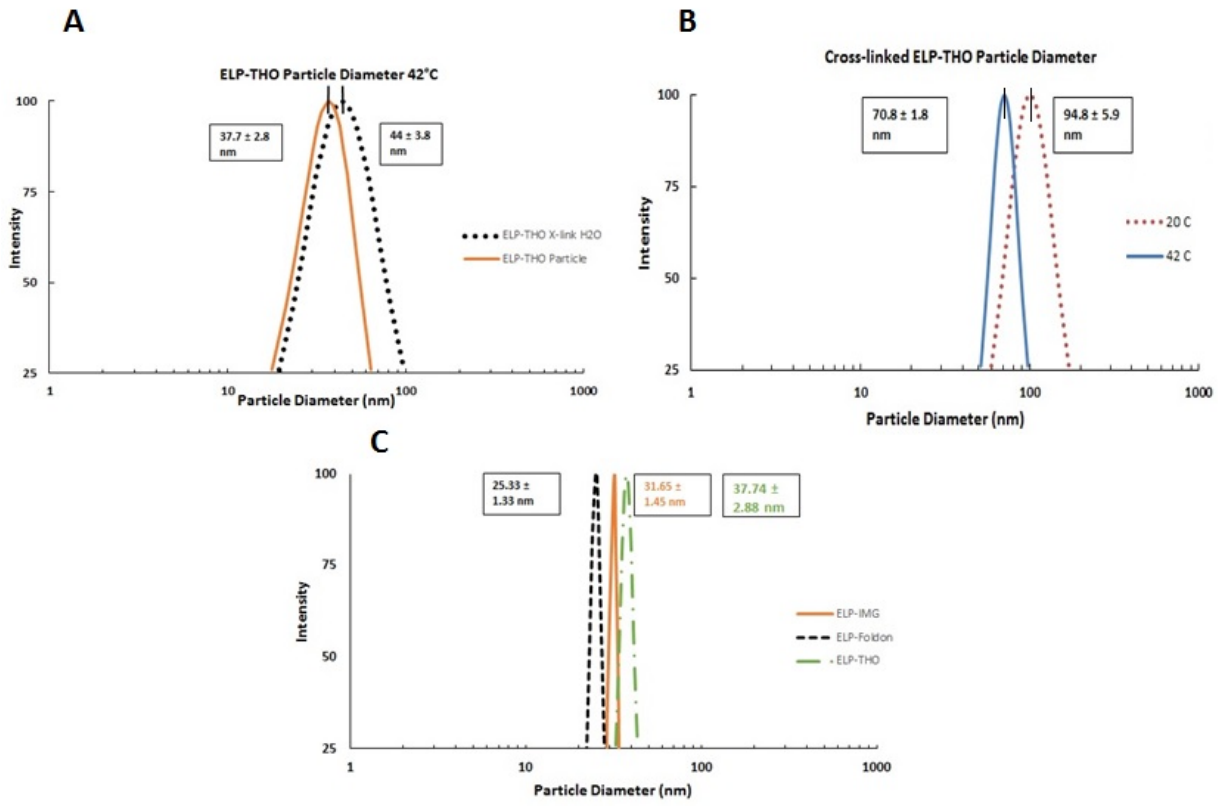

Figure 4.3. Particle size characterization of ELP-THO construct. A) Particle diameter in H_2O particle forming conditions and in reaction conditions. B) Cross-linked particle behavior above and below the T_t. C) Comparison of 3 ELP nanoparticle constructs

Using methods described previously, TEM images were acquired and further confirmed the nanoparticle scale of the crosslinked constructs as shown in figure 4.4.

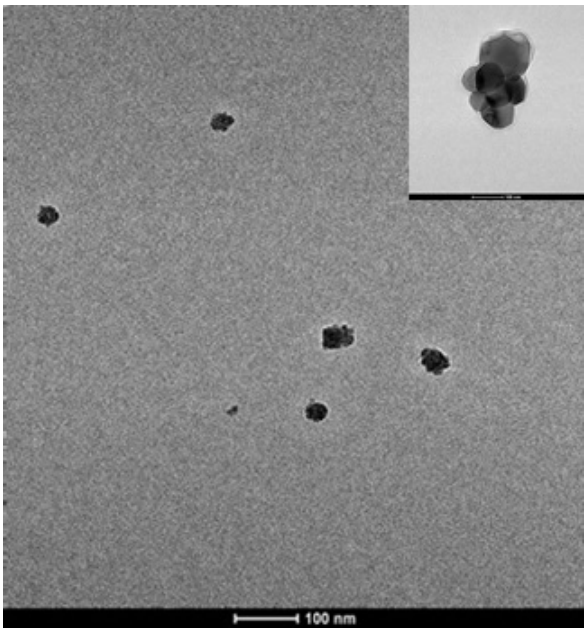

Figure 4.4. TEM images of ELP-THO. TEM images of crosslinked ELP-THO samples at room temperature in PBS.

Gadolinium addition, characterization, and imaging properties

Gadolinium chloride in citrate buffer (Acros) was added to cross-linked ELP-THO proteins in a drop-wise manner and allowed to stir overnight. It was found that a protein to gadolinium ratio of 1:1 was required to ensure the level of excess gadolinium present in the solution was minimal (<10%). ICP-OES analysis with the presence of the internal standard showed 95-100% recovery of internal standard, which indicates that the protein was not interfering with the detection of gadolinium. Xylenol orange and Arsenazo III assays were used to show that the amount of excess gadolinium present was < 10%. After addition and determination of bound gadolinium, relaxivity values were determined using a series of ELP-THO Gd^{3+} chelates at varying concentrations and 37°C. The results showed that the crosslinked constructs had a *r1* relaxivity of 15.17 $mM^{-1}s^{-1}$, which is slightly less than ELP-IMG (21.7 $mM^{-1}s^{-1}$).

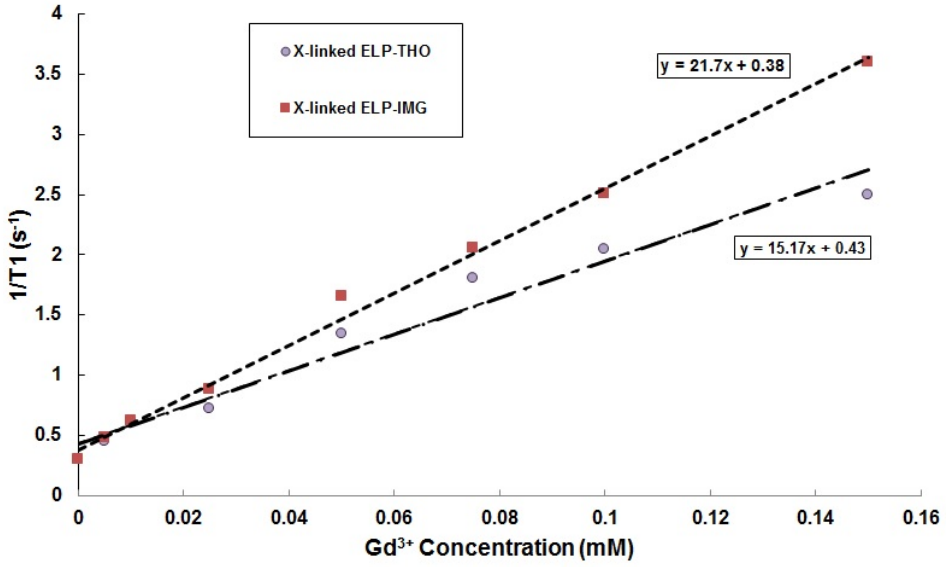

Figure 4.5. Relaxivity plot for ELP-THO construct compared to ELP-IMG. A linear relationship is observed between the Gd^{3+} concentration and 1/*T1* values, and when plotted as a line the slope gives the *r1* value of the construct as a whole.

MR Imaging

The results of the phantom experiment showed that the construct was displaying contrast in *T1* weighted imaging. Samples of increasing Gd^{3+} content (as measured by ICP-OES) displayed increasing contrast (Figure 4.6).

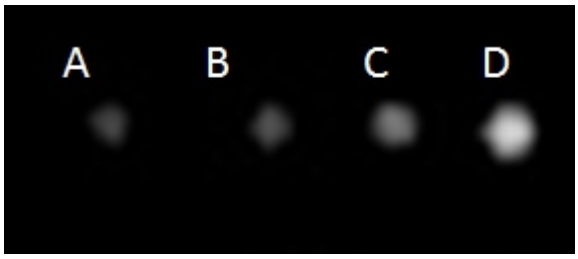

Figure 4.6. T1 weighted MR image of ELP-THO constructs. Phantom MR images of cross-linked ELP-THO-Gd^{3+} samples in PBS. Gd content was present in the samples as follows A) 0.01 mM B) 0.05 mM C) 0.1 mM D) 0.15 mM and *T1* weighted MR images were obtained using GRE sequence (TE = 5.12 ms, TR =150 ms, resolution matrix 512x336, 111 slices, slice thickness= 2 mm)

Active targeting properties of ELP-THO

Incubation of ELP-THO with gastrin release positive and negative cell lines and subsequent fluorescent microscopy imaging confirmed that the attachment of the gastrin release peptide targeting fragment allowed for active targeting of ELP constructs. As a negative control ELP without the targeting fragment also underwent the same procedure and was shown to have no interaction with the cell lines (Figures 4.7 and 4.8).

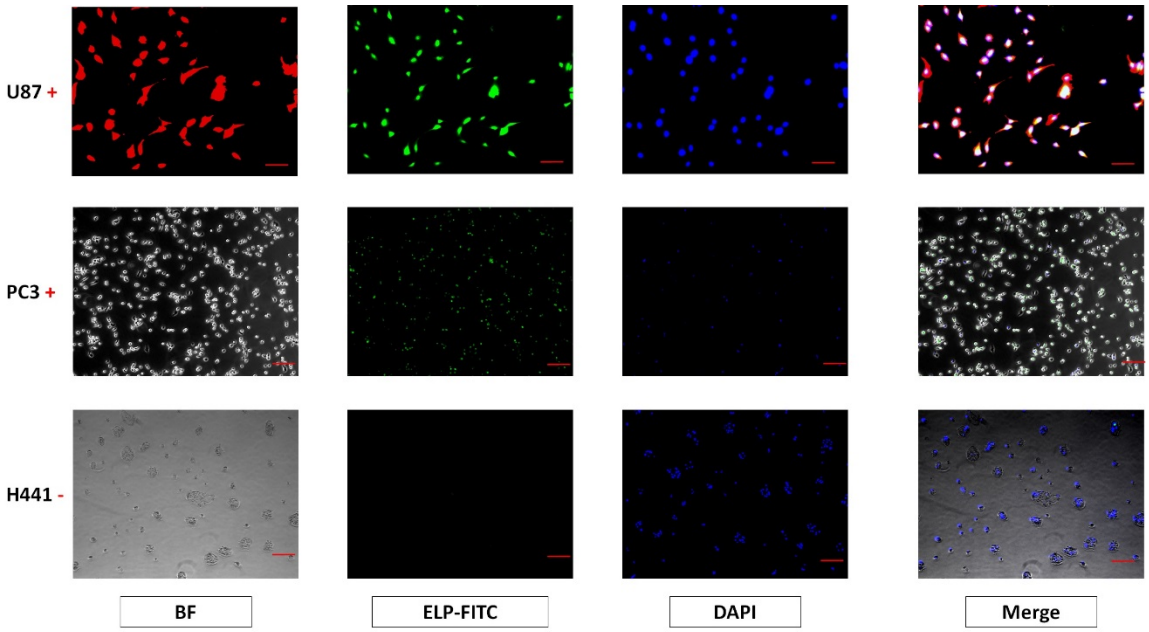

Figure 4.7. Immunohistochemistry panel of ELP-THO for 3 cell lines. Panel of three cell lines with either positive or negative GRPR content incubated with ELP-THO labeled with FITC. Images are taken at three wavelengths and merged to determine the nature of the targeting.

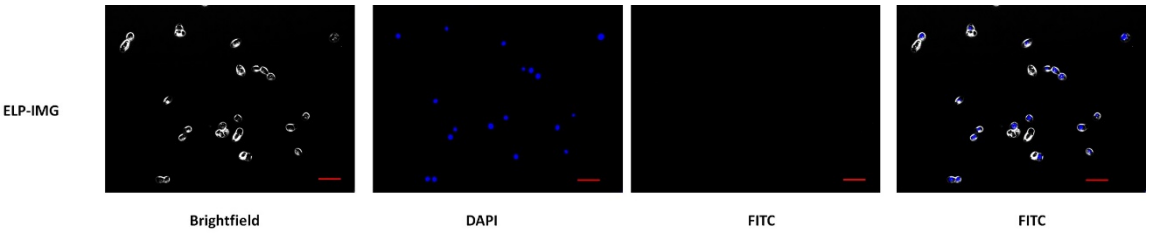

Figure 4.8. Immunohistochemistry panel of ELP-IMG as negative control. 3 cell lines negative control using ELP-IMG labeled with FITC incubated with PC3 cells.

Specific uptake and targeting of PC3 cells was investigated with different time points of incubation for 25 μM ELP-THO constructs labeled with FITC. Time points chosen were

30 minutes, 1.5 hour, 4 hours. Fluorescence microscopy indicated that the nanoparticles were targeting PC3 cells and were able to undergo interaction with cells in 30 minutes (Figure 4.9). MR Imaging of cells was performed to show that $Gd3^{+}$ loaded targeted constructs would display MRI contrast even after interaction with cells (Figure 4.10).

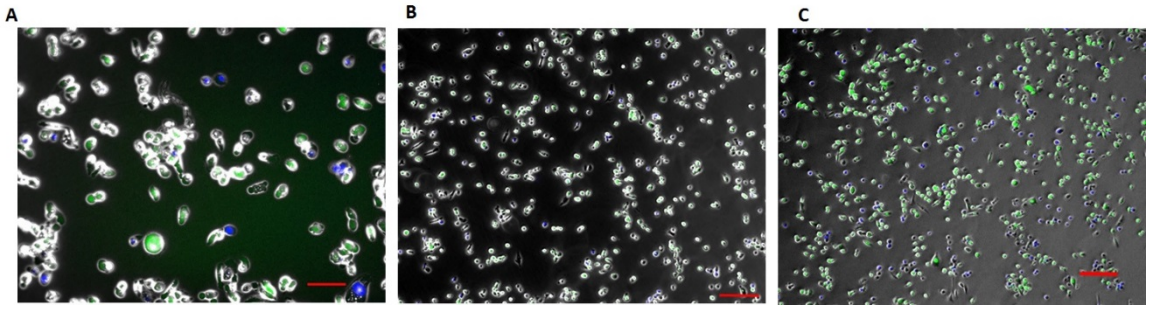

Figure 4.9. Uptake of ELP-THO-FITC in PC3 cells at 3 time points. PC3 cells (25,000 cells/well) incubated with 25μM ELP-THO at three time points a) 30 minutes b) 90 minutes c) 4 hours. The images were taken at three wavelengths and merged.

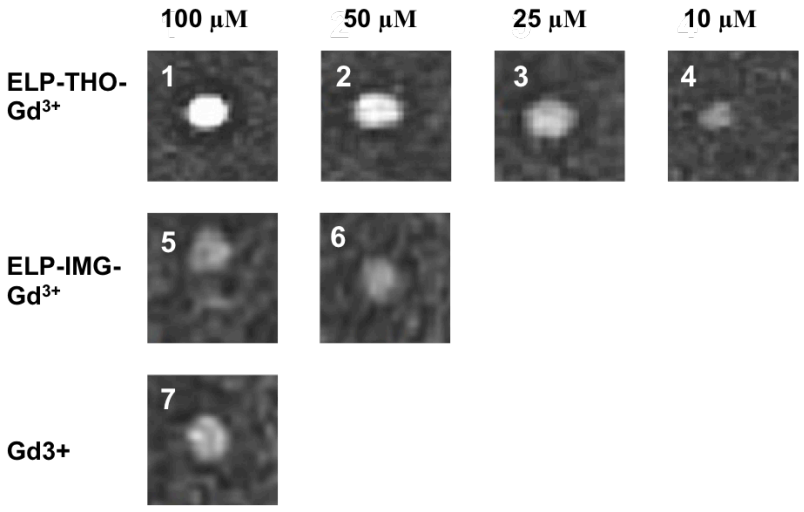

Figure 4.10. MR imaging of incubated cell pellets**.** PC3 cells at a density of 80,000 cells/well were cultured. ELP-THO Gd^{3+} was incubated at four concentrations (**1-4**) with the cells for 4 hours, followed by harvesting and imaging. As controls Gd^{3+} only at a concentration of 100 μM was incubated with cells (**7**) as well as the protein construct without targeting elements (**5-6**).

Cytoxicity assays

The results of the live/dead assay showed that ELP constructs displayed minimal toxic effects on PC3 cells while constructs with excess GTA and Gd^{3+} provided a higher level of toxicity. DMSO was used as a control to provide a majority of cells as dead while one well was left completely alive.

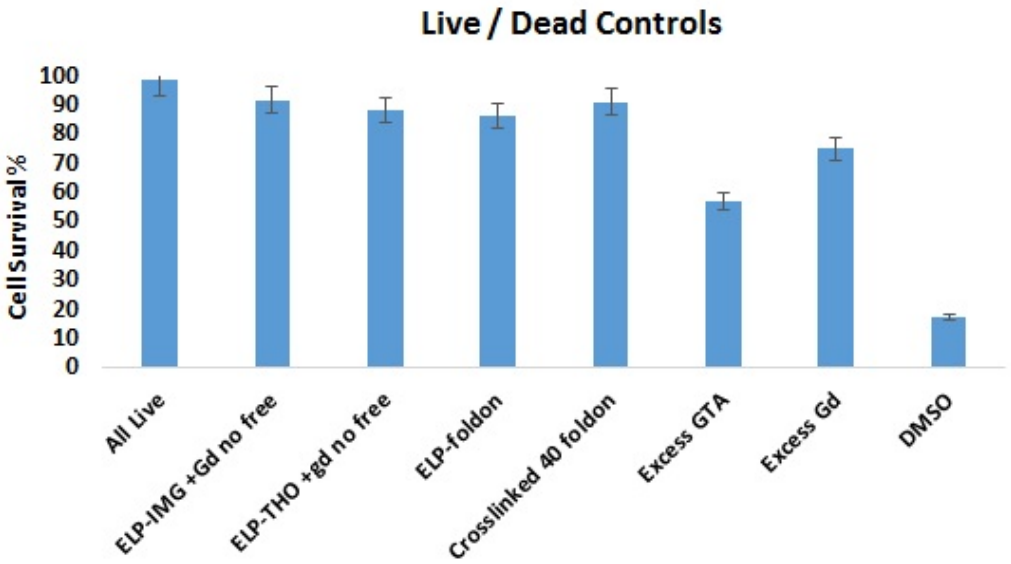

Figure 4.11. Live / Dead controls cytotoxicity %. Results of a series of controls to determine cell viability using a live / dead assay, which shows that ELP constructs inherently display minimal toxic effects on cells.

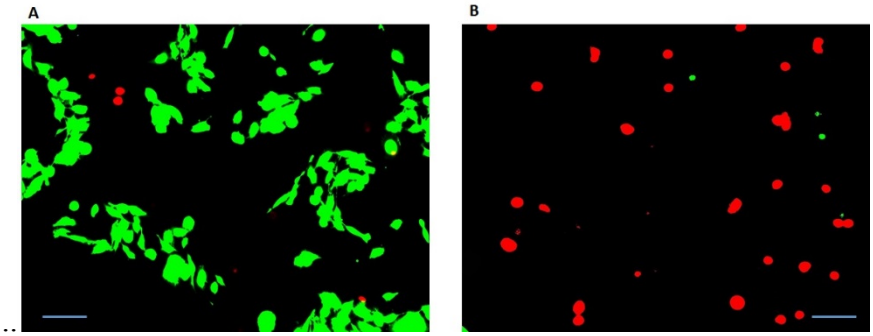

Figure 4.12. Live / Dead control A) ELP-THO with Gd^{3+} B) DMSO control.

The live / dead assay were performed as function of ELP concentration in samples of both PC3 cells, and U87 cells. The results showed that as ELP concentration increased the toxic effects remained minimal (Figure 4.13).

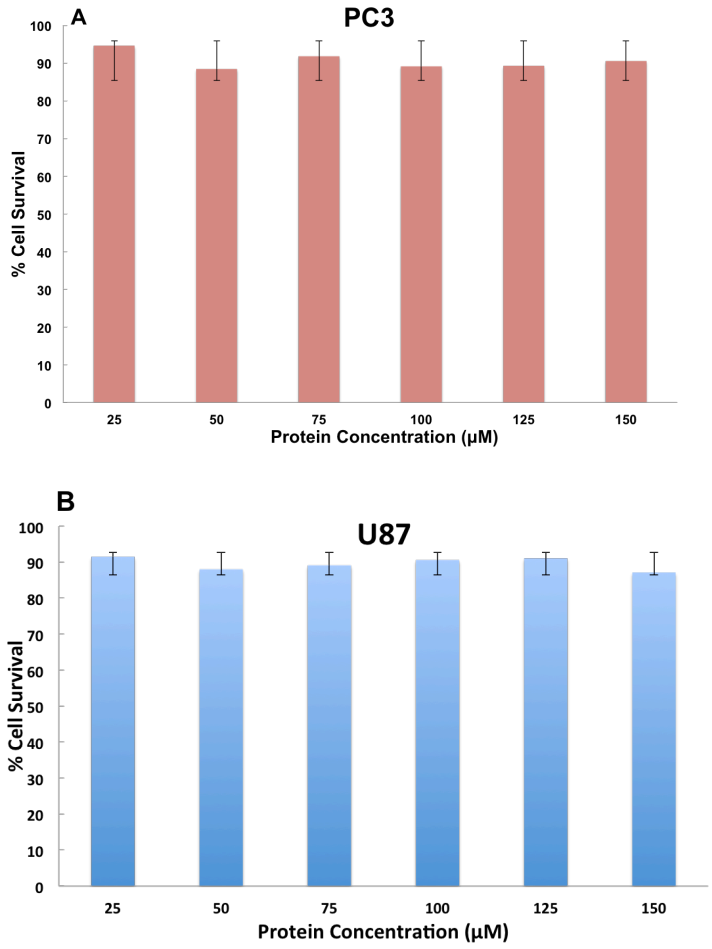

Figure 4.13. Live / Dead as a function of protein concentration. A) ELP-THO at protein concentrations from 25-150 µM incubated with PC3 cells. B) ELP-THO at protein concentrations from 25-150 µM incubated with U87 cells.

4.5. Discussion

The addition of targeting elements to MRI active nanoparticles of elastin-like polypeptides (ELP-IMG) is the first step to transforming the previously described system into a theranostic nanoparticle. These targeting peptides allow for disease state specific interaction between ELP nanoparticles and receptor positive cell lines.

After the addition of the targeting domains, it was important to determine the changes on the ELP properties. Transition temperature (T_t) behavior was characterized and compared to ELP-IMG. The T_t was found to be 32.4°C at 25 μM in PBS which is comparable to previous results. Further over a series of protein concentrations and salt concentrations the construct behaved in an expected manner. Also, with the addition of gadolinium, there was not an appreciable change in the T_t. This is a strong indication the addition of the spacing element and targeting peptide has no adverse effect on the ELP properties. When samples were prepared in micelle forming conditions (low salt, high pH) micelle self-assembly took place as expected and is comparable to both ELP-foldon[193] and ELP-IMG with an average diameter of 37.7 ± 2.8 nm. Cross-linking of the micelles was undertaken to stabilize the particles and prevent dissociation of the micelles in physiologic conditions. Another benefit of crosslinking the ELP-THO with glutaraldehyde (GTA) is that GTA has been shown to reduce drug burst release levels, reduce release rates and increase the time it takes for total drug release to occur[174]. After crosslinking took place in GTA the diameter of the constructs increased slightly, which can be explained by the non-specific nature of glutaraldehyde, which utilizes free amines for crosslinking[250]. Free amines are located on the N-terminal amines inside the core of the micelles; however, others exist on the headgroups, which may lead to the crosslinking

of individual micelles together to form aggregates. This behavior is clear from the TEM image in Figure 4.4. After dialysis into PBS, the diameter of the constructs increased approximately 200%. This can be explained by extra salt content that causes a decrease in the shielding on the headgroups. This decreased shielding causes the headgroups to become smaller while the length of the chains in the ELP core become extended[194]. The extent of the crosslinking through glutaraldehyde interacting with amines prevents the construct from dissociating as the temperature is dropped below the T_t. Instead the nanoparticles swell, to allow for the influx of water into the core that would typically be associated with soluble ELP. This swollen state, which only exists with the crosslinked proteins, has a diameter of 94.8 ±5.9 nm with a relatively broad distribution. When the temperature is raised above the T_t the diameter of the crosslinked nanoparticles collapses to a diameter of 70.8 ±1.8 nm. This can be described as the water leaving the core of the micelles as the ELP goes from a soluble to an insoluble state, but in this case the nanoparticle shape remains, with less water located in the core. This shrinking and swelling behavior can potentially be exploited in many ways for theranostic applications, with the transition being only dependent upon temperature change.

The next step of characterizing the ELP-THO crosslinked nanoparticle was to determine its properties as a contrast agent. Relaxometry was used to determine the value of the relaxivity at various Gd^{3+} concentrations and compared to ELP-IMG. The measurements showed that the constructs had a relaxivity of 15.1 $mM^{-1}s^{-1}$, which is 75% of the value achieved for the ELP-IMG constructs without the targeting and spacing elements. The spacer and targeting elements can be preventing water access to the CA1.CD2 domain in order to allow for optimal interaction between the Gd^{3+} and the bulk

water. Further, due to the non-specific crosslinking from the glutaraldehyde multiple headgroups may be being crosslinked together and held in close proximity, which can reduce relaxivity. The TEM may lend credence to this idea, as the headgroups appear to be stacked on top of each other (Figure 4.4). Water exchange rates, however are still high due to the soluble nature of the ELP construct in solution. Gradient echo MRI images show that the construct does provide positive contrast in *T1* weighted imaging which is dependent on the concentration of gadolinium bound to the construct.

Incubation of the ELP-THO constructs with cancer cell lines with varying levels of gastrin release peptide receptor expression confirmed the specificity of the targeting mechanism. After an incubation periods of 30 minutes crosslinked ELP-THO samples appear to be interacting with the PC3 cells, while after a period of 1.5 hours non targeted ELP-IMG show no uptake into cells. Similar behavior was observed in the GRPR positive cell line U87, while GRPR negative cell line H441, showed no interaction with ELP-THO. These results are strong indicators of the efficacy of the targeting peptides, as well as the ability of the targeted protein to interact with the cell. When MR imaging was applied to collected cell pellets, there was an enhancement of contrast observed with an increase in protein and Gd^{3+} concentration. Cytotoxicity analysis showed that the ELP based protein constructs without therapeutic displayed minimal toxicity. A 10 fold molar excess of Gd^{3+} with ELP-THO showed an increase in cytotoxic effects as well as a larger increase in cytotoxic effects for the sample with 300 fold excess GTA. However, samples that contained no excess amounts of either component had minimal toxicity. This is to be expected as Gd^{3+} is only toxic to cells in very large doses[251], and both ELP[168] and CA1.CD2 domain[137] are considered biocompatible. Further when ELP-THO was

incubated without bound Gd^{3+} in varying concentrations, minimal cytotoxicity was observed.

4.6. Conclusion

The advantages of this system are numerous and clearly display that the ELP-THO construct has potential as a theranostic system. The system exists as a crosslinked nanoparticle that is responsive to changes in the temperature of the environment. The combination of self-assembly, imaging properties, and targeting specificity are presented and represent the basis of using this system for numerous applications. A further advantage of the system is that it is fully protein based which allows for easy modification of the construct dependent only upon utilization of molecular biology. Modifications that are possible include adding any peptide based targeting element, changing the ELP composition to change the mechanism of response or to be more sensitive to various therapeutic interactions.

CHAPTER V

MODIFICATION OF THE ARCHITECTURE OF ELP-IMG CONSTRUCTS: EFFECTS OF CHAIN LENGTH AND MIXTURES WITH ELP-FOLDON

5.1. Introduction

Through the use of molecular biology, modification of the previously described ELP-IMG gene is a relatively straightforward process. The idea of this brief study was to determine two things; the first being the effects of linear chain length without the foldon domain on the properties of ELP-IMG and the second being making mixtures of ELP-IMG and ELP-Foldon. The linear constructs were conceived to see if the foldon and subsequent micelle formation had any adverse effects on properties and effectiveness of CA1.CD2 domain. The mixtures were thought of as a solution to reduce headgroup crowding that has been observed in ELP-IMG and ELP-THO. This chapter will detail their development and characterization.

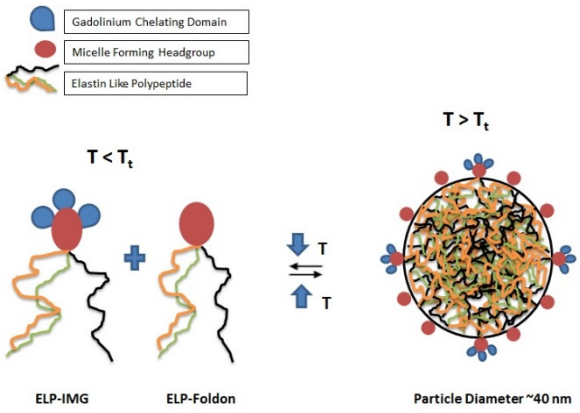

Figure 5.1. Schematic of mixtures of ELP-IMG and ELP-foldon.

5.2. Materials and Methods

The molecular biology method to create the linear constructs follows the methods previously described in other sections. The only difference was $(GVGVP)_{10}$, $(GVGVP)_{20}$, $(GVGVP)_{40}$ were double digested with NdeI and BglI and inserted into a pET20b-IMG vector that had been double digested with NdeI and PflMI. Mixtures were made based on a molar ratio which is what the percentages indicate, with only $(GVGVP)_{40}$-foldon and ELP-IMG being used. For example a 100 μM total protein concentration sample will have the following composition for different mixtures:

Composition: 2 ml 100 µM protein concentration	**ELP-IMG (430 µM stock)**	**ELP-Foldon (950 µM stock)**
10/90	10 µM 46.5 µl stock	90 µM 189.5 µl stock
30/70	30 µM 139.5 µl stock	70 µM 147.4 µl stock
50/50	50 µM 232.5 µl stock	50 µM 99.25 µl stock

Table 5.1. Ratios of protein stocks used to make mixtures.

Expression and purification of the linear constructs followed the same methods as described before, except for $(GVGVP)_{20}$-IMG and $(GVGVP)_{10}$-IMG, where NaCl was added to aid in the warm purification steps. At the conclusion of purification samples were dialyzed against H_2O for 24 hours to remove residual salts. Characterization including T_t measurements, dynamic light scattering and r1 time measurement proceeded as described earlier. *T1* weighted imaging was performed on a 1.5 T scanner (Siemens Espree) using Spin echo imaging with a TR of 500 ms, a TE of 12 ms. Slice thickness was 5 mm or 7 mM and the resolution matrix was 256x100.

5-3. Results

Mixture formation was successful in creating single entity constructs with mixed headgroups. The transition temperature (T_t) of the mixtures decreased with increasing ELP-IMG content with values for a 25 µM sample in PBS of: 10% ELP-IMG / 90%

ELP-Foldon having a value of 41.6°C, 30% ELP-IMG / 70% ELP-Foldon having a value of 38.7 °C and 50% ELP-IMG / 50% ELP-Foldon having a value of 36.2°C (Figure 5-2.).

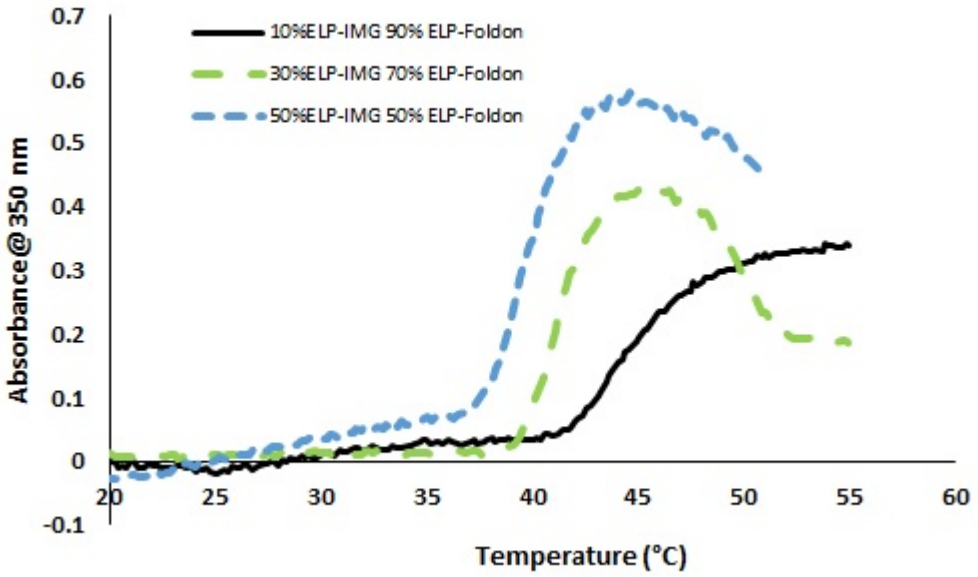

Figure 5.2. Transition Temperatures of mixtures. Transition temperature measurements for ELP-IMG / ELP-Foldon mixtures. Samples were made at 25 μM concentration in PBS.

Dynamic light scattering was applied to samples in particle forming conditions (low salt, high pH), post crosslinking in water and post crosslinking in PBS. The diameter of the particles in all conditions compares favorably to both ELP-foldon and ELP-IMG. A broadened distribution in crosslinked samples is observed however (Figure 5.3).

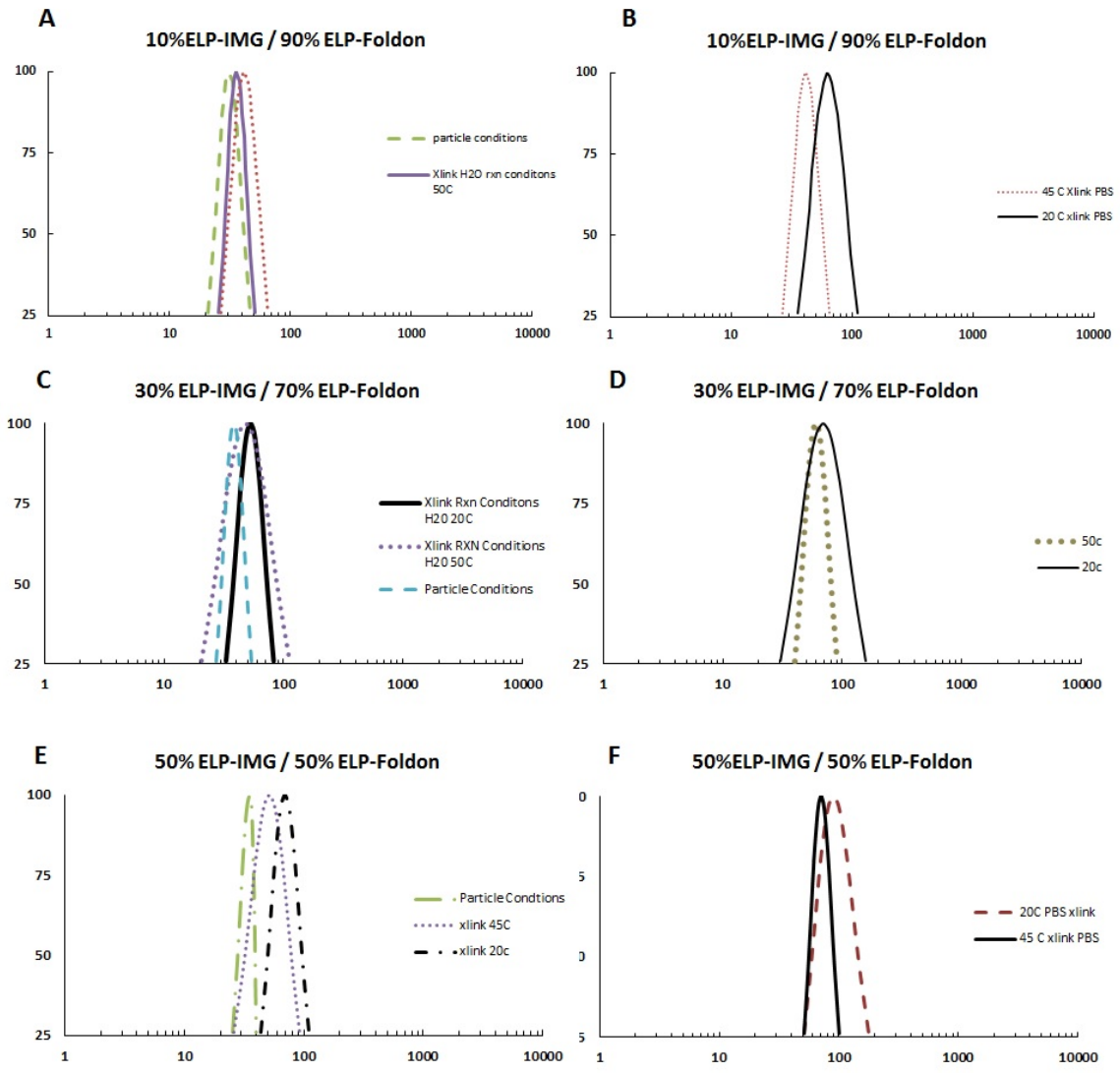

Figure 5.3. Dynamic light scattering of mixtures. Dynamic light scattering results for 3 mixtures, 10% 90%, 30% 70% and 50% 50% ratios. Single populations are observed across all conditions.

Upon measurement of the relaxivity values for crosslinked samples it was found that in mixtures with increasing ELP-IMG content, the relaxivity increased (50%>30%>10%) as would be expected. These values range from 16.6 $mM^{-1}s^{-1}$ to 12.9 $mM^{-1}s^{-1}$ (Figure 5-4), which are still at least 2.5 times more than Gd-DTPA in clinical

use. The advantage of the headgroup mixing however was as anticipated with a reduction in headgroup crowding leading to an enhancement of relaxivity values.

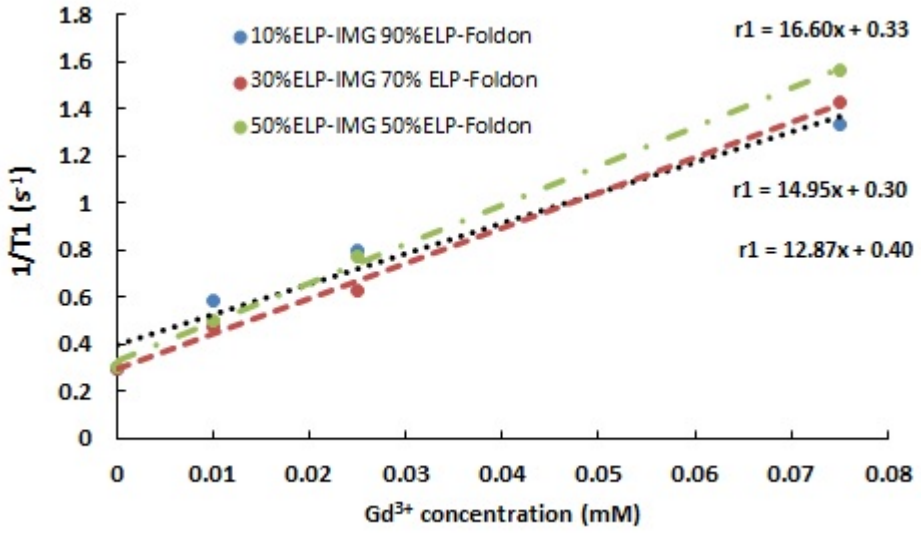

Figure 5.4. Relaxivity plots for mixtures of ELP-IMG and ELP-Foldon.

When the linear samples were measured as soluble constructs below their respective T_t $GVGVP_{40}$-IMG and $GVGVP_{20}$-IMG display relaxivities of 34.1 $mM^{-1}s^{-1}$ and 14.5 $mM^{-1}s^{-1}$, both of which are relatively high values in relation to clinical contrast agents (Figure 5-5). $GVGVP_{10}$-IMG was unable to be measured due to difficulty purifying the sample.

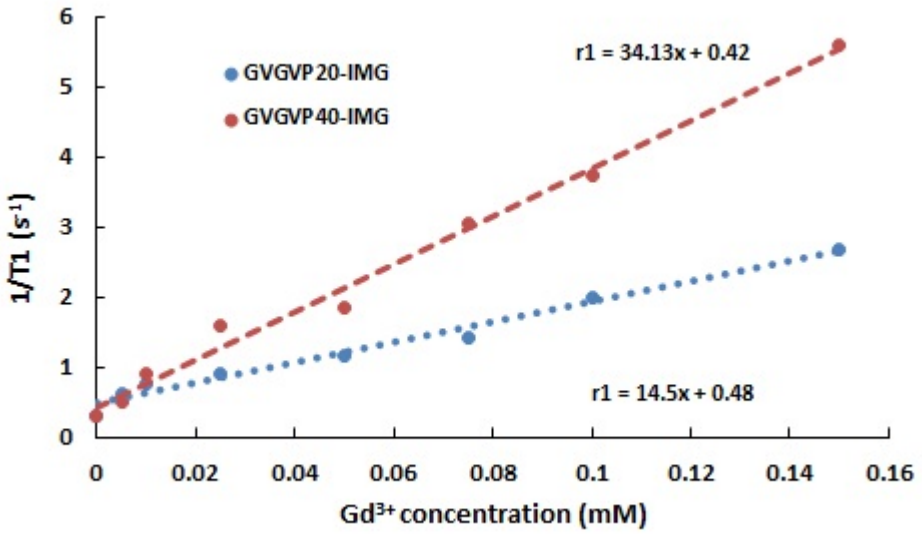

Figure 5-5: Relaxivity plots for linear ELP-IMG constructs.

Construct	Relaxivity ($mM^{-1}s^{-1}$)	T_t (°C)
$GVGVP_{40}$-IMG	34.13	40.1
$GVGVP_{20}$-IMG	14.5	55.5
10% ELP-IMG 90%ELP-Foldon	12.87	41.7
30% ELP-IMG 70%ELP-Foldon	14.95	38.6
50% ELP-IMG 50%ELP-Foldon	16.6	36.2

Table 5.2. Summary of relaxivity and T_t measured for modified constructs.

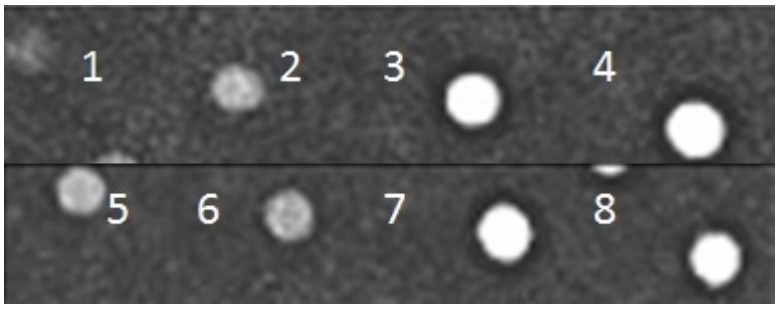

Figure 5.6. *In vitro* MRI imaging of mixtures. *T1* weighted MR image of linear ELP-IMG samples. The images are arranged in the following order (1) 0.01 mM Gd^{3+}-$GVGVP_{20}$-IMG (2) 0.025 mM Gd^{3+}- $GVGVP_{20}$-IMG (3) 0.05 mM Gd^{3+} $GVGVP_{20}$-IMG (4) 0.75 mM Gd^{3+} $GVGVP_{20}$-IMG (5) 0.01 mM Gd^{3+} $GVGVP_{40}$-IMG (6) 0.025 mM Gd^{3+} $GVGVP_{40}$-IMG (7) 0.05 mM Gd^{3+} $GVGVP_{40}$-IMG (8) 0.75 mM Gd^{3+} $GVGVP_{40}$-IMG

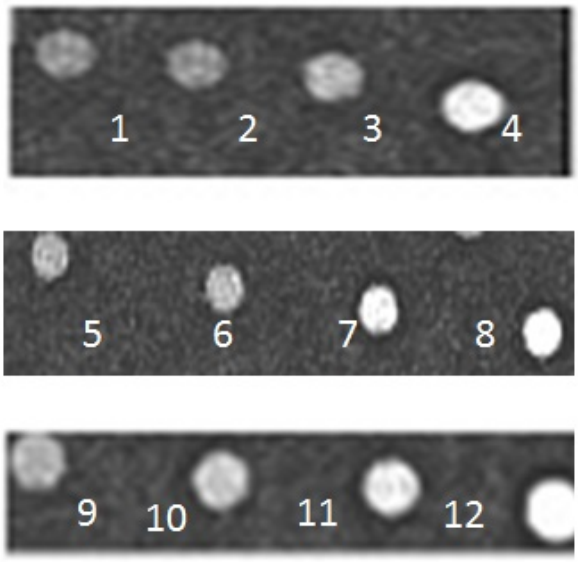

Figure 5.7. *In vitro* MRI imaging of linear constructs. *T1* weighted MR image of Mixtures of ELP-IMG and ELP-foldon samples. Samples 1-4 are 10% ELP-IMG / 90% ELP-foldon, samples 5-8 are 30% ELP-IMG / 70% ELP-foldon and samples 9-12 are 50% ELP-IMG / 50% ELP-foldon. The images are arranged in the following order (1) 0.01 mM Gd^{3+}, (2) 0.025 mM Gd^{3+}, (3) 0.05 mM Gd^{3+}, (4) 0.75 mM Gd^{3+}, (5) 0.01 mM Gd^{3+}, (6) 0.025 mM Gd^{3+}, (7) 0.05 mM Gd^{3+}, 8) 0.75 mM Gd^{3+}, 9) 0.01 mM Gd^{3+}, 10) 0.025 mM Gd^{3+}, (11) 0.05 mM Gd^{3+}, and (12) 0.75 mM Gd^{3+}

5.4 Discussion

Modification of the architecture of ELP-IMG constructs resulted in a series of new contrast agent constructs. There were a few important results from this experiment that may be able to shed light on the effects of ELP on contrast agent properties. The first motivation for the experiment was to attempt to solve what is believed to be headgroup crowding in crosslinked ELP-IMG nanoparticles. The strategy chosen was to attempt to

make mixtures of ELP-foldon and ELP-IMG to create a reduction in CA1.CD2 domain headgroups that would be present in each nanoparticle. On a positive note, these mixtures behaved in exactly the same manner as individual constructs, with T_t and particle formation that did not deviate from normal behavior. All mixture constructs however displayed relaxivity values that were less than ELP-IMG on its own, however the 50% / 50% mixture was higher than ELP-THO. The expected gains in relaxivity were not achieved through this mixture. Possible reasons include a drop in molecular weight of the mixtures, or a gain in mobility due to the headgroups no longer being cross-linked together. If multiple headgroups aren't being cross-linked together along with a reduction in molecular weight, there may be an increase in the molecular tumbling rate, which decreases relaxivity. Alternatively as theorized earlier headgroup crowding could still be occurring in the mixtures due to the choice of a non-specific crosslinking agent. These ideas would need to be investigated further if the mixtures were to continue as a viable project.

Linear constructs were synthesized to ensure that the foldon domain was not radically interfering with the activity of the fused CA1.CD2 domain. The results showed that the foldon domain does cause a loss of relaxivity (*r1* $GVGVP_{40}$-IMG > *r1* $GVGVP_{40}$-foldon-IMG) at the same chain length of ELP. This is most likely due to reasons mentioned previously. The linear ELP-IMG construct would be the version most similar to the CA1.CD2 domain alone, but in this case with a random coil polymer tail. Interesting when the tail length is cut in half ($GVGVP_{20}$) the relaxivity drops by 20 $mM^{-1}s^{-1}$, which is most likely explained by the drop in molecular weight and increase in rotational motion. The $GVGVP_{20}$-IMG construct is well below its T_t during the *T1*

measurement, which would mean it, exists as a random coil in solution, possibly explaining the drop in relaxivity. The $GVGVP_{40}$-IMG however construct has a T_t of 40.1 °C, which at the temperature of measurement for *T1* puts the construct right at its T_t, which could imply that the construct is going through the transition process during measurement and may be measured during the onset of turbidity. During this period there would be less random behavior of the ELP and a more ordered environment. *T1* weighted images confirmed that the constructs were displaying positive contrast in *T1* imaging and that the contrast increased in a linear fashion with increasing Gd^{3+} content (Figure 5.6 and Figure 5.7). This is important as the patterns are similar what was found for ELP-IMG and ELP-THO alone.

5.5 Conclusion

Being able to modify the construct in this manner allows for a number of possibilities to create mixed architectures that will still retain the positive properties of the designed protein. Although the mixtures did not enhance relaxivity due to perceived reduction of headgroup crowding, the mixtures still provide a positive route to attempt new ELP-IMG based constructs without having to completely redesign the architecture.

CHAPTER VI

CONCLUSION AND FUTURE DIRECTIONS

Utilizing elastin-like polypeptides as the base material for multifunctional theranostic nanoparticle systems has many distinct advantages. Starting with an entirely amino acid based composition has dual positive properties as the system is organic in nature and can then be modified and designed at the gene level through the use of molecular biology techniques in any applicable way. The responsive behavior can be exploited to drive the transitional behavior in response to various stimuli, which opens endless possibilities in the field of theranostics. The approach of this work was to utilize these properties to design a new theranostic nanoparticle system, composed entirely of organic components and needing no complex post-translational chemical modification.

Micelles of three-armed star elastin-like polypeptides were fused to a protein based MRI contrast agent in the first part of this study. The aim was to create a stable nanoparticle contrast agent composed of organic components that retained flexibility for modification. This aim was successful as the fusion of the two components produced a

stable crosslinked nanoparticle that was effective as a *T1* weighted MRI contrast agent in both particle and non-particle form that had relaxivity values 5 times that of clinical contrast agents. To demonstrate the flexibility of the system the architecture was modified and it was established that the system could undergo changes without loss of effectiveness of the positive properties.

This system was then modified through the addition of a short targeting peptide and spacing element that specifically targeted the gastrin release peptide receptor. When incubated with receptor positive cell lines the new construct showed targeting capabilities that were demonstrated by an enhanced amount of cellular uptake. Contrast agents incubated with these cell lines were able to introduce gadolinium into the cells, which was demonstrated by *T1* weighted imaging of cell pellets.

To enhance the system for the future the following recommendations are presented. 1) change the ELP guest residue position to create a stimulus responsive particle system. This could potentially enhance relaxivity as well enhance cytotoxicity through specific dissociation of the particles in certain conditions. 2) Introduce site-specific crosslinking to better control the morphology of the crosslinked nanoparticles. This can potentially enhance relaxivity by eliminating some of the non-specific crosslinking that currently takes place. 3) Establish a range of therapeutics and their partition coefficients in relation to changes in guest residue. This would create a library of ELP / therapeutic combinations that could potentially be used in any number of treatments. Along with the enhanced contrast agent properties these combinations would prove to be an ideal theranostic system.

This work demonstrated the ability to use micelles of ELPs as multifunctional nanoparticles for theranostic applications. Features demonstrated include self-assembling nanoparticle formation, MRI contrast, and active cancer cell targeting behavior. Taken as a whole this represents a platform that can be manipulated in endless ways to truly demonstrate the potential of elastin-like polypeptides.

BIBLIOGRAPHY

1. Siegel R, Ma J, Zou Z, Jemal A. Cancer statistics, 2014. *CA: A Cancer Journal for Clinicians*. 2014;64(1):9-29.

2. DeSantis CE, Lin CC, Mariotto AB, et al. Cancer treatment and survivorship statistics, 2014. *CA-Cancer J Clin*. 2014;64(4):252-271.

3. Sahoo S, Labhasetwar V. Nanotech approaches to delivery and imaging drug. *Drug Discov Today*. 2003;8(24):1112-1120.

4. Cheng Z, Al Zaki A, Hui JZ, Muzykantov VR, Tsourkas A. Multifunctional nanoparticles: Cost versus benefit of adding targeting and imaging capabilities. *Science*. 2012;338(6109):903-910.

5. Kelkar SS, Reineke TM. Theranostics: Combining imaging and therapy. *Bioconjug Chem*. 2011;22(10):1879-1903.

6. Ryu JH, Lee S, Son S, et al. Theranostic nanoparticles for future personalized medicine. *Journal of controlled release : official journal of the Controlled Release Society*. 2014;190:477-484.

7. Kalia M. Personalized oncology: Recent advances and future challenges. *Metab Clin Exp*. 2013;62, Supplement 1(0):S11-S14.

8. McGeough C, Bjourson A. Diagnostic, prognostic and theranostic genetic biomarkers for rheumatoid arthritis. *J Clin Cell Immuno*. 2012;6(002):1-5.

9. Gelderblom H, Verweij J, Nooter K, Sparreboom A. Cremophor EL: The drawbacks and advantages of vehicle selection for drug formulation. *Eur J Cancer*. 2001;37(13):1590-1598.

10. Cho K, Wang X, Nie S, Chen Z(, Shin DM. Therapeutic nanoparticles for drug delivery in cancer. *Clin Cancer Res*. 2008;14(5):1310-1316.

11. Allen T, Cullis P. Drug delivery systems: Entering the mainstream. *Science*. 2004;303(5665):1818-1822.

12. Davis ME, Chen Z, Shin DM. Nanoparticle therapeutics: An emerging treatment modality for cancer. *Nature Reviews Drug Discovery*. 2008;7(9):771-782.

13. Brannon-Peppas L, Blanchette J. Nanoparticle and targeted systems for cancer therapy. *Adv Drug Deliv Rev*. 2004;56(11):1649-1659.

14. Kamaly N, Xiao Z, Valencia PM, Radovic-Moreno AF, Farokhzad OC. Targeted polymeric therapeutic nanoparticles: Design, development and clinical translation. *Chem Soc Rev*. 2012;41(7):2971-3010.

15. Zhang S, Li J, Lykotrafitis G, Bao G, Suresh S. Size-dependent endocytosis of nanoparticles. *Adv Mater*. 2009;21(4):419-+.

16. Sahay G, Alakhova DY, Kabanov AV. Endocytosis of nanomedicines. *J Controlled Release*. 2010;145(3):182-195.

17. Gratton SEA, Ropp PA, Pohlhaus PD, et al. The effect of particle design on cellular internalization pathways. *Proc Natl Acad Sci U S A*. 2008;105(33):11613-11618.

18. Wang J, Byrne JD, Napier ME, DeSimone JM. More effective nanomedicines through particle design. *Small*. 2011;7(14):1919-1931.

19. Choi HS, Liu W, Misra P, et al. Renal clearance of quantum dots. *Nat Biotechnol*. 2007;25(10):1165-1170.

20. Moghimi SM, Szebeni J. Stealth liposomes and long circulating nanoparticles: Critical issues in pharmacokinetics, opsonization and protein-binding properties. *Prog Lipid Res*. 2003;42(6):463-478.

21. Torchilin VP. Micellar nanocarriers: Pharmaceutical perspectives. *Pharm Res*. 2007;24(1):1-16.

22. Geng Y, Dalhaimer P, Cai S, et al. Shape effects of filaments versus spherical particles in flow and drug delivery. *Nat Nanotechnol*. 2007;2(4):249-255.

23. Verma A, Stellacci F. Effect of surface properties on nanoparticle-cell interactions. *Small*. 2010;6(1):12-21.

24. Toy R, Bauer L, Hoimes C, Ghaghada KB, Karathanasis E. Targeted nanotechnology for cancer imaging. *Adv Drug Deliv Rev*. 2014;76:79-97.

25. Doshi N, Prabhakarpandian B, Rea-Ramsey A, Pant K, Sundaram S, Mitragotri S. Flow and adhesion of drug carriers in blood vessels depend on their shape: A study using model synthetic microvascular networks. *J Controlled Release*. 2010;146(2):196-200.

26. Decuzzi P, Godin B, Tanaka T, et al. Size and shape effects in the biodistribution of intravascularly injected particles. *J Controlled Release*. 2010;141(3):320-327.

27. Zhao F, Zhao Y, Liu Y, Chang X, Chen C, Zhao Y. Cellular uptake, intracellular trafficking, and cytotoxicity of nanomaterials. *Small*. 2011;7(10):1322-1337.

28. Wilhelm C, Billotey C, Roger J, Pons JN, Bacri JC, Gazeau F. Intracellular uptake of anionic superparamagnetic nanoparticles as a function of their surface coating. *Biomaterials*. 2003;24(6):1001-1011.

29. Dausend J, Musyanovych A, Dass M, et al. Uptake mechanism of oppositely charged fluorescent nanoparticles in HeLa cells. *Macromolecular Bioscience*. 2008;8(12):1135-1143.

30. Karmali PP, Simberg D. Interactions of nanoparticles with plasma proteins: Implication on clearance and toxicity of drug delivery systems. *Expert Opin Drug Deliv*. 2011;8(3):343-357.

31. Vonarbourg A, Passirani C, Saulnier P, Benoit JP. Parameters influencing the stealthiness of colloidal drug delivery systems. *Biomaterials*. 2006;27(24):4356-4373.

32. Veronese FM, Pasut G. PEGylation, successful approach to drug delivery. *Drug Discov Today*. 2005;10(21):1451-1458.

33. Malam Y, Loizidou M, Seifalian AM. Liposomes and nanoparticles: Nanosized vehicles for drug delivery in cancer. *Trends Pharmacol Sci*. 2009;30(11):592-599.

34. Agnihotri S, Mallikarjuna N, Aminabhavi T. Recent advances on chitosan-based micro- and nanoparticles in drug delivery. *J Controlled Release*. 2004;100(1):5-28.

35. Bala I, Hariharan S, Kumar M. PLGA nanoparticles in drug delivery: The state of the art. *Crit Rev Ther Drug Carrier Syst*. 2004;21(5):387-422.

36. Gu F, Zhang L, Teply BA, et al. Precise engineering of targeted nanoparticles by using self-assembled biointegrated block copolymers. *Proc Natl Acad Sci U S A*. 2008;105(7):2586-2591.

37. Soppimath K, Aminabhavi T, Kulkarni A, Rudzinski W. Biodegradable polymeric nanoparticles as drug delivery devices. *J Controlled Release*. 2001;70(1-2):1-20.

38. Noble GT, Stefanick JF, Ashley JD, Kiziltepe T, Bilgicer B. Ligand-targeted liposome design: Challenges and fundamental considerations. *Trends Biotechnol*. 2014;32(1):32-45.

39. Al-Jamal WT, Kostarelos K. Liposomes: From a clinically established drug delivery system to a nanoparticle platform for theranostic nanomedicine. *Acc Chem Res*. 2011;44(10):1094-1104.

40. Allen TM, Cullis PR. Liposomal drug delivery systems: From concept to clinical applications. *Adv Drug Deliv Rev*. 2013;65(1):36-48.

41. Astruc D, Boisselier E, Ornelas C. Dendrimers designed for functions: From physical, photophysical, and supramolecular properties to applications in sensing, catalysis, molecular electronics, photonics, and nanomedicine. *Chem Rev*. 2010;110(4):1857-1959.

42. Kaminskas LM, Boyd BJ, Porter CJH. Dendrimer pharmacokinetics: The effect of size, structure and surface characteristics on ADME properties. *Nanomedicine*. 2011;6(6):1063-1084.

43. Oerlemans C, Bult W, Bos M, Storm G, Nijsen JFW, Hennink WE. Polymeric micelles in anticancer therapy: Targeting, imaging and triggered release. *Pharm Res*. 2010;27(12):2569-2589.

44. Http://Www.doxil.com/.

45. Nagore E, Insa A, Sanmartin O. Antineoplastic therapy-induced palmar plantar erythrodysesthesia ('hand-foot') syndrome. incidence, recognition and management. *American journal of clinical dermatology*. 2000;1(4):225-234.

46. Longhi A, Ferrari S, Bacci G, Specchia S. Long-term follow-up of patients with doxorubicin-induced cardiac toxicity after chemotherapy for osteosarcoma. *Anticancer Drugs*. 2007;18(6):737-744.

47. Goto S, Ihara Y, Urata Y, et al. Doxorubicin-induced DNA intercalation and scavenging by nuclear glutathione S-transferase pi. *FASEB J*. 2001;15(14):2702-2714.

48. Thorn CF, Oshiro C, Marsh S, et al. Doxorubicin pathways: Pharmacodynamics and adverse effects. *Pharmacogenetics and Genomics*. 2011;21(7):440-446.

49. ROWINSKY E, DONEHOWER R. Drug-therapy - paclitaxel (taxol). *N Engl J Med*. 1995;332(15):1004-1014.

50. SPENCER C, FAULDS D. Paclitaxel - a review of its pharmacodynamic and pharmacokinetic properties and therapeutic potential in the treatment of cancer. *Drugs*. 1994;48(5):794-847.

51. Redis RS, Berindan-Neagoe I, Pop VI, Calin GA. Non-coding RNAs as theranostics in human cancers. *J Cell Biochem*. 2012;113(5):1451-1459.

52. Bartel DP. MicroRNAs: Genomics, biogenesis, mechanism, and function. *Cell*. 2004;116(2):281-297.

53. Calin GA, Dumitru CD, Shimizu M, et al. Frequent deletions and down-regulation of micro-RNA genes miR15 and miR16 at 13q14 in chronic lymphocytic leukemia. *Proc Natl Acad Sci U S A*. 2002;99(24):15524-15529.

54. Hatley ME, Patrick DM, Garcia MR, et al. Modulation of K-ras-dependent lung tumorigenesis by MicroRNA-21. *Cancer Cell*. 2010;18(3):282-293.

55. Zhao J, Lin J, Yang H, et al. MicroRNA-221/222 negatively regulates estrogen receptor alpha and is associated with tamoxifen resistance in breast cancer. *J Biol Chem*. 2008;283(45):31079-31086.

56. Fujita Y, Kojima K, Hamada N, et al. Effects of miR-34a on cell growth and chemoresistance in prostate cancer PC3 cells. *Biochem Biophys Res Commun*. 2008;377(1):114-119.

57. Chen Y, Zhu X, Zhang X, Liu B, Huang L. Nanoparticles modified with tumor-targeting scFv deliver siRNA and miRNA for cancer therapy. *Molecular Therapy*. 2010;18(9):1650-1656.

58. Kim J, Yeom J, Ko J, et al. Effective delivery of anti-miRNA DNA oligonucleotides by functionalized gold nanoparticles. *J Biotechnol*. 2011;155(3):287-292.

59. Oh Y, Park TG. siRNA delivery systems for cancer treatment. *Adv Drug Deliv Rev*. 2009;61(10):850-862.

60. Peer D, Park EJ, Morishita Y, Carman CV, Shimaoka M. Systemic leukocyte-directed siRNA delivery revealing cyclin D1 as an anti-inflammatory target. *Science*. 2008;319(5863):627-630.

61. Schiffelers RM, Storm G. ICS-283: A system for targeted intravenous delivery of siRNA. *Expert Opinion on Drug Delivery*. 2006;3(3):445-454.

62. Barenholz Y(. Doxil (R) - the first FDA-approved nano-drug: Lessons learned. *J Controlled Release*. 2012;160(2):117-134.

63. O'Brien M, Wigler N, Inbar M, et al. Reduced cardiotoxicity and comparable efficacy in a phase III trial of pegylated liposomal doxorubicin HCl (CAELYX (TM)/doxil (R)) versus conventional doxorubicin for first-line treatment of metastatic breast cancer. *Ann Oncol*. 2004;15(3):440-449.

64. Forssen EA, Ross ME. Daunoxome treatment of solid tumors: Preclinical and clinical investigations. *J Liposome Res*. 1994;4(1):481-512.

65. Green MR, Manikhas GM, Orlov S, et al. Abraxane((R)), a novel cremophor((R))-free, albumin-bound particle form of paclitaxel for the treatment of advanced non-small-cell lung cancer. *Ann Oncol*. 2006;17(8):1263-1268.

66. Kim T, Kim D, Chung J, et al. Phase I and pharmacokinetic study of genexol-PM, a cremophor-free, polymeric micelle-formulated paclitaxel, in patients with advanced malignancies. *Clin Cancer Res*. 2004;10(11):3708-3716.

67. Maeda H, Greish K, Fang J. The EPR effect and polymeric drugs: A paradigm shift for cancer chemotherapy in the 21st century. *Adv Polym Sci*. 2006;193:103-121.

68. Kobayashi H, Watanabe R, Choyke PL. Improving conventional enhanced permeability and retention (EPR) effects; what is the appropriate target? *Theranostics*. 2014;4(1):81-89.

69. Maruyama K. Intracellular targeting delivery of liposomal drugs to solid tumors based on EPR effects. *Adv Drug Deliv Rev*. 2011;63(3):161-169.

70. Acharya S, Sahoo SK. PLGA nanoparticles containing various anticancer agents and tumour delivery by EPR effect. *Adv Drug Deliv Rev*. 2011;63(3):170-183.

71. Maeda H, Wu J, Sawa T, Matsumura Y, Hori K. Tumor vascular permeability and the EPR effect in macromolecular therapeutics: A review. *J Controlled Release*. 2000;65(1-2):271-284.

72. Heldin C, Rubin K, Pietras K, Ostman A. High interstitial fluid pressure - an obstacle in cancer therapy. *Nat Rev Cancer*. 2004;4(10):806-813.

73. Maeda H. Vascular permeability in cancer and infection as related to macromolecular drug delivery, with emphasis on the EPR effect for tumor-selective drug targeting. *Proceedings of the Japan Academy Series B-Physical and Biological Sciences*. 2012;88(3):53-71.

74. Moghimi S, Hunter A, Murray J. Long-circulating and target-specific nanoparticles: Theory to practice. *Pharmacol Rev*. 2001;53(2):283-318.

75. Peer D, Karp JM, Hong S, FaroKHzad OC, Margalit R, Langer R. Nanocarriers as an emerging platform for cancer therapy. *Nat Nanotechnol*. 2007;2(12):751-760.

76. Baselga J, Norton L, Albanell J, Kim Y, Mendelsohn J. Recombinant humanized anti-HER2 antibody (herceptin (TM)) enhances the antitumor activity of paclitaxel and doxorubicin against HER2/neu overexpressing human breast cancer xenografts. *Cancer Res*. 1998;58(13):2825-2831.

77. Zhang X, Eden HS, Chen X. Peptides in cancer nanomedicine: Drug carriers, targeting ligands and protease substrates. *J Controlled Release*. 2012;159(1):2-13.

78. Pasqualini R, Ruoslahti E. Organ targeting in vivo using phage display peptide libraries. *Nature*. 1996;380(6572):364-366.

79. Davis ME. The first targeted delivery of siRNA in humans via a self-assembling, cyclodextrin polymer-based nanoparticle: From concept to clinic. *Molecular Pharmaceutics*. 2009;6(3):659-668.

80. Http://Meetinglibrary.asco.org/content/32235-65.

81. Yu MK, Park J, Jon S. Targeting strategies for multifunctional nanoparticles in cancer imaging and therapy. *Theranostics*. 2012;2(1):3-44.

82. Maloney D, GrilloLopez A, White C, et al. IDEC-C2B8 (rituximab) anti-CD20 monoclonal antibody therapy in patients with relapsed low-grade non-hodgkin's lymphoma. *Blood*. 1997;90(6):2188-2195.

83. Hurwitz H, Fehrenbacher L, Novotny W, et al. Bevacizumab plus irinotecan, fluorouracil, and leucovorin for metastatic colorectal cancer. *N Engl J Med*. 2004;350(23):2335-2342.

84. Cunningham D, Humblet Y, Siena S, et al. Cetuximab monotherapy and cetuximab plus irinotecan in irinotecan-refractory metastatic colorectal cancer. *N Engl J Med*. 2004;351(4):337-345.

85. Nygren P. Alternative binding proteins: Affibody binding proteins developed from a small three-helix bundle scaffold. *Febs J*. 2008;275(11):2668-2676.

86. Sudimack J, Lee R. Targeted drug delivery via the folate receptor. *Adv Drug Deliv Rev*. 2000;41(2):147-162.

87. Low PS, Kularatne SA. Folate-targeted therapeutic and imaging agents for cancer. *Curr Opin Chem Biol*. 2009;13(3):256-262.

88. Watanabe K, Kaneko M, Maitani Y. Functional coating of liposomes using a folate-polymer conjugate to target folate receptors. *International Journal of Nanomedicine*. 2012;7:3679-3688.

89. Qian Z, Li H, Sun H, Ho K. Targeted drug delivery via the transferrin receptor-mediated endocytosis pathway. *Pharmacol Rev*. 2002;54(4):561-587.

90. Anabousi S, Bakowsky U, Schneider M, Huwer H, Lehr C, Ehrhardt C. In vitro assessment of transferrin-conjugated liposomes as drug delivery systems for inhalation therapy of lung cancer. *European Journal of Pharmaceutical Sciences*. 2006;29(5):367-374.

91. Anabousi S, Bakowsky U, Schneider M, Huwer H, Lehr C, Ehrhardt C. In vitro assessment of transferrin-conjugated liposomes as drug delivery systems for inhalation therapy of lung cancer. *European Journal of Pharmaceutical Sciences*. 2006;29(5):367-374.

92. Reubi J. Peptide receptors as molecular targets for cancer diagnosis and therapy. *Endocr Rev*. 2003;24(4):389-427.

93. Arias JL. Drug targeting strategies in cancer treatment: An overview. *Mini-Reviews in Medicinal Chemistry*. 2011;11(1):1-17.

94. Haubner R, Wester H, Reuning U, et al. Radiolabeled alpha(v)beta(3) integrin antagonists: A new class of tracers for tumor targeting. *J Nucl Med*. 1999;40(6):1061-1071.

95. Zhan C, Gu B, Xie C, Li J, Liu Y, Lu W. Cyclic RGD conjugated poly(ethylene glycol)-co-poly(lactic acid) micelle enhances paclitaxel anti-glioblastoma effect. *J Controlled Release*. 2010;143(1):136-142.

96. Katsogiannou M, Peng L, Catapano CV, Rocchi P. Active-targeted nanotherapy strategies for prostate cancer. *Curr Cancer Drug Targets*. 2011;11(8):954-965.

97. Http://Clinicaltrials.gov/show/NCT00031187.

98. Http://Clinicaltrials.gov/ct2/show?term=ASG-5ME&rank=1.

99. Polascik T, Oesterling J, Partin A. Prostate specific antigen: A decade of discovery - what we have learned and where we are going. *J Urol*. 1999;162(2):293-306.

100. Chang S, Reuter V, Heston W, Bander N, Grauer L, Gaudin P. Five different anti-prostate-specific membrane antigen (PSMA) antibodies confirm PSMA expression in tumor-associated neovasculature. *Cancer Res*. 1999;59(13):3192-3198.

101. Liu H, Rajasekaran AK, Moy P, et al. Constitutive and antibody-induced internalization of prostate-specific membrane antigen. *Cancer Res*. 1998;58(18):4055-4060.

102. Xu W, Siddiqui IA, Nihal M, et al. Aptamer-conjugated and doxorubicin-loaded unimolecular micelles for targeted therapy of prostate cancer. *Biomaterials*. 2013;34(21):5244-5253.

103. Hubert RS, Vivanco I, Chen E, et al. STEAP: A prostate-specific cell-surface antigen highly expressed in human prostate tumors. *Proc Natl Acad Sci U S A*. 1999;96(25):14523-14528.

104. Alves PMS, Faure O, Graff-Dubois S, et al. STEAP, a prostate tumor antigen, is a target of human CD8(+) T cells. *Cancer Immunology Immunotherapy*. 2006;55(12):1515-1523.

105. Http://Clinicaltrials.gov/ct2/show/NCT01283373?term=DSTP3086S&rank=1.

106. Patel O, Shulkes A, Baldwin GS. Gastrin-releasing peptide and cancer. *Biochim Biophys Acta-Rev Cancer*. 2006;1766(1):23-41.

107. Cornelio DB, Roesler R, Schwartsmann G. Gastrin-releasing peptide receptor as a molecular target in experimental anticancer therapy. *Annals of Oncology*. 2007;18(9):1457-1466.

108. Beer M, Montani M, Gerhardt J, et al. Profiling gastrin-releasing peptide receptor in prostate tissues: Clinical implications and molecular correlates. *Prostate*. 2012;72(3):318-325.

109. Steinmetz NF, Ablack AL, Hickey JL, et al. Intravital imaging of human prostate cancer using viral nanoparticles targeted to gastrin-releasing peptide receptors. *Small*. 2011;7(12):1664-1672.

110. Hosta-Rigau L, Olmedo I, Arbiol J, Cruz LJ, Kogan MJ, Albericio F. Multifunctionalized gold nanoparticles with peptides targeted to gastrin-releasing peptide receptor of a tumor cell line. *Bioconjug Chem*. 2010;21(6):1070-1078.

111. Janib SM, Moses AS, MacKay JA. Imaging and drug delivery using theranostic nanoparticles. *Adv Drug Deliv Rev*. 2010;62(11):1052-1063.

112. Debbage P, Jaschke W. Molecular imaging with nanoparticles: Giant roles for dwarf actors. *Histochem Cell Biol*. 2008;130(5):845-875.

113. Choi KY, Jeon EJ, Yoon HY, et al. Theranostic nanoparticles based on PEGylated hyaluronic acid for the diagnosis, therapy and monitoring of colon cancer. *Biomaterials*. 2012;33(26):6186-6193.

114. Medintz IL, Uyeda HT, Goldman ER, Mattoussi H. Quantum dot bioconjugates for imaging, labelling and sensing. *Nature Materials*. 2005;4(6):435-446.

115. Tan WB, Jiang S, Zhang Y. Quantum-dot based nanoparticles for targeted silencing of HER2/neu gene via RNA interference. *Biomaterials*. 2007;28(8):1565-1571.

116. Derfus A, Chan W, Bhatia S. Probing the cytotoxicity of semiconductor quantum dots. *Nano Lett*. 2004;4(1):11-18.

117. Shilo M, Reuveni T, Motiei M, Popovtzer R. Nanoparticles as computed tomography contrast agents: Current status and future perspectives. *Nanomedicine*. 2012;7(2):257-269.

118. Liu Y, Ai K, Lu L. Nanoparticulate X-ray computed tomography contrast agents: From design validation to in vivo applications. *Acc Chem Res*. 2012;45(10):1817-1827.

119. Zhu J, Zheng L, Wen S, et al. Targeted cancer theranostics using alpha-tocopheryl succinate-conjugated multifunctional dendrimer-entrapped gold nanoparticles. *Biomaterials*. 2014;35(26):7635-7646.

120. Rabin O, Perez J, Grimm J, Wojtkiewicz G, Weissleder R. An X-ray computed tomography imaging agent based on long-circulating bismuth sulphide nanoparticles. *Nat Mater*. 2006;5(2):118-122.

121. Zanzonico P. Principles of nuclear medicine imaging: Planar, SPECT, PET, multi-modality, and autoradiography systems. *Radiat Res*. 2012;177(4):349-364.

122. Pysz MA, Gambhir SS, Willmann JK. Molecular imaging: Current status and emerging strategies. *Clin Radiol*. 2010;65(7):500-516.

123. Jennings LE, Long NJ. 'Two is better than one'-probes for dual-modality molecular imaging. *Chem Commun*. 2009(24):3511-3524.

124. Kao H, Lin Y, Chen C, et al. Evaluation of EGFR-targeted radioimmuno-gold-nanoparticles as a theranostic agent in a tumor animal model. *Bioorg Med Chem Lett*. 2013;23(11):3180-3185.

125. Liu Y, Welch MJ. Nanoparticles labeled with positron emitting nuclides: Advantages, methods, and applications. *Bioconjug Chem*. 2012;23(4):671-682.

126. Gambhir SS. Molecular imaging of cancer with positron emission tomography. *Nature Reviews Cancer*. 2002;2(9):683-693.

127. Juweid M, Cheson B. Current concepts - positron-emission tomography and assessment of cancer therapy. *N Engl J Med*. 2006;354(5):496-507.

128. Chen F, Hong H, Zhang Y, et al. In vivo tumor targeting and image-guided drug delivery with antibody-conjugated, radio labeled mesoporous silica nanoparticles. *ACS Nano*. 2013;7(10):9027-9039.

129. Toth E, Helm L, Merbach A. Relaxivity of MRI contrast agents. *Contrast Agents i*. 2002;221:61-101.

130. Tu C, Osborne EA, Louie AY. Activatable T (1) and T (2) magnetic resonance imaging contrast agents. *Ann Biomed Eng*. 2011;39(4):1335-1348.

131. Botta M. Second coordination sphere water molecules and relaxivity of gadolinium(III) complexes: Implications for MRI contrast agents. *Eur J Inorg Chem*. 2000(3):399-407.

132. Caravan P. Strategies for increasing the sensitivity of gadolinium based MRI contrast agents. *Chem Soc Rev*. 2006;35(6):512-523.

133. Langereis S, de Lussanet QG, van Genderen MHP, Backes WH, Meijer EW. Multivalent contrast agents based on gadolinium-diethylenetriaminepentaacetic acid-terminated poly(propylene imine) dendrimers for magnetic resonance imaging. *Macromolecules*. 2004;37(9):3084-3091.

134. CARR D, BROWN J, BYDDER G, et al. Gadolinium-dtpa as a contrast agent in mri - initial clinical-experience in 20 patients. *Am J Roentgenol*. 1984;143(2):215-224.

135. Lauffer R, Parmelee D, Dunham S, et al. MS-325: Albumin-targeted contrast agent for MR angiography. *Radiology*. 1998;207(2):529-538.

136. Yang JJ, Yang J, Wei L, et al. Rational design of protein-based MRI contrast agents. *J Am Chem Soc*. 2008;130(29):9260-9267.

137. Xue S, Qiao J, Pu F, Cameron M, Yang JJ. Design of a novel class of protein-based magnetic resonance imaging contrast agents for the molecular imaging of cancer biomarkers. *Wiley Interdiscip Rev -Nanomed Nanobiotechnol*. 2013;5(2):163-179.

138. Qiao J, Li S, Wei L, et al. HER2 targeted molecular MR imaging using a de novo designed protein contrast agent. *Plos One*. 2011;6(3):e18103.

139. Bruckman MA, Yu X, Steinmetz NF. Engineering gd-loaded nanoparticles to enhance MRI sensitivity via T-1 shortening. *Nanotechnology*. 2013;24(46):462001.

140. Al-Jamal WT, Kostarelos K. Liposome-nanoparticle hybrids for multimodal diagnostic and therapeutic applications. *Nanomedicine (London, England)*. 2007;2(1):85-98.

141. Kielar F, Tei L, Terreno E, Botta M. Large relaxivity enhancement of paramagnetic lipid nanoparticles by restricting the local motions of the gd-III chelates. *J Am Chem Soc*. 2010;132(23):7836-+.

142. Kobayashi H, Brechbiel M. Nano-sized MRI contrast agents with dendrimer cores. *Adv Drug Deliv Rev*. 2005;57(15):2271-2286.

143. Huang C, Nwe K, Al Zaki A, Brechbiel MW, Tsourkas A. Biodegradable polydisulfide dendrimer nanoclusters as MRI contrast agents. *Acs Nano*. 2012;6(11):9416-9424.

144. Lam T, Pouliot P, Avti PK, Lesage F, Kakkar AK. Superparamagnetic iron oxide based nanoprobes for imaging and theranostics. *Adv Colloid Interface Sci*. 2013;199:95-113.

145. Mikhaylova M, Kim D, Bobrysheva N, et al. Superparamagnetism of magnetite nanoparticles: Dependence on surface modification. *Langmuir*. 2004;20(6):2472-2477.

146. Lee C, Jeong H, Kim S, et al. SPION-loaded chitosan-linoleic acid nanoparticles to target hepatocytes. *Int J Pharm*. 2009;371(1-2):163-169.

147. Uzun K, Cevik E, Senel M, et al. Covalent immobilization of invertase on PAMAM-dendrimer modified superparamagnetic iron oxide nanoparticles. *Journal of Nanoparticle Research*. 2010;12(8):3057-3067.

148. Lee H, Yu MK, Park S, et al. Thermally cross-linked superparamagnetic iron oxide nanoparticles: Synthesis and application as a dual imaging probe for cancer in vivo. *J Am Chem Soc*. 2007;129(42):12739-12745.

149. Moura CC, Segundo MA, das Neves J, Reis S, Sarmento B. Co-association of methotrexate and SPIONs into anti-CD64 antibody-conjugated PLGA nanoparticles for theranostic application. *International Journal of Nanomedicine*. 2014;9:4911-4922.

150. Smejkalova D, Nesporova K, Huerta-Angeles G. Selective in vitro anticancer effect of superparamagnetic iron oxide nanoparticles loaded in hyaluronan polymeric micelles. *Biomacromolecules*. 2014;15(11):4012-4020.

151. Lammers T, Aime S, Hennink WE, Storm G, Kiessling F. Theranostic nanomedicine. *Acc Chem Res*. 2011;44(10):1029-1038.

152. Balasubramaniam S, Pothayee N, Lin Y, et al. Poly(N-isopropylacrylamide)-coated superparamagnetic iron oxide nanoparticles: Relaxometric and fluorescence behavior correlate to temperature-dependent aggregation. *Chem Mat*. 2011;23(14):3348-3356.

153. Grogna M, Cloots R, Luxen A, et al. Polymer micelles decorated by gadolinium complexes as MRI blood contrast agents: Design, synthesis and properties. *Polymer Chemistry*. 2010;1(9):1485-1490.

154. Jeong SY, Kim HJ, Kwak B, et al. Biocompatible polyhydroxyethylaspartamide-based micelles with gadolinium for MRI contrast agents. *Nanoscale Research Letters*. 2010;5(12):1970-1976.

155. Shiraishi K, Kawano K, Maitani Y, Yokoyama M. Polyion complex micelle MRI contrast agents from poly(ethylene glycol)-b-poly(L-lysine) block copolymers having gd-DOTA; preparations and their control of T-1-relaxivities and blood circulation characteristics. *J Controlled Release*. 2010;148(2):160-167.

156. Kim KS, Park W, Hu J, Bae YH, Na K. A cancer-recognizable MRI contrast agents using pH-responsive polymeric micelle. *Biomaterials*. 2014;35(1):337-343.

157. Liu T, Li X, Qian Y, Hu X, Liu S. Multifunctional pH-disintegrable micellar nanoparticles of asymmetrically functionalized beta-cyclodextrin-based star copolymer

covalently conjugated with doxorubicin and DOTA-gd moieties. *Biomaterials*. 2012;33(8):2521-2531.

158. Rowe MD, Thamm DH, Kraft SL, Boyes SG. Polymer-modified gadolinium metal-organic framework nanoparticles used as multifunctional nanomedicines for the targeted imaging and treatment of cancer. *Biomacromolecules*. 2009;10(4):983-993.

159. Yongjun L, Junsheng L. **Theranostic polymeric micelles for the diagnosis and treatment of hepatocellular carcinoma**. *Journal of Biomedical Nanotechnology*. 2015;11(4):613-622.

160. URRY D, TRAPANE T, PRASAD K. Phase-structure transitions of the elastin polypentapeptide water-system within the framework of composition temperature studies. *Biopolymers*. 1985;24(12):2345-2356.

161. Urry DW. Physical chemistry of biological free energy transduction as demonstrated by elastic protein-based polymers. *J Phys Chem B*. 1997;101(51):11007-11028.

162. Yamaoka T, Tamura T, Seto Y, Tada T, Kunugi S, Tirrell DA. Mechanism for the phase transition of a genetically engineered elastin model peptide (VPGIG)(40) in aqueous solution. *Biomacromolecules*. 2003;4(6):1680-1685.

163. Girotti A, Reguera J, Arias FJ, Alonso M, Testera AM, Rodriguez-Cabello JC. Influence of the molecular weight on the inverse temperature transition of a model genetically engineered elastin-like pH-responsive polymer. *Macromolecules*. 2004;37(9):3396-3400.

164. Alonso M, Reboto V, Guiscardo L, Mate V, Rodriguez-Cabello JC. Novel photoresponsive p-phenylazobenzene derivative of an elastin-like polymer with enhanced control of azobenzene content and without pH sensitiveness. *Macromolecules*. 2001;34(23):8072-8077.

165. Cho Y, Zhang Y, Christensen T, Sagle LB, Chilkoti A, Cremer PS. Effects of hofmeister anions on the phase transition temperature of elastin-like polypeptides. *J Phys Chem B*. 2008;112(44):13765-13771.

166. Xu W, Siddiqui IA, Nihal M, et al. Aptamer-conjugated and doxorubicin-loaded unimolecular micelles for targeted therapy of prostate cancer. *Biomaterials*. 2013;34(21):5244-5253.

167. MacKay JA, Callahan DJ, FitzGerald KN, Chilkoti A. Quantitative model of the phase behavior of recombinant pH-responsive elastin-like polypeptides. *Biomacromolecules*. 2010;11(11):2873-2879.

168. Hrabchak C, Rouleau J, Moss I, et al. Assessment of biocompatibility and initial evaluation of genipin cross-linked elastin-like polypeptides in the treatment of an osteochondral knee defect in rabbits. *Acta Biomaterialia*. 2010;6(6):2108-2115.

169. Liu W, Dreher MR, Chow DC, Zalutsky MR, Chilkoti A. Tracking the in vivo fate of recombinant polypeptides by isotopic labeling. *J Controlled Release*. 2006;114(2):184-192.

170. MacEwan SR, Chilkoti A. Applications of elastin-like polypeptides in drug delivery. *Journal of controlled release : official journal of the Controlled Release Society*. 2014;190:314-330.

171. MacKay JA, Chen M, McDaniel JR, Liu W, Simnick AJ, Chilkoti A. Self-assembling chimeric polypeptide-doxorubicin conjugate nanoparticles that abolish tumours after a single injection. *Nature Materials*. 2009;8(12):993-999.

172. McDaniel JR, Bhattacharyya J, Vargo KB, Hassouneh W, Hammer DA, Chilkoti A. Self-assembly of thermally responsive nanoparticles of a genetically encoded peptide polymer by drug conjugation. *Angewandte Chemie-International Edition*. 2013;52(6):1683-1687.

173. Rincon AC, Molina-Martinez IT, de las Heras B, et al. Biocompatibility of elastin-like polymer poly(VPAVG) microparticles: In vitro and in vivo studies. *Journal of Biomedical Materials Research Part a*. 2006;78A(2):343-351.

174. Martinez AW, Caves JM, Ravi S, Li W, Chaikof EL. Effects of crosslinking on the mechanical properties, drug release and cytocompatibility of protein polymers. *Acta Biomater*. 2014;10(1):26-33.

175. Nagapudi K, Brinkman WT, Leisen JE, et al. Photomediated solid-state cross-linking of an elastin-mimetic recombinant protein polymer. *Macromolecules*. 2002;35(5):1730-1737.

176. McHale MK, Setton LA, Chilkoti A. Synthesis and in vitro evaluation of enzymatically cross-linked elastin-like polypeptide gels for cartilaginous tissue repair. *Tissue Eng*. 2005;11(11-12):1768-1779.

177. Chung C, Lampe KJ, Heilshorn SC. Tetrakis(hydroxymethyl) phosphonium chloride as a covalent cross-linking agent for cell encapsulation within protein-based hydrogels. *Biomacromolecules*. 2012;13(12):3912-3916.

178. Lim DW, Nettles DL, Setton LA, Chilkoti A. In situ cross-linkinig of elastin-like polypeptide block copolymers for tissue repair. *Biomacromolecules*. 2008;9(1):222-230.

179. Benitez PL, Sweet JA, Fink H, et al. Sequence-specific crosslinking of electrospun, elastin-like protein preserves bioactivity and native-like mechanics. *Advanced Healthcare Materials*. 2013;2(1):114-118.

180. McDaniel JR, Callahan DJ, Chilkoti A. Drug delivery to solid tumors by elastin-like polypeptides. *Adv Drug Deliv Rev*. 2010;62(15):1456-1467.

181. Dreher MR, Liu W, Michelich CR, Dewhirst MW, Chilkoti A. Thermal cycling enhances the accumulation of a temperature-sensitive biopolymer in solid tumors. *Cancer Res*. 2007;67(9):4418-4424.

182. Moktan S, Perkins E, Kratz F, Raucher D. Thermal targeting of an acid-sensitive doxorubicin conjugate of elastin-like polypeptide enhances the therapeutic efficacy compared with the parent compound in vivo. *Molecular Cancer Therapeutics*. 2012;11(7):1547-1556.

183. Shi P, Aluri S, Lin Y, et al. Elastin-based protein polymer nanoparticles carrying drug at both corona and core suppress tumor growth in vivo. *J Controlled Release*. 2013;171(3):330-338.

184. Moktan S, Ryppa C, Kratz F, Raucher D. A thermally responsive biopolymer conjugated to an acid-sensitive derivative of paclitaxel stabilizes microtubules, arrests cell cycle, and induces apoptosis. *Invest New Drugs*. 2012;30(1):236-248.

185. Simnick AJ, Valencia CA, Liu R, Chilkoti A. Morphing low-affinity ligands into high-avidity nanoparticles by thermally triggered self-assembly of a genetically encoded polymer. *ACS Nano*. 2010;4(4):2217-2227.

186. Simnick AJ, Amiram M, Liu W, et al. In vivo tumor targeting by a NGR-decorated micelle of a recombinant diblock copolypeptide. *J Controlled Release*. 2011;155(2):144-151.

187. Hassouneh W, Fischer K, MacEwan SR, et al. Unexpected multivalent display of proteins by temperature triggered self-assembly of elastin-like polypeptide block copolymers. *Biomacromolecules*. 2012;13(5):1598-1605.

188. MacKay JA, Callahan DJ, FitzGerald KN, Chilkoti A. Quantitative model of the phase behavior of recombinant pH-responsive elastin-like polypeptides. *Biomacromolecules*. 2010;11(11):2873-2879.

189. Callahan DJ, Liu W, Li X, et al. Triple stimulus-responsive polypeptide nanoparticles that enhance intratumoral spatial distribution. *Nano Letters*. 2012;12(4):2165-2170.

190. Hassouneh W, Nunalee ML, Shelton MC, Chilkoti A. Calcium binding peptide motifs from calmodulin confer divalent ion selectivity to elastin-like polypeptides. *Biomacromolecules*. 2013;14(7):2347-2353.

191. Frank S, Kammerer R, Mechling D, et al. Stabilization of short collagen-like triple helices by protein engineering. *J Mol Biol*. 2001;308(5):1081-1089.

192. Du C, Wang M, Liu J, Pan M, Cai Y, Yao J. Improvement of thermostability of recombinant collagen-like protein by incorporating a foldon sequence. *Appl Microbiol Biotechnol*. 2008;79(2):195-202.

193. Ghoorchian A, Cole JT, Holland NB. Thermoreversible micelle formation using a three-armed star elastin-like polypeptide. *Macromolecules*. 2010;43(9):4340-4345.

194. Ghoorchian A, Vandemark K, Freeman K, Kambow S, Holland NB, Streletzky KA. Size and shape characterization of thermoreversible micelles of three-armed star elastin-like polypeptides. *J Phys Chem B*. 2013;117(29):8865-8874.

195. CHEN C, OKAYAMA H. High-efficiency transformation of mammalian-cells by plasmid dna. *Mol Cell Biol*. 1987;7(8):2745-2752.

196. Bar M, Bar-Ziv R, Scherf T, Fass D. Efficient production of a folded and functional, highly disulfide-bonded beta-helix antifreeze protein in bacteria. *Protein Expr Purif*. 2006;48(2):243-252.

197. Chilkoti A, Dreher MR, Meyer DE. Design of thermally responsive, recombinant polypeptide carriers for targeted drug delivery. *Adv Drug Deliv Rev*. 2002;54(8):1093-1111.

198. McPherson DT, Xu J, Urry DW. Product purification by reversible phase transition following escherichia coli expression of genes encoding up to 251 repeats of the elastomeric pentapeptide GVGVP. *Protein Expr Purif*. 1996;7(1):51-57.

199. Meyer D, Chilkoti A. Quantification of the effects of chain length and concentration on the thermal behavior of elastin-like polypeptides. *Biomacromolecules*. 2004;5(3):846-851.

200. Urry DW, Luan CH, Parker TM, et al. Temperature of polypeptide inverse temperature transition depends on mean residue hydrophobicity. *J Am Chem Soc*. 1991;113(11):4346-4348.

201. Meyer DE, Chilkoti A. Purification of recombinant proteins by fusion with thermally-responsive polypeptides. *Nat Biotechnol*. 1999;17(11):1112-1115.

202. Meyer DE, Trabbic-Carlson K, Chilkoti A. Protein purification by fusion with an environmentally responsive elastin-like polypeptide: Effect of polypeptide length on the purification of thioredoxin. *Biotechnol Prog*. 2001;17(4):720-728.

203. Yu S, Liu Y. Expression and one-step purification of a beta-galactosidase by fusion with elastin-like polypetides. *Process Biochem*. 2012;47(7):1108-1114.

204. Fong BA, Wu W, Wood DW. Optimization of ELP-intein mediated protein purification by salt substitution. *Protein Expr Purif*. 2009;66(2):198-202.

205. Chow D, Dreher M, Trabbic-Carlson K, Chilkoti A. Ultra-high expression of a thermally responsive recombinant fusion protein in E-coli. *Biotechnol Prog*. 2006;22(3):638-646.

206. Wagner JG. Interpretation of percent dissolved-time plots derived from in vitro testing of conventional tablets and capsules. *J Pharm Sci*. 1969;58(10):1253-&.

207. Yang W, Jones LM, Isley L, et al. Rational design of a calcium-binding protein. *J Am Chem Soc*. 2003;125(20):6165-6171.

208. Grobner T. Gadolinium - a specific trigger for the development of nephrogenic fibrosing dermopathy and nephrogenic systemic fibrosis? (vol 21, pg 1104, 2006). *Nephrol Dial Transplant*. 2006;21(6):1745-1745.

209. Clogston JD, Patri AK. Detecting and measuring free gadolinium in nanoparticles for MRI imaging. *Characterization of Nanoparticles Intended for Drug Delivery*. 2011;697:101-108.

210. Nagaraja TN, Croxen RL, Panda S, et al. Application of arsenazo III in the preparation and characterization of an albumin-linked, gadolinium-based macromolecular magnetic resonance contrast agent. *J Neurosci Methods*. 2006;157(2):238-245.

211. Woods M, Pasha A, Zhao P, et al. Investigations into whole water, prototropic and amide proton exchange in lanthanide(III) DOTA-tetraamide chelates. *Dalton Transactions*. 2011;40(25):6759-6764.

212. Barge A, Cravotto G, Gianolio E, Fedeli F. How to determine free gd and free ligand in solution of gd chelates. A technical note. *Contrast Media Mol Imaging*. 2006;1(5):184-188.

213. ALLEN T, CHONN A. Large unilamellar liposomes with low uptake into the reticuloendothelial system. *FEBS Lett*. 1987;223(1):42-46.

214. Mieszawska AJ, Mulder WJM, Fayad ZA, Cormode DP. Multifunctional gold nanoparticles for diagnosis and therapy of disease. *Mol Pharm*. 2013;10(3):831-847.

215. Li S, Goins B, Zhang L, Bao A. Novel multifunctional theranostic liposome drug delivery system: Construction, characterization, and multimodality MR, near-infrared fluorescent, and nuclear imaging. *Bioconjug Chem*. 2012;23(6):1322-1332.

216. Chen Z, Yu D, Liu C, et al. Gadolinium-conjugated PLA-PEG nanoparticles as liver targeted molecular MRI contrast agent. *J Drug Target*. 2011;19(8):657-665.

217. Talelli M, Rijcken CJF, van Nostrum CF, Storm G, Hennink WE. Micelles based on HPMA copolymers. *Adv Drug Deliv Rev*. 2010;62(2):231-239.

218. Caldorera-Moore ME, Liechty WB, Peppas NA. Responsive theranostic systems: Integration of diagnostic imaging agents and responsive controlled release drug delivery carriers. *Acc Chem Res*. 2011;44(10):1061-1070.

219. Caravan P, Farrar CT, Frullano L, Uppal R. Influence of molecular parameters and increasing magnetic field strength on relaxivity of gadolinium- and manganese-based T(1) contrast agents. *Contrast Media & Molecular Imaging*. 2009;4(2):89-100.

220. URRY D, HAYNES B, HARRIS R. Temperature-dependence of length of elastin and its polypentapeptide. *Biochem Biophys Res Commun*. 1986;141(2):749-755.

221. Alonso M, Reboto V, Guiscardo L, Mate V, Rodriguez-Cabello J. Novel photoresponsive p-phenylazobenzene derivative of an elastin-like polymer with enhanced control of azobenzene content and without pH sensitiveness. *Macromolecules*. 2001;34(23):8072-8077.

222. Park J, Won J. Thermal behaviors of elastin-like polypeptides (ELPs) according to their physical properties and environmental conditions. *Biotechnology and Bioprocess Engineering*. 2009;14(5):662-667.

223. McDaniel JR, Callahan DJ, Chilkoti A. Drug delivery to solid tumors by elastin-like polypeptides. *Adv Drug Deliv Rev*. 2010;62(15):1456-1467.

224. Betre H, Setton L, Meyer D, Chilkoti A. Characterization of a genetically engineered elastin-like polypeptide for cartilaginous tissue repair. *Biomacromolecules*. 2002;3(5):910-916.

225. Rao G, Balamurugan S, Meyer D, Chilkoti A, Lopez G. Hybrid bioinorganic smart membranes that incorporate protein-based molecular switches. *Langmuir*. 2002;18(5):1819-1824.

226. Asai D, Xu D, Liu W, et al. Protein polymer hydrogels by in situ, rapid and reversible self-gelation. *Biomaterials*. 2012;33(21):5451-5458.

227. Meyer D, Chilkoti A. Genetically encoded synthesis of protein-based polymers with precisely specified molecular weight and sequence by recursive directional ligation: Examples from the elastin-like polypeptide system. *Biomacromolecules*. 2002;3(2):357-367.

228. Hanaoka K, Lubag AJM, Castillo-Muzquiz A, Kodadek T, Sherry AD. The detection limit of a Gd3+-based T-1 agent is substantially reduced when targeted to a protein microdomain. *Magn Reson Imaging*. 2008;26(5):608-617.

229. Ghoorchian A, Holland NB. Molecular architecture influences the thermally induced aggregation behavior of elastin-like polypeptides. *Biomacromolecules*. 2011;12(11):4022-4029.

230. Yamaoka T, Tamura T, Seto Y, Tada T, Kunugi S, Tirrell D. Mechanism for the phase transition of a genetically engineered elastin model peptide (VPGIG)(40) in aqueous solution. *Biomacromolecules*. 2003;4(6):1680-1685.

231. GILL S, VONHIPPEL P. Calculation of protein extinction coefficients from amino-acid sequence data. *Anal Biochem*. 1989;182(2):319-326.

232. Barge A, Cravotto G, Gianolio E, Fedeli F. How to determine free gd and free ligand in solution of gd chelates. A technical note. *Contrast Media & Molecular Imaging*. 2006;1(5):184-188.

233. Clogston JD, Patri AK. Detecting and measuring free gadolinium in nanoparticles for MRI imaging. *Characterization of Nanoparticles Intended for Drug Delivery*. 2011;697:101-108.

234. Xu X, Smith AE, McCormick CL. Facile 'one-pot' preparation of reversible, disulfide-containing shell cross-linked micelles from a RAFT-synthesized, pH-responsive triblock copolymer in water at room temperature. *Aust J Chem*. 2009;62(11):1520-1527.

235. Li Y, Lokitz B, McCormick C. RAFT synthesis of a thermally responsive ABC triblock copolymer incorporating N-acryloxysuccinimide for facile in situ formation of shell cross-linked micelles in aqueous media. *Macromolecules*. 2006;39(1):81-89.

236. Osborne JL, Farmer R, Woodhouse KA. Self-assembled elastin-like polypeptide particles. *Acta Biomaterialia*. 2008;4(1):49-57.

237. Gianolio E, Giovenzana GB, Longo D, Longo I, Menegotto I, Aime S. Relaxometric and modelling studies of the binding of a lipophilic gd-AAZTA complex to fatted and defatted human serum albumin. *Chem -Eur J*. 2007;13(20):5785-5797.

238. Nicolle G, Helm L, Merbach A. S-8 paramagnetic centres in molecular assemblies: Possible effect of their proximity on the water proton relaxivity. *Magn Reson Chem*. 2003;41(10):794-799.

239. Luk BT, Fang RH, Zhang L. Lipid- and polymer-based nanostructures for cancer theranostics. *Theranostics*. 2012;2(12):1117-1126.

240. Kozlowska D, Foran P, MacMahon P, Shelly MJ, Eustace S, O'Kennedy R. Molecular and magnetic resonance imaging: The value of immunoliposomes. *Adv Drug Deliv Rev*. 2009;61(15):1402-1411.

241. Peer D, Karp JM, Hong S, FaroKHzad OC, Margalit R, Langer R. Nanocarriers as an emerging platform for cancer therapy. *Nature Nanotechnology*. 2007;2(12):751-760.

242. Frangioni JV. New technologies for human cancer imaging. *J Clin Oncol*. 2008;26(24):4012-4021.

243. Caravan P, Ellison J, McMurry T, Lauffer R. Gadolinium(III) chelates as MRI contrast agents: Structure, dynamics, and applications. *Chem Rev*. 1999;99(9):2293-2352.

244. Lee GY, Qian WP, Wang L, et al. Theranostic nanoparticles with controlled release of gemcitabine for targeted therapy and MRI of pancreatic cancer. *ACS Nano*. 2013;7(3):2078-2089.

245. Li NK, Quiroz FG, Hall CK, Chilkoti A, Yingling YG. Molecular description of the LCST behavior of an elastin-like polypeptide. *Biomacromolecules*. 2014;15(10):3522-3530.

246. Rembert KB, Paterova J, Heyda J, Hilty C, Jungwirth P, Cremer PS. Molecular mechanisms of ion-specific effects on proteins. *J Am Chem Soc*. 2012;134(24):10039-10046.

247. Reile H, Armatis PE, Schally AV. Characterization of high-affinity receptors for bombesin/gastrin releasing peptide on the human prostate-cancer cell-lines pc-3 and du-

145 - internalization of receptor-bound (125)i-(tyr(4)) bombesin by tumor-cells. *Prostate*. 1994;25(1):29-38.

248. Pinski J, Schally AV, Halmos G, Szepeshazi K, Groot K. Somatostatin analogs and bombesin/gastrin-releasing peptide antagonist rc-3095 inhibit the growth of human glioblastomas in-vitro and in-vivo. *Cancer Res*. 1994;54(22):5895-5901.

249. Roebroek AJM, Martens GJM, Duits AJ, et al. Differential expression of the gene encoding the novel pituitary polypeptide 7b2 in human-lung cancer-cells. *Cancer Res*. 1989;49(15):4154-4158.

250. Migneault I, Dartiguenave C, Bertrand MJ, Waldron KC. Glutaraldehyde: Behavior in aqueous solution, reaction with proteins, and application to enzyme crosslinking. *BioTechniques*. 2004;37(5):790-+.

251. Kuo PH, Kanal E, Abu-Alfa AK, Cowper SE. Gadolinium-based MR contrast agents and nephrogenic systemic fibrosis. *Radiology*. 2007;242(3):647-649.

APPENDIX

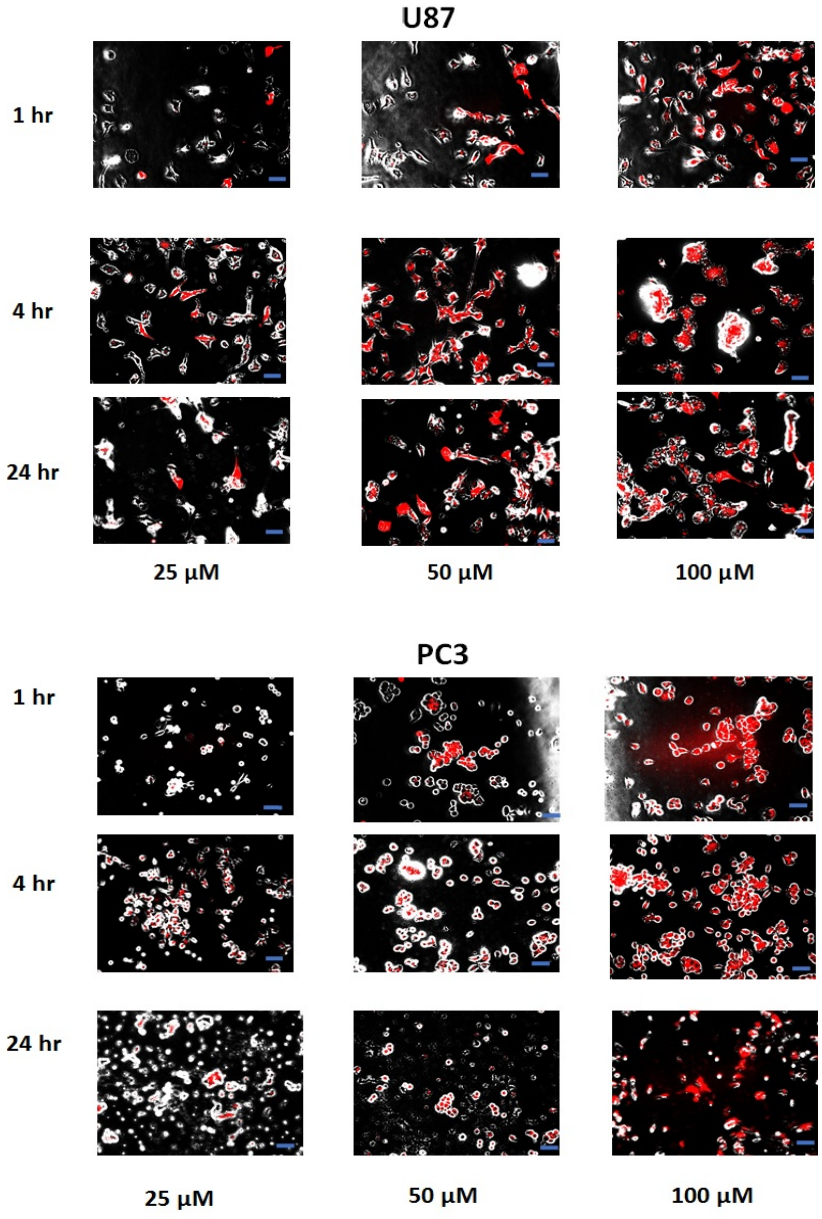

Figure A-1: Incubation of Doxorubicin loaded ELP-THO nanoparticles with cells. Nanoparticles were incubated with both PC3 and U87 cells at different concentrations and for different time periods. There is clearly an increase in interaction with the cells with increasing in incubation time as well as protein concentration.